# Studies on the Neutrality of Antihydrogen

by

Marcelo Baquero-Ruiz

A dissertation submitted in partial satisfaction of the
requirements for the degree of
Doctor of Philosophy

in

Physics

in the

Graduate Division

of the

University of California, Berkeley

Committee in charge:

Professor Joel Fajans, Chair
Professor Jonathan Wurtele
Professor Michael Lieberman

Fall 2013

The dissertation of Marcelo Baquero-Ruiz, titled Studies on the Neutrality of Antihydrogen, is approved:

Chair Date

Date

Date

University of California, Berkeley

**Studies on the Neutrality of Antihydrogen**

Copyright 2013
by
Marcelo Baquero-Ruiz

# Abstract

Studies on the Neutrality of Antihydrogen

by

Marcelo Baquero-Ruiz

Doctor of Philosophy in Physics

University of California, Berkeley

Professor Joel Fajans, Chair

The recent demonstration of trapping of antihydrogen atoms by the ALPHA collaboration at CERN opened great possibilities to study antimatter and perform precision measurements on it.

In this work, a retrospective analysis of the 2010 and 2011 experimental runs in ALPHA, together with comprehensive studies of the apparatus and detailed simulations of the manipulations of anti-atoms, are performed and used to measure the electric charge of antihydrogen. This result is an example of a precision measurement on antimatter that may ultimately lead to keys for solving some of the most important problems in physics today, such as the asymmetry between matter and antimatter, by comparison to measurements carried out on "normal" matter atoms.

A procedure similar to the one presented may lead to increased precision with a larger data sample, perhaps using the new ALPHA2 apparatus. Nevertheless, a method using "stochastic heating" is proposed that could increase the precision of the measurement by many orders of magnitude. The technique offers many other advantages that make it very attractive for future experimental implementations.

To my family

# Contents

# List of Figures

# List of Tables

# Acknowledgments

I want to thank all members of the ALPHA collaboration for their dedication and the incredible effort they have made to make antimatter research a reality. The work presented in this thesis would have not been possible without their hard work nor without the fruitful discussions that have taken place since the studies of charge of antihydrogen were first proposed.

Special thanks to my advisor, Prof. Joel Fajans, for his support, guidance and encouragement in the long process of working on an idea until reaching a final result.

Many thanks as well to Prof. Jonathan Wurtele and Prof. Michael Lieberman for their helpful advise and comments. They were very important for putting this dissertation in final form.

# Chapter 1

# Introduction

## 1.1 Overview

In the decade since antihydrogen, the simplest form of atomic antimatter composed by one antiproton ($\bar{\text{p}}$) and one positron ($\text{e}^+$) bound by the electric force, was first created in a laboratory [1, 2, 3], antimatter research has experienced major progress. The ALPHA (Antihydrogen Laser Physics Apparatus) collaboration [4], whose experimental apparatus is located at the Antiproton Decelerator facility at CERN (Switzerland), has contributed significantly to this effort by demonstrating the first ever trapping of cold antihydrogen atoms [5, 6], performing studies of their formation dynamics and confinement time [7] and succeeding at probing their internal structure for the first time using microwaves [8]. Also, by a careful analysis of the experimental data, loose bounds were established on the ratio of gravitational to inertial mass of antihydrogen [9].

These achievements, together with research performed by other groups [2, 10], have opened the way to new studies of the fundamental symmetries of our world and the possibility to address some of the most fundamental questions in physics today [11]. By performing precise measurements on trapped antihydrogen and comparing them to measurements carried out on "normal" hydrogen, for example, CPT invariance can be put to a test and evidence for the source of the asymmetry between matter and antimatter in the universe can be sought. One test that is often proposed for this is the comparison of spectra, and in particular of the narrow 1S-2S transition that has been measured to precisions of $4 \times 10^{-15}$ in hydrogen [12]. Also, there is interest in investigating the weak equivalence principle by measuring precisely the effect of gravity on antimatter [9, 11].

Spectral and gravitational measurements are not the only measurements that can be performed on anti-atoms. In this work, two methods are explored to measure the *electric charge of antihydrogen* using ALPHA1, the apparatus used by ALPHA during the 2010 and 2011 experimental runs.

"Normal" matter is experimentally known to be electrically neutral to great precision. Although no direct measurements seem to exist for H (atomic hydrogen), other diverse species such as He, $H_2$, and $SF_6$ are known to be neutral to about $10^{-21}$ [13]. It is therefore expected, based on CPT symmetry, that antihydrogen be charge neutral.

The techniques used to measure the charge on matter rely on macroscopic quantities of atoms or molecules; for example, by letting escape atoms or molecules from an electrically isolated container, or by attempting to excite sound waves in a gas with oscillating electric fields [13]. In contrast, only very small quantities of antihydrogen can be produced and trapped (about one anti-atom per attempt [7]) and therefore it is not possible to replicate the same experiments with antimatter.

The only previous direct bound established on the charge of antihydrogen was inferred from the observation that an energetic beam [14] of anti-atoms could not be deflected away from a detector by the magnetic force $Qe(\vec{v} \times \vec{B})$, where $e$ is the elementary charge and $Q$ is the "fractional charge" (see sec. 1.2). This measurement established that $|Q| < 0.02$. Better bounds can be found by comparing the measured charges of the antiproton and positron. The charge anomaly of the antiproton, $(|q_{\bar{p}}| - e)/e$, is known to be less than $7 \times 10^{-10}$ with a confidence level of 90% by measurements on $\bar{p}\mathrm{He}^+$ [10]. The charge anomaly of the positron, $(q_{e^+} - e)/e$, is known [15] to less than $4 \times 10^{-8}$ by measurements of the positron cyclotron frequency and the positronium Rydberg. Hence, it is possible to infer a bound on the fractional charge of antihydrogen of $|Q| \leq 4 \times 10^{-8}$ [16].

The methods described in this thesis give a "direct" precision measurement of the charge of antihydrogen, if any, leading to bounds equal or better than this existing one. They are "direct" in that the results do not depend on high precision measurements of other parameters, such as the mass of antihydrogen or its magnetic moment. Since the charge of the antiproton is known to better precision, this measurement constitutes a precision measurement of the charge of the positron under the very likely assumption that the total charge of antihydrogen is equivalent to the sum of the charges of its constituent particles.

This thesis is organized as follows: A brief overview of the experimental techniques and subsystems of interest of the ALPHA1 apparatus are described in chapter 2 in order to provide a background and introduce terminology. Chapter 3 gives a description of the computer simulations developed to study the dynamics of antihydrogen in the trap. Chapter 4 builds upon the previous chapters and establishes a bound on the charge of antihydrogen atoms using a technique based on the analysis of the axial location of annihilations of trapped antihydrogen released from the magnetic trap. Finally, chapter 5 describes a proposed method based on stochastic heating that can improve the bound by many orders of magnitude. This method may be implemented in future experimental runs in ALPHA, most likely in the new ALPHA2 apparatus currently being commissioned.

## 1.2 Units and conventions

Throughout this document, Système International (SI) units will be used.

In some chapters, it will be useful to measure energies in units of K (Kelvin); context will make it clear when a quantity measured in K does not refer to temperature. The conversion to the corresponding SI unit "J" (Joule) can straightforwardly be performed through multiplication by the Boltzmann constant, $k_B = 1.381 \times 10^{-23}$ J/K.

One important definition that will be extensively used is that of the "fractional charge" $Q$. It is equivalent to the total electric charge divided by $e = 1.602 \times 10^{-19}$ C, the "elementary charge". Note that this means that $Q$ is defined to be *dimensionless*. Also, as $e$ is defined as a *positive* number, $Q < 0$ refers to a negative total electric charge.

Due to the cylindrical symmetry of the trap (sec. 2.1), vector quantities will usually be expressed in "axial" and "radial" components. The former correspond to the direction parallel to the trap axis, which is also parallel to the background magnetic field used for charged particle confinement. The letter '$z$' will be used to denote axial quantities, and the positive $z$ direction will point towards the *positron* end of the apparatus (Fig. 2.2). In the case of positions, $z = 0$ corresponds to the axial midpoint of the center electrode in the "mixing region" of the trap (electrode number 18), which is experimentally known to be the location of the magnetic trap minimum (sec. 2.2) to within 0.5 mm, by measurements of heating of an electron plasma using microwaves [17]. Radial components will be denoted by the letter '$r$'.

No explicit mention to an azimuthal quantity is needed for the purpose of the analysis, and therefore no notation will be defined for azimuthal quantities. This, of course, does not mean that the system can be reduced to a two-dimensional model; the octupole magnet used for the anti-atom trap (sec. 2.2), for example, breaks the azimuthal symmetry and must be properly accounted for in the simulations. Correct descriptions of trajectories need to take into account the full three-dimensional configuration of the total magnetic field (ch. 3).

Finally, in order to avoid possible confusions, it is stated explicitly that the terms "anti-hydrogen atoms" and "anti-atoms" will refer to the same entity - the bound system formed by one antiproton ($\bar{\text{p}}$) and one positron ($\text{e}^+$). The two terms will be used interchangeably throughout this document.

# Chapter 2

# Experimental Methods

The synthesis of cold antihydrogen for trapping involves very careful procedures and manipulations of particles over a very wide range of energies. Any experimental apparatus designed to accomplish this task, where not only neutral particles but also charged particles (like the antiprotons and positrons required to synthesize the anti-atoms) are of interest, needs to be very flexible, and at the same time very robust and well diagnosed.

It is therefore not surprising that the ALPHA1 apparatus, which was built and operated exactly for this purpose, was a very complex machine. Its capabilities went beyond those of a common neutral particle trap, and allowed delicate manipulations that could in fact be used in a range of interesting studies like the ones described in appendix A, or others on the physics of non-neutral plasmas (see for example [18, 19, 20]).

Detailed descriptions of all the subsystems that came together to have a fully functional ALPHA1 apparatus are therefore lengthy and may lead the discussion too far away from the subject of this thesis. The interested reader can find excellent information in references [4, 21, 22]. For this work, it will be sufficient to restrict the attention to only those subsystems or procedures that are directly related to the studies of the charge of antihydrogen in later chapters.

## 2.1 Penning-Malmberg trap for charged particles

Cylindrical Penning-Malmberg traps are devices used for confining and storing charged particles [23]. They consist of a set of concentric hollow metallic cylinders (the "electrodes") whose electric potential can be individually controlled, and a strong uniform magnetic field in the direction of the axis of the electrodes (Fig. 2.1). Charged particles that are placed inside this "electrode stack" are radially confined by the strong magnetic field, and can be trapped or manipulated in the axial direction by electric fields produced with appropriate biases set on the electrodes. In order to reduce particle loss or unwanted interactions, the trap is usually kept under ultra high vacuum conditions.

The ends of the electrode stack are open, which allows for particles to be transferred into

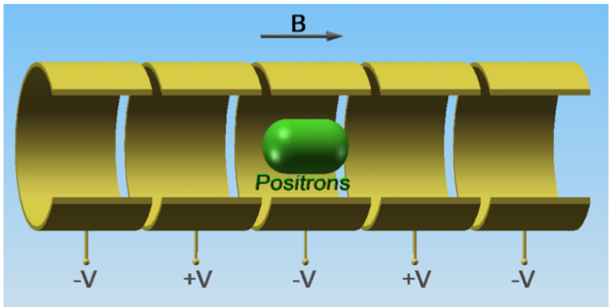

Figure 2.1: Schematic of a cylindrical Penning-Malmberg trap. Positively charged positrons are confined axially by appropriate biases on the electrodes and radially by the magnetic field $\vec{B}$. Adapted from [24].

or out of the trap. This feature was extensively used in ALPHA1 for experiments aiming at producing antihydrogen by carefully manipulating nonneutral plasmas of antiprotons and positrons obtained from the Antiproton Decelerator and the positron accumulator [25, 4], respectively. It also gave access to diagnostic devices that could be used to perform studies on the trapped particles [26, 8].

The ALPHA1 apparatus was built around a Penning-Malmberg trap with 35 electrodes placed in a 1 T solenoidal magnetic field (Fig. 2.2). The voltage in each one of the electrodes was set by a 16-bit Digital-to-Analog (DAC) converter connected to an amplifier with an output range of ±75 V or ±140 V, allowing control of the applied voltage to ±2 mV or ±4 mV respectively. Electrical noise could have adverse effects on particles in the trap [4], so the electrodes in the most sensitive areas were driven by the ±75 V amplifiers, which had a narrow-band output of approximately 2 kHz. Additional low-pass filters were placed between the output of all amplifiers and the electrodes, with cut-off (-3dB) frequencies of $\approx 25$ kHz, for increased noise immunity at the expense of longer response times, which limited the speed at which particle manipulations could be performed. The filters also had a high-pass input with a cut-off at $\approx 170$ kHz that was used to mix high-frequency and low-frequency signals on the electrodes.

Not all the electrodes were equal. Antihydrogen synthesis was carried out in the so called “mixing” region of the apparatus, where electrodes had a radius of 22.275 mm, slightly larger than the immediately contiguous electrodes in the stack, whose radius was 16.8 mm. Furthermore, not all the 13 electrodes in this “mixing trap” had the same axial length. Thus, biases on different electrodes had different contributions to the true electrostatic potential inside the trap, an effect that had to be taken into account when modeling the electric fields for manipulations of charged particles.

Timing in ALPHA1 was provided by the sequencer system [4], which controlled the triggering of instruments and reacted to their responses, and also controlled the timing and output voltages of the DACs that drove the electrodes. In each experimental run, a pre-

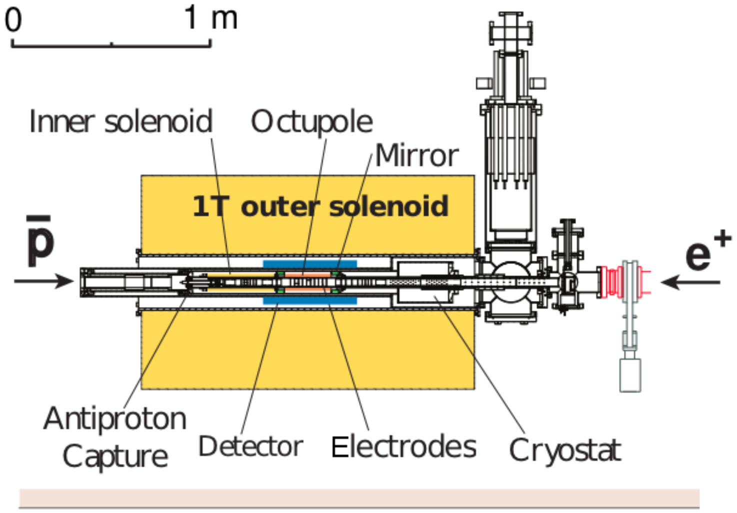

Figure 2.2: Schematic of the ALPHA1 apparatus. Antiprotons ($\bar{p}$) arrive at the left from the Antiproton Decelerator (AD) and positrons ($e^+$) come from the positron accumulator at the right. The main Penning-Malmberg trap can be seen inside the bore of the 1 T solenoid, at its axis. It is surrounded by the trap magnets (sec. 2.2) and silicon detector (sec. 2.3). Image from ALPHA Collaboration.

generated list of voltages for all electrodes was loaded and, once the "sequence" was started, the output of the DACs was updated correspondingly at a rate as fast as 2 $\mu$s, but typically less.

## 2.2 Magnetic trap for antihydrogen

The Penning-Malmberg trap in ALPHA1 provided means for storing and manipulating charged particles, including the antiprotons and positrons required for antimatter synthesis. However, antihydrogen was expected to be electrically neutral, which meant that once antiprotons and positrons were combined and formed a bound state, other techniques were needed in order to trap and study the resulting anti-atoms.

Trapping of antihydrogen in ALPHA1 was achieved [5] using the intrinsic magnetic dipole moment of anti-atoms. This can be understood by considering the quantum-mechanical Hamiltonian of an antihydrogen atom in its ground state (where the positron has reached the 1S atomic orbital), in the presence of a magnetic field [27].

$$\hat{H} = A(\hat{I} \cdot \hat{S}) - (\hat{M}_{e+} \cdot \vec{B}) - (\hat{M}_{\bar{p}} \cdot \vec{B}) \tag{2.1}$$

The first term in this expression is the "hyperfine" term, which arises from the interaction of the spins of the antiproton ($\hat{I}$) and positron ($\hat{S}$) in the atom. "$A$" is a constant resulting from the detailed calculation of the interaction. For the case of normal hydrogen atoms, in which the bound system is composed by a proton and an electron, $A$ has been measured experimentally to very high accuracy [28] and has a value of $(A\hbar)/(2\pi) = 1.420 \times 10^9$ Hz. Experiments in ALPHA1 established that, for antihydrogen, $(A\hbar)/(2\pi)$ has the same value as for hydrogen to within 100 MHz [8]. The determination of $A$ to higher accuracy for antihydrogen constitutes an important experimental challenge [11].

The second and third terms result from the interaction of the magnetic moments of the positron ($\hat{M}_{e+}$) and antiproton ($\hat{M}_{\bar{p}}$) with the magnetic field $\vec{B}$; the so called "Zeeman" terms. The magnetic moment of each particle is related to their spin through the expressions $\hat{M}_{e+} = g_{e+}\,(\mu_B/\hbar)\,\hat{S}$ and $\hat{M}_{\bar{p}} = g_{\bar{p}}\,(\mu_B/\hbar)\,(m_{e-}/m_{\bar{p}})\,\hat{I}$, where $\mu_B = 9.274 \times 10^{-24}$ J/T is the "Bohr magneton", $m_{e-}/m_{\bar{p}} = 5.446 \times 10^{-4}$ is the ratio of the electron to the antiproton mass, $g_{\bar{p}} = -5.586$ is the antiproton g-factor [15, 29], and $g_{e+} = 2.002 \approx 2$ [15] is the positron g-factor. Since the antiproton and positron are both particles with spin 1/2, the only possible outcomes of a measurement of $\hat{I}$ or $\hat{S}$ are $\pm\hbar/2$; thus, the numbers mentioned here show that the third term in (2.1) is smaller than the second one by a factor of $1.5 \times 10^{-3}$, and can be neglected.

By choosing $\vec{B} = B\hat{z}$, the Hamiltonian (2.1) can then be written as

$$\hat{H} \approx A(\hat{I} \cdot \hat{S}) - \mu_B|\vec{B}|(\frac{2\hat{S}_z}{\hbar}) \tag{2.2}$$

The eigenvalues of this operator give the allowed energies of a ground-state antihydrogen atom in the presence of a magnetic field:

$$\begin{aligned}
U_1 &= \frac{A\hbar^2}{4} + \mu_B|\vec{B}| \\
U_2 &= -\frac{A\hbar^2}{4} + \sqrt{(\frac{A\hbar^2}{2})^2 + (\mu_B|\vec{B}|)^2} \\
U_3 &= \frac{A\hbar^2}{4} - \mu_B|\vec{B}| \\
U_4 &= -\frac{A\hbar^2}{4} - \sqrt{(\frac{A\hbar^2}{2})^2 + (\mu_B|\vec{B}|)^2}
\end{aligned} \tag{2.3}$$

Even though it was assumed here that $\vec{B}$ was constant, the phenomenon of "adiabatic following" ensures that the magnetic moment of anti-atoms that are freely moving through the field will stay aligned with the direction of $\vec{B}$, so these expressions remain valid provided variations of the field are not too abrupt. Since antihydrogen atoms in the states $U_1$ and $U_2$ have a lower energy in regions where $|\vec{B}|$ is small, they tend to be attracted to regions of low magnetic field strength. For this reason, atoms in these states are called "low-field seeking". States $U_3$ and $U_4$ tend to be attracted to high magnetic fields and are therefore called "high-field seeking". In ALPHA1, magnets were designed such that a magnetic field with a minimum could be created and used to trap "low-field seeking" states of antihydrogen.

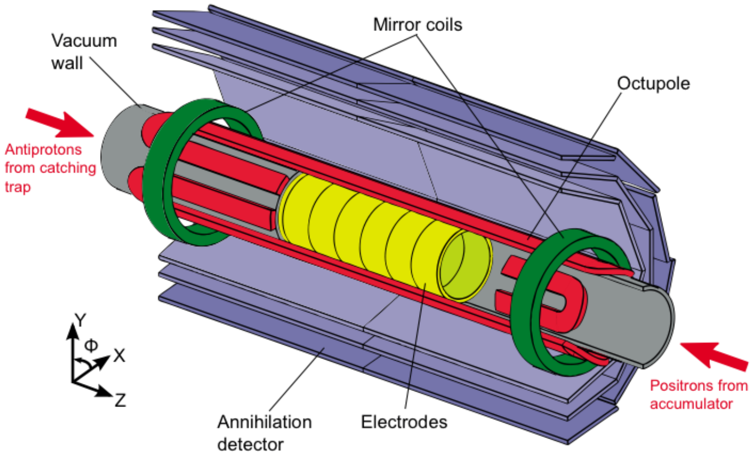

Figure 2.3: Trapping, or "mixing", region of ALPHA1. The magnetic field to trap anti-atoms is produced by contributions from the mirror coils, octupole and 1 T background field (not shown, see Fig. 2.2). The silicon annihilation detector is placed around the trap, outside the cryostat (not shown). Image from ALPHA collaboration [4].

The force that a "low-field seeking" antihydrogen atom experiences while moving through a magnetic field $\vec{B}$ can be calculated from $U_1$ and $U_2$ simply as $\vec{F} = -\nabla(U_1)$ and $\vec{F} = -\nabla(U_2)$. Typical magnetic fields used in our experiments had strengths greater than or equal to 1 T, so the first term inside the square root in the expression for $U_2$ is smaller than the second by a factor of approximately $(\frac{A\hbar^2}{2}/\mu_B)^2 = 2.6 \times 10^{-3}$, and can be neglected. The force then becomes simply

$$\vec{F} = \nabla(\hat{M}_{e+} \cdot \vec{B}) = -\nabla(\mu_B|\vec{B}|) = -\mu_B\nabla(|\vec{B}|) \tag{2.4}$$

where, for the term $\nabla(\hat{M}_{e+} \cdot \vec{B})$, it is understood that the anti-atom is in a low-field seeking state.

In order to produce a magnetic field with a minimum, ALPHA1 used two mirror coils and an octupole magnet superposed to the 1 T background field used for charged particle confinement [30]. The superconducting mirrors and octupole were placed coaxially around the electrodes of the "mixing trap" region as shown in Fig. 2.3.

The mirrors created a minimum of $|\vec{B}|$ in the axial direction, while the octupole created a minimum in the radial direction. Control of the currents through these magnets provided means to set the strength of the corresponding fields. For a typical run, the mirrors were set such that the peak on-axis field would be 1 T in the absence of contributions from other magnets. The octupole was set to produce a field of 1.54 T at $z = 0$, $r = 22.275\,\mathrm{mm}$ when energized independently. These settings corresponded to currents of 608 A through the mirrors and 890 A through the octupole (as measured by ±0.25% shunts). The addition

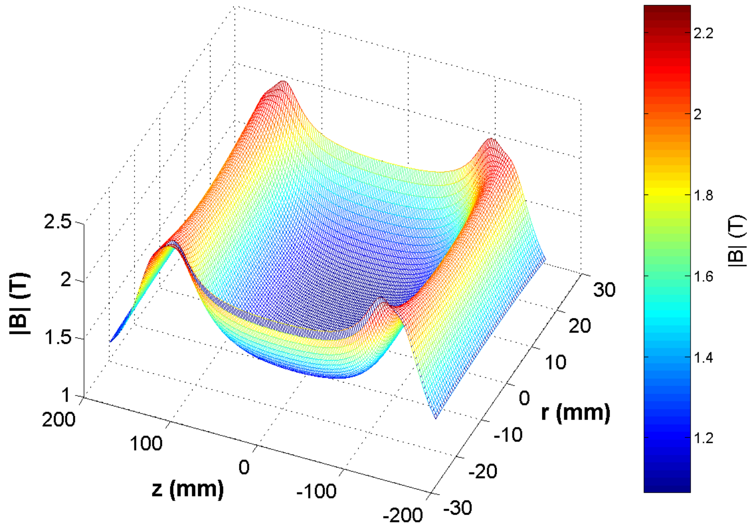

Figure 2.4: Slice of $|\vec{B}|$ for different values of $z$ and $r$. In this plot, $y = 0$, so $r$ corresponds to the distance from the axis in the $x$ direction (parallel to the ground). Due to the presence of the octupole, the shape of this "magnetic well" changes for different azimuthal angles.

of these fields plus the 1 T background field created the magnetic trap for antihydrogen shown in Fig. 2.4.

The depth of 0.54 K, in units of "Kelvin" instead of "Joules" (see sec. 1.2), was in reality limited by the strength of the octupole, which adds in quadrature to the axial field approximately as

$$\Delta U_{trap} = \mu_B(\sqrt{B_{oct}^2 + B_z^2} - B_z) \tag{2.5}$$

where $B_{oct}$ is the magnetic field strength of the octupole field at the electrodes and $B_z$ is the on-axis axial component of the field. This means that only antihydrogen created with a kinetic energy less than or equal to 0.54 K could be trapped in ALPHA1. Such a number shows how difficult it is to trap anti-atoms if one considers the energies involved in all the steps of antimatter creation, from antiproton generation, deceleration in the Antiproton Decelerator, cooling, and plasma handling, to the injection of antiprotons into the positron plasma for synthesis; in total, a difference of about 14 orders of magnitude in energy.

An electronic system provided protection for the mirrors and octupole against quenches by quickly forcing their current to go through a resistor network to dissipate the stored energy. That system was also used for the rapid shutdown of the magnetic trap for detection of trapped antihydrogen atoms, as explained in sec. 2.3. The currents through the mirrors and octupole would then decay approximately exponentially, with time constants of 8.8 ms and 9.5 ms [4]. In fact, it was seen in separate simulations that eddy currents generated on the electrodes by the changes in the magnet currents retarded the field decays, thereby

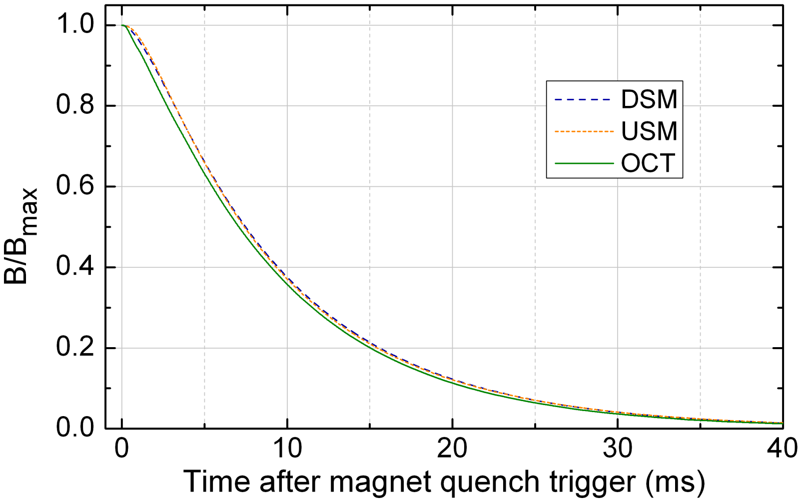

Figure 2.5: Decay of the trapping fields after a magnet shutdown trigger. The trace "DSM" corresponds to the downstream mirror coil (on the *positron* side); "USM" is the upstream mirror (on the *antiproton* side of the apparatus); and "OCT" is the octupole. In all cases, the curves represent the magnitude of the field produced by a specific magnet, normalized to the value at $t = 0$.

changing slightly the exponential behavior of the fields. This effect was especially important at early times, close to the start of the shutdown, as seen in Fig. 2.5.

## 2.3 Annihilation detector

When antiprotons undergo low-energy interactions with nuclei of normal matter atoms, they "annihilate" and produce energetic particles that travel away in different directions. On average, for each antiproton that interacts with a heavy nucleus, three charged and two neutral pions are created [22] which follow paths that start at a common vertex. The neutral pions in turn decay very rapidly into gamma rays, which can produce electron-positron pairs in the apparatus material.

In ALPHA1, trapped antihydrogen atoms were released at the time of the magnetic trap shutdown and drifted towards the trap walls until eventually coming into contact with the gold-plated aluminum Penning-Malmberg trap electrodes. The antiproton in each anti-atom would then annihilate and produce pions that could be used as signatures for detection. Indeed, ALPHA1 had a three layer silicon detector surrounding the electrode stack (Fig. 2.3) that was capable of detecting the passage of these charged particles. The system could reconstruct their trajectories (tracks) and find vertices where two or more of the tracks intersected. Each vertex would then be an estimate for the location of one antiproton annihilation, which in the case of the events recorded during a magnetic trap shutdown, was the indication of a trapped antihydrogen atom having been released from the trap and annihilating on the wall. The short duration of the trap shutdown (sec. 2.2) meant that cosmic rays and other backgrounds (with an acceptance estimated at $47 \pm 2\,\mathrm{mHz}$ [31]) were low and unlikely to produce a wrong detection. The annihilations were recorded in $0.1\,\mathrm{ms}$ bins.

Even though the detector itself could not distinguish between anti-atoms and bare antiprotons annihilating on the walls, the later could be ruled out thanks to a detailed study [32] which showed that no antiprotons were expected to confound the signal in antihydrogen trapping runs.

Very detailed descriptions of the detector hardware and vertex reconstruction software can be found in the references above ([31, 22]). However, the studies presented in later chapters are only concerned with the axial location $z$ of the annihilations, so it will be sufficient to concentrate on the performance of detection along $z$.

The first important issue is the efficiency of the detector at reconstructing vertices. Different materials present between the electrodes and the detector modules in the real ALPHA1 apparatus meant that particles produced in annihilation events might scatter differently and reduce the efficiency with which the system was able to detect annihilations in some regions of the apparatus. The non-uniformity of the magnetic field might also affect the trajectories of outgoing charged particles. Most importantly, it was known that one detector module (module 10) was not in operation in the years 2010 and 2011, affecting how well tracks passing through it (mainly those on the antiproton side) could be reconstructed. Monte Carlo simulations that included all these effects were run in order to create a curve of detector efficiency versus axial location $z$ [33].

Additionally, the detector was displaced with respect to the center of the mixing trap (corresponding to the center of electrode no. 18; see sec. 1.2). This offset was measured to be $2.395 \pm 0.024\,\mathrm{cm}$, towards the positron end of the apparatus, using annihilations of antiprotons with background gas in lifetime experiments. The finite length of the detector meant that axial locations towards the antiproton (or AD) end had less coverage and consequently, there was an additional contribution for a lower efficiency on that side. Adding this effect to the Monte Carlo simulations leads to a detector efficiency curve along $z$, in experiment coordinates, that describes how well the detector did at detecting annihilations in $z$ (Fig. 2.6).

The second important issue is the reconstructed vertex position resolution. Scattering of annihilation-produced particles in the apparatus and the finite hit resolution of the detector, among other effects, produce a broadening (or “smearing”) of the distribution of reconstructed vertices. This effect was studied with further Monte Carlo simulations, where annihilation events were generated and the location of the reconstructed vertices was compared to the original position. Experimental studies were performed using annihilations of antiprotons with background gas, which agreed to within better than 20% with the simulations [22]. As a result, a double-gaussian distribution function for the vertex position resolution was calculated, which is shown in Fig. 2.7.

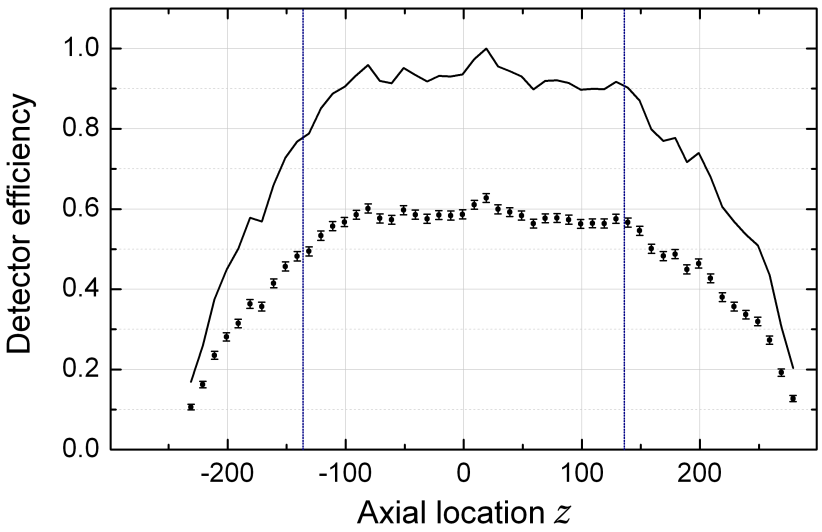

Figure 2.6: Detector efficiency along the axial direction $z$, in experiment coordinates. The points and error bars are the results of Monte Carlo simulations of annihilations and reconstructed vertices that use a full magnetic field and assume module 10 off (located on the *antiproton* side) [33]. The solid line is a linear interpolation of the simulation data, normalized such that the maximum is 1. The blue dashed vertical lines indicate the location of the "mixing" region, where most of the analysis takes place.

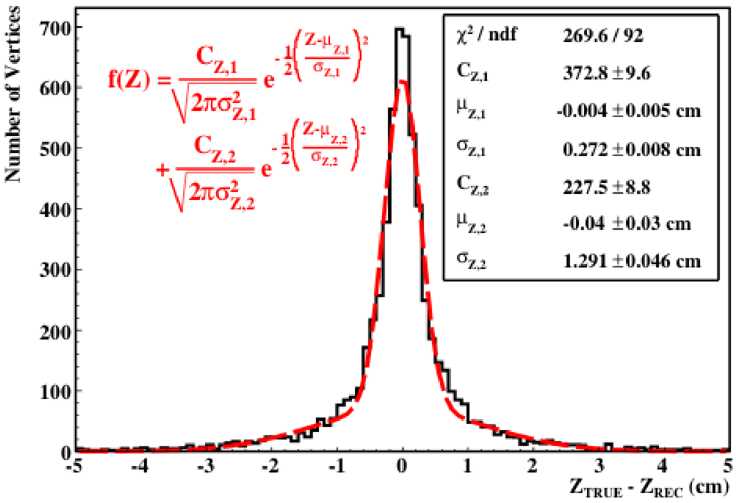

Figure 2.7: Detector smearing in the axial direction $z$. Taken from [22, ch.5]

## 2.4 Manipulations during antihydrogen trapping runs

Antihydrogen trapping experiments involved manipulating plasmas of antiprotons, obtained from CERN's Antiproton Decelerator facility, and plasmas of positrons, obtained from a Surko-type positron accumulator [25]. The steps leading to the synthesis of antihydrogen atoms is well documented and can be found in detail elsewhere [5, 6, 4]. Here attention is centered on the history of anti-atoms during and after synthesis.

The magnetic trap, which was kept off during all earlier manipulations, was energized by ramping up the mirrors and octupole currents to their nominal values (see section 2.2) and, after a short wait, the antiproton plasma was autoresonantly injected into the positron plasma [34]. The injection process was followed by a 1 s wait, during which antiprotons interacted and combined with positrons to produce antihydrogen atoms. Studies made using data from the 2010 [7, 32] and 2011 [9] runs gave strong evidence that anti-atoms were created with an initial energy that followed a thermal distribution at the positron temperature of $\approx$ 50 K. Since only atoms with kinetic energy less than or equal to 0.54 K could remain trapped (sec. 2.2), their initial energy ("$U$") distribution could be described approximately by the tail of a Maxwellian with a shape proportional to $\sqrt{U}$. Antihydrogen could also remain trapped for a significant amount of time in quasi-bound orbits with energies slightly larger than the trap depth (up to around 0.75 K), although in small proportions.

The initial energies of anti-atoms and the shallowness of the magnetic trap meant that, on average, less than 1 antihydrogen atom was trapped per attempt [5, 7, 8]. Most of the anti-atoms would have too large an energy and escape from the trap as soon as they formed; they could also re-ionize into antiprotons and exit. In fact, $\sim$ 5000 "mixing triggers" were detected per attempt as anti-atoms escaped immediately after forming and annihilated on the electrodes.

After the wait, a first set of electric potential manipulations (Fig. 2.8a) was done in order to gently eject the remaining positrons from the trap and measure their temperature [24, ch.3]. Theoretical calculations using a very pessimistic decay path showed that 99.5% of the anti-atoms would reach their ground state after 400 ms [7], so large electric fields were avoided at this early stage in order not to field-ionize weakly bound anti-atoms that might not have had enough time to reach stable states.

277.02 ms after the end of the 1 s "mixing", a first set of clearing fields was applied. An initial potential configuration was ramped in 2 ms, inverted 10 ms later (in a 2 ms interval), and cycled again after a 10 ms wait (Fig. 2.8b). The purpose of these manipulations was to get rid of any charged particles that could remain in the trap. Of special importance were antiprotons, which could lead to erroneous antihydrogen detections. This first set of "clearings", which lasted a total of 48.6 ms, was followed by another set with identical timings but stronger fields (Fig. 2.8c).

29.5 ms after the last set of clearings (403.72 ms after the end of mixing) a bias field was ramped and left on to deflect any possible remaining antiprotons as they were released during the rapid turn off of the magnetic trap. The bias QWP (Shutdown with Electric Potential) field could be "Bias-Right" (Fig. 2.8d) or "Bias-Left" (Fig. 2.8e), depending on the side of

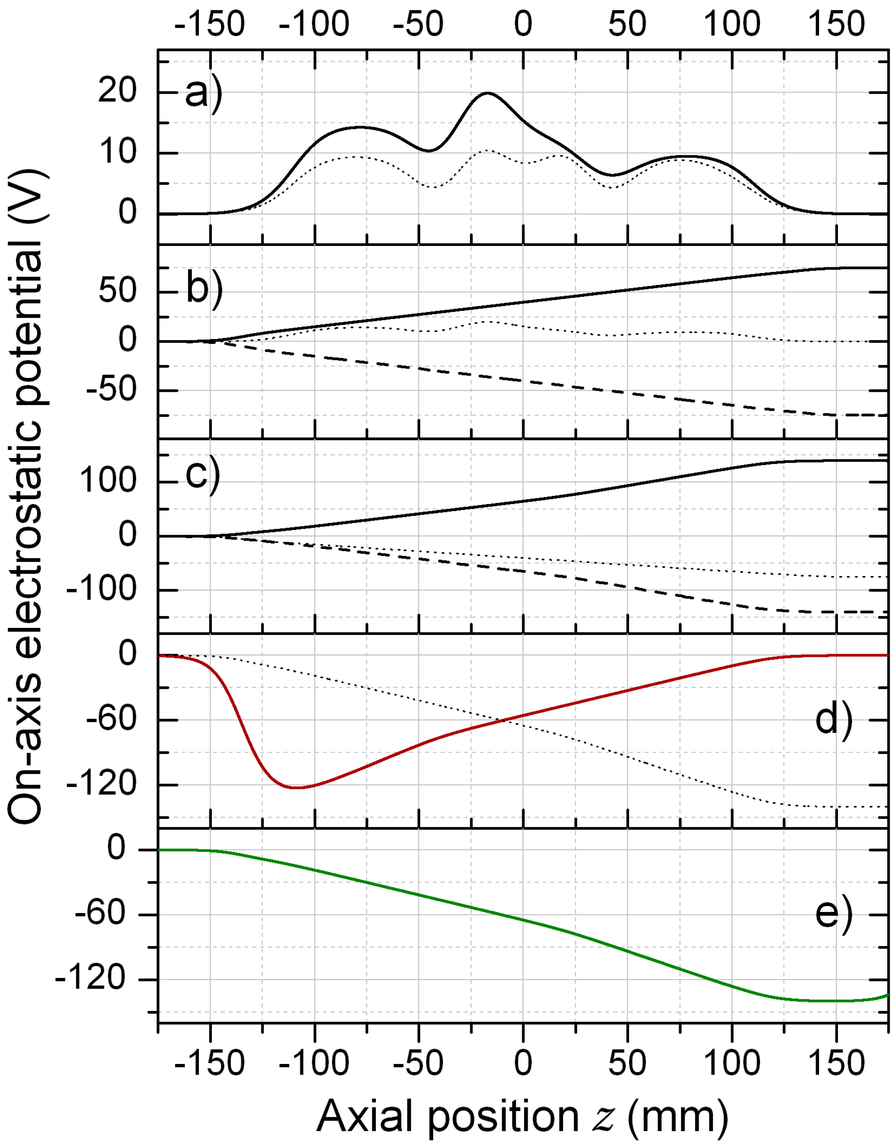

Figure 2.8: On-axis potential for each step (labeled 'a' through 'e'; see text for details) of the manipulations of the electrostatic field with trapped antihydrogen. Each part involved ramping the potential from an initial configuration (dotted lines) to a final one (solid lines), possibly passing through an intermediate level (dashed lines).

the trap (positron accumulator or AD end, respectively) towards which antiprotons would be pushed, providing a way to distinguish antihydrogen annihilations from bare antiproton ones [32]. The time interval between erecting the QWP bias and the magnet shutdown trigger usually lasted 13.1 ms, which was the time used for most simulations (sec. 3.3). However, a wait could be introduced in between for long confinement [7] and microwave runs [8] that could last up to 2000 s.

It is these bias fields, which were merely precautionary but used in most trapping experiments, that allow the search for a fractional charge of antihydrogen in chapters 3 and 4.

# Chapter 3

# Simulations

## 3.1 Simple analytic model

The electric field manipulations of section (2.4) would have an effect on trapped antihydrogen atoms if they carried a fractional electric charge $Q$. For example, if $|Q|$ were larger than $\sim 1 \times 10^{-6}$, the QWP bias potentials would be sufficient to push all anti-atoms out of the magnetic trap. This can be seen by considering the energy that anti-atoms would gain from the bias fields by going from the center of the trap to the walls. From Fig. 2.8, $\Delta\Phi_{bias} \approx 50\,\mathrm{V}$, and therefore $|Qe(\Delta\Phi_{bias})| > 0.54\,\mathrm{K}$, more than the depth of the trap $U_T$, and enough to allow any antihydrogen with $|Q| > 1 \times 10^{-6}$ to escape. As we observed trapped anti-atoms, this sets an upper "expulsion" bound on $|Q|$.

A better, although still simple, analytical estimate of the effect of the electric fields can be made by assuming that $Q < 1 \times 10^{-6}$, so that the effects of the field are less severe. This calculation will be useful in understanding and interpreting the simulation results described later in this chapter.

Under this assumption it is reasonable to focus on the last stage of the sequences, close in time to the magnetic trap shutdown when the bias potentials (QWP) are on. Including the effects of an assumed fractional charge $Q$, the potential energy of an antihydrogen atom in the trap is given by

$$U(z) = \mu_B B(z) - QeEz \tag{3.1}$$

where $U(z)$ is the potential energy that is assumed to only depend on the axial location $z$ for the purpose of this simple model, $E$ is the average electric field in the trap, and $e$ is the fundamental charge (as defined in sec. 1.2). When $Q = 0$, the potential energy has a minimum at $z = 0$; consequently, antihydrogen annihilations are centered around $z = 0$. A non-zero $Q$ would shift the annihilation center.

From eqn. 3.1, it is possible to solve for the shift $\Delta z$ in the minimum of the field $U(z)$ that results from a non-zero $Q$ in the presence of a Bias-Right ($E_R$) or Bias-Left ($E_L$) field. Combining results from the two cases leads to the $Q$ required to produce a given shift:

$$Q = \frac{2\mu_B \beta}{e(E_R - E_L)} \left(\Delta z_R - \Delta z_L\right) \tag{3.2}$$

where the magnetic field has been modeled as quasi-parabolic in the center of the trap, $B(z) = B_0 + \beta z^2$. Assuming further that this shift equals the difference in the mean of the annihilation locations measured experimentally for the Bias-Right and Bias-Left runs, i.e. $0.5\,[\Delta z_R - \Delta z_L] = 0.5\,[\langle z \rangle_R - \langle z \rangle_L] \equiv \langle z \rangle_\Delta$, an expression is obtained that directly relates the fractional charge $Q$ to an experimentally measurable quantity.

The bias fields average $E_R = -0.50\,\mathrm{V/mm}$, $E_L = 0.52\,\mathrm{V/mm}$ near the center of the trap (see Fig. 2.8), and $\beta = 1.6 \times 10^{-5}\,\mathrm{T/mm^2}$ from a fit done in the same region. Thus, eqn. 3.2 becomes $Q = -3.7 \times 10^{-9} \langle z \rangle_\Delta$, where $\langle z \rangle_\Delta$ is given in mm.

As will be seen in sec. 4.1, $\langle z \rangle_\Delta$ could be measured with a precision of a few millimeters. Therefore, this simple calculation gives a tighter estimate of the order of magnitude of $Q$, of around $\sim 10^{-8}$. Furthermore, this simple model gives an expected dependency of $Q$ on $\langle z \rangle_\Delta$ which will prove to be useful later in this chapter.

Nevertheless, the anti-atom dynamics in the trap are sufficiently complicated that numerical simulations are required for a more accurate calculation. These simulations are described in the following sections.

## 3.2 Model for simulations

The equation of motion of an antihydrogen atom in the trap with a possible fractional charge $Q$ is

$$m_{\bar{H}} \frac{d^2\vec{r}}{dt^2} = -\mu_B \nabla(|\vec{B}(\vec{r},t)|) + Qe\left(\vec{E}(\vec{r},t) + \frac{d\vec{r}}{dt} \times \vec{B}(\vec{r},t)\right) \tag{3.3}$$

where $\vec{r}$ is the center-of-mass position of the anti-atom and $m_{\bar{H}}$ is its mass. The first term on the right hand side is the magnetic trapping force, eqn. (2.4). The second term is the well known Lorentz force that a particle with charge $Qe$ would experience in the presence of electric ($\vec{E}$) and magnetic ($\vec{B}$) fields.

The purpose of the simulations is to integrate equation (3.3) and follow the full three-dimensional (3 D) trajectories of anti-atoms in the trap. This includes modeling precisely the time dependent 3 D electric and magnetic fields over the course of the manipulations described in sec. 2.4, and tracking down the axial location $z$ of the anti-atoms as they come into contact with the electrodes during the magnetic trap shutdown (sec. 2.2).

Electromagnetic effects, such as the induced electric fields produced by the rapidly changing magnetic field during the trap shutdown, can be included directly in $\vec{E}$ or $\vec{B}$. The total electric field $\vec{E}$, for example, has contributions from the instantaneous electrostatic potential, which can be calculated from the known electrode biases (sec. 3.3), and from $-\partial \vec{A}/\partial t$, where $\vec{A}$ is the magnetic vector potential [35]. The later term, however, is usually much smaller than the first for typical parameters used in our experiments, and its omission has no appreciable consequences in the simulation results (sections 4.3, 4.4). Magnetic fields generated by electric field changes have even smaller effects and can be neglected. Thus, only contributions from the externally applied potentials and magnetic fields are considered.

As discussed in sec. 2.4, experimental data suggests that antiprotons thermalize with the positron plasma during "mixing". Thus, anti-atom initial energies are modeled as following a Maxwellian distribution at the temperature of the positrons, truncated at 0.75 K (slightly bigger than the depth of the magnetic trap, to allow for quasi-bound anti-atoms that may be present). The initial location of anti-atoms is taken to be uniformly distributed in the region occupied by the positron plasma, roughly an ellipsoid of length 16 mm and radius 0.8 mm at the center of the trap [34]. Changes of the results due to variations of these initial conditions are explored in sections (4.3) and (4.4).

## 3.3 Implementation of the code

A code in C++ was developed in order to simulate the trajectory of individual antihydrogen atoms in the trap, as described in sec. 3.2. It implemented a symplectic propagator to integrate the anti-atom motion from randomly generated initial conditions consistent with the expected distributions [32, 36].

The magnetic field was implemented using analytic models for the mirrors and octupole [32] that explicitly depended on the bias currents. The rapid turn off of the trap was simulated by lowering the value of the octupole and mirror fields in an approximately exponential way, as discussed in sec. 2.2. The 1 T background field, which always remained on, was set in value and direction directly in the code.

The electric field was determined first by solving Laplace's equation for each set of electrode bias voltages used in the experiments, from "start" potential to soft clearings, strong clearings and QWP (see Fig. 2.8). The manipulations to diagnose the positron plasmas, which were carried out at comparatively much lower fields, were not included. A precise model of the trap in COMSOL [37], which relied on the cylindrical symmetry of the trap but otherwise took into account the true geometry, length and radius of the electrodes (sec. 2.1), as well as the gaps between them, was employed for this purpose, and used to calculate the electrostatic potential in a pre-established grid that spanned all the trapping volume. A set of interpolation coefficients (cubic splines) was then calculated on that grid for each one of the bias configurations. In fact, two sets of interpolation coefficients were calculated for each configuration of potentials: One set contained the contribution of the channels that used the ±75 V amplifiers, which had a narrower bandwidth and "slow" response times (sec. 2.1); the potential due to all other electrodes (called "fast" in comparison) was stored as a separate set.

The time evolution of the electrostatic potential was then included by loading all sets of interpolation coefficients into memory and implementing linear transitions between them, taking into account the true timings of the programmed voltage changes (sec. 2.4) and the different response times of the slow and fast electrodes. The instantaneous electric field at the position of the anti-atom was finally found by interpolation on this grid with time dependent coefficients.

Except for the electric field manipulations to diagnose the positron plasmas, the sequence implemented for the electric and magnetic fields closely followed the history of anti-atoms in the majority of experimental runs, from synthesis to release from the trap, and was incorporated into the basic algorithm of the code:

1. Configure constants and parameters. The fractional charge $Q$, the time step $t_{step}$, the number of trajectories to simulate *numtraj*, the currents through mirrors and octupole, for example, are set in this step.
2. Open references to the files that contain the sets of interpolation coefficients for the electrostatic potential, and load the sets of coefficients into memory.
3. Generate random initial conditions of position and velocity for one anti-atom, using the distributions discussed in sec. 3.2. Choose a start time of the simulation using a uniform distribution in the interval $(-1.1\,\mathrm{s},\ -0.9\,\mathrm{s})$, which gives on average a 1 s randomization time before the start of the potential manipulations of sec. 2.4. These manipulations begin at $t = 0$ with the "soft clearings".
4. Go forward one time step, using the symplectic integrator and the values of the current (at time $t$) electric and magnetic fields, calculated as described above.
5. Update the simulation time to $t = t + t_{step}$.
6. Check whether the anti-atom is still within the boundaries of the trap. If yes, go back to step (4). If not, print its $z$ coordinate and the simulation time $t$, and continue; this is the location and timing of a simulated anti-atom annihilation.
7. Check how many anti-atoms have been simulated. If fewer than *numtraj*, go to step (3). Otherwise, print total execution time and finish.

A time step $t_{step}$ of $3.5\,\mu$s was used for most simulations. As the energy of anti-atoms is bound by the depth of the trap to be $< 1\,\mathrm{K}$ ($= 1.381 \times 10^{-23}$ J), which roughly corresponds to speeds of $v < \sqrt{2U/m_{\bar{H}}} \approx 130\,\mathrm{m/s} = 450\,\mu\mathrm{m}/t_{step}$, this choice gave good detail of the trajectories and dynamics in the trap. Comparisons with results obtained using the different time steps $0.35\,\mu$s, $10.0\,\mu$s and $35.0\,\mu$s, showed no (within statistical noise) difference, providing further support to the choice of time step made. As a matter of fact, in order to see noticeable differences in the results, the step had to be increased to $t_{step} = 100\,\mu$s, a number sufficiently far to be of any concern.

Since the integration method used employed a fixed time step, the execution time scaled approximately linearly with simulation time and number of anti-atoms considered. In regular computers, integration of a single anti-atom trajectory would take approximately 2 s, showing that in order to obtain good simulation statistics ($\sim 5 \times 10^5$ points, as discussed later) for each value of fractional charge $Q$, many instances had to be run in parallel. The CERN batch system [38] was extensively used for this purpose. $\sim 100$ computer cores, each one running an independent instance of the code with 5000 anti-atom trajectories and different seeds for the initial conditions generators, could be run in parallel to produce the required number of simulated annihilations, for each value of $Q$ and choice of bias, in $\sim 3$ hours.

Other (different) machines were also used for testing, debugging, and also running proper simulations. In some cases the algorithm above had to be modified slightly in order to make good use of the available resources. For example, our research group's Dell PowerEdge R815 server with 4 AMD 64-bit Opteron 6276 processors (64-cores total) running at 2.3 GHz, allowed for compilation and execution of parallelized C++ codes using the Message Passing Interface (MPI) library. This required adding specialized instructions to the code that cannot be understood by standard compilers. Nevertheless, the algorithm implemented was essentially the same; the extra instructions only served the purpose of initializing independent parallel instances of the same program, running them and waiting for all instances to finish before exiting. This method, in fact, showed slightly better simulation speeds over the original method described above.

## 3.4 Results for nominal sequences

Figure 3.1 shows plots of annihilation times and axial locations $(t_{anh}, z_{anh})$ obtained with the simulations described in sec. 3.3, for different values of $Q$. No detector effects are included. The effect of the different electric field manipulations is clear, and gives an idea of the dynamics of fractionally charged antihydrogen in the trap.

If $Q \sim 10^{-7}$, the clearing fields are strong enough to force a significant number of anti-atoms out before the magnetic trap shutdown. This suggests an order of magnitude limit in the fractional charge better than the $10^{-6}$ mentioned in sec. 3.1; that is, the simulations suggest that observation of trapped antihydrogen is already indicative of $Q < 2 \times 10^{-7}$ (see sec. 5.1). For $Q \sim 10^{-8}$, most particles remain trapped until the start of the trap shutdown; very few anti-atoms escape due to the clearings. The study of $Q$ in that regime therefore requires attention on the annihilations occurring at late times in the sequences.

Figure 3.2 shows contour plots of the distribution of annihilations in $z$ at a time $t_q$ after triggering of the magnetic trap shutdown for particles with $Q \sim 10^{-8}$. The tendency of annihilations to be pushed toward one side of the trap by the bias fields is clearly seen when $Q \neq 0$, suggesting that a careful analysis of the axial location of anti-atom annihilations may allow the detection of an electric charge, if any.

If experimental data were abundant, it would in principle be possible to construct precise $(t_q, z)$ distributions like those in Fig. 3.2 and compare them with simulations that include detector effects (see sec. 3.5), using appropriate statistical methods to infer an experimental $Q$. However, experimental data was limited ($\sim 400$ data points), and comparison of experimental and simulated $(t_q, z)$ distributions was not necessarily the best way to perform the

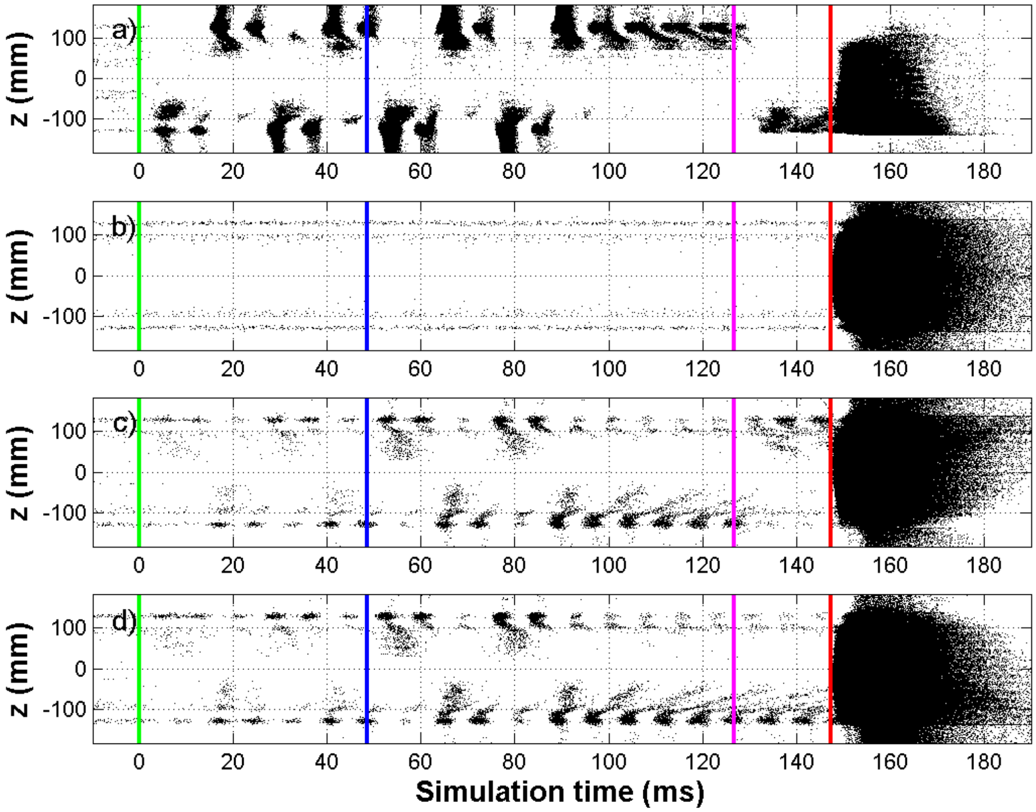

Figure 3.1: Simulated axial annihilation locations versus time for different values of fractional charge $Q$ and orientation of bias field: a) $Q = 2 \times 10^{-7}$, Bias-Right; b) $Q = 0$, Bias-Right; c) $Q = -3 \times 10^{-8}$, Bias-Right; and d) $Q = -3 \times 10^{-8}$, Bias-Left. Each black dot represents one particle that has escaped and annihilated at a particular time $t_{anh}$ and location $z_{anh}$. The colored vertical lines indicate the start times for different manipulations (see Fig. 2.8): Soft clearings in green, strong clearings in blue, ramp of bias field in magenta, and magnet shutdown trigger in red.

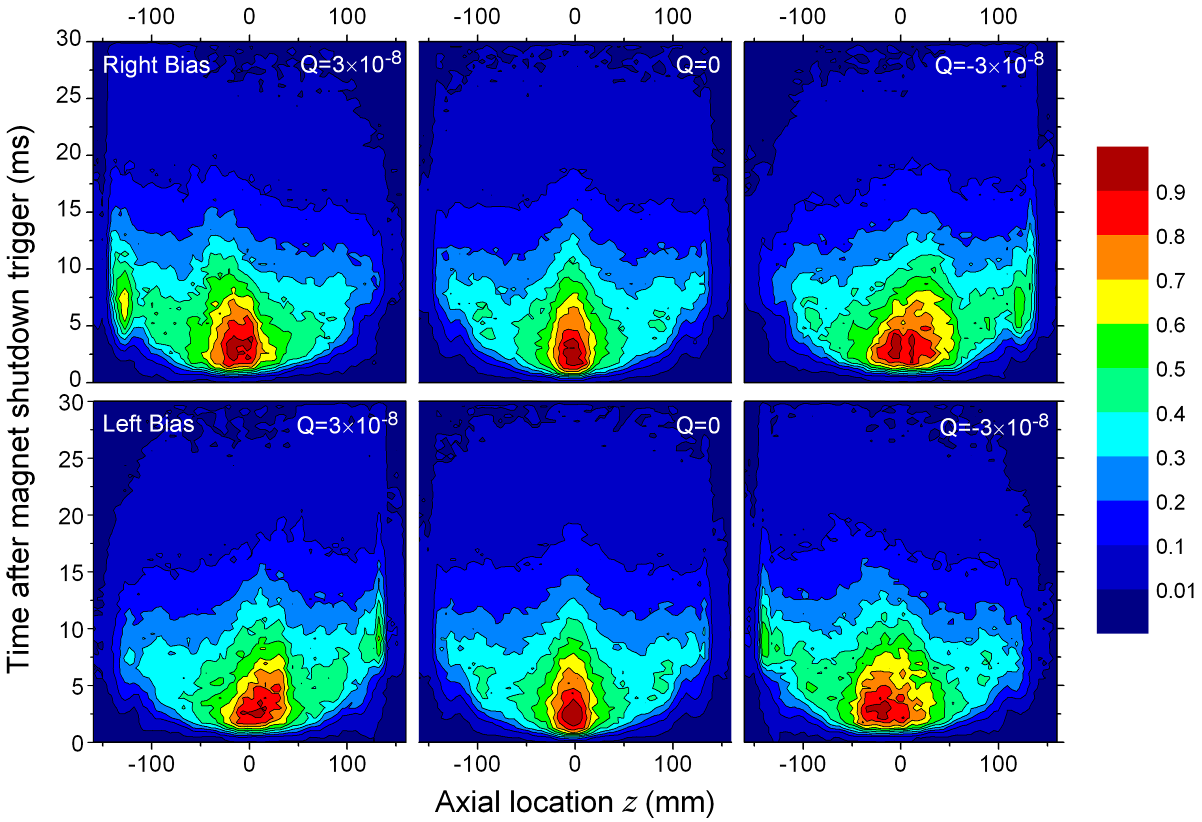

Figure 3.2: Heat plots of distribution of annihilations in time after magnet shutdown trigger $t_q$, and axial location $z$, for different $Q$. The top row corresponds to simulations for Bias-Right, while the bottom one was obtained with Bias-Left. The colormap is normalized to 1 for the highest density of annihilations, and changes linearly as indicated in the bar at the right; except for the darkest blue, which corresponds to all densities less than 1% of the maximum. The small differences between the $Q = 0$ plots are due to statistical differences between the two different data sets generated with Bias-Right and Bias-Left.

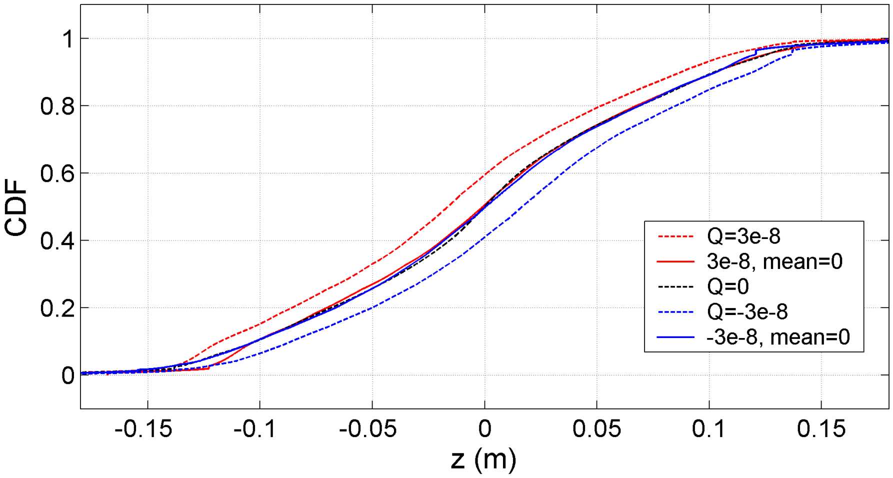

Figure 3.3: Comparison of cumulative distribution functions (CDFs) of axial location of annihilations for all $0 \leq t_q \leq 30\,\mathrm{ms}$ and different values of $Q$. Dashed lines correspond to curves obtained from original distributions, while solid lines correspond to distributions from which the mean has been subtracted.

analysis. Instead, the $t_q$ coordinate was integrated out and only the first moment of the marginalized distribution was considered, i.e. only the mean $z$ of the annihilations, $\langle z\rangle$.

This was motivated by the observation that the standard deviation, skewness and kurtosis of the simulated $z$ distributions for different values of $Q$ did not show appreciable differences that could be clearly resolved with the number of available experimental data points. Also, as Fig. 3.3 shows, CDFs for different $Q$ look very similar once the effect of the mean is subtracted, suggesting that focusing on the simple $\langle z\rangle$ would not lead to a significant loss of the statistical power that could be obtained by performing, for example, a more complicated Kolmogorov-Smirnov test [9].

In addition to being simple, using $\langle z\rangle$ provides a good way to reduce systematic effects. If some *constant* offset $z_0$ were introduced in the experimentally measured $z$, the average location of the annihilations would become $\langle z\rangle + z_0$. However, if two sets of experimental data were correctly chosen such that one could subtract their means without eliminating the signal, then the effect of $z_0$ would go away; that is $\langle z_1 + z_0\rangle - \langle z_2 + z_0\rangle = \langle z_1\rangle - \langle z_2\rangle$ exactly.

Figure 3.2 shows that the Bias-Right and Bias-Left configurations have approximately inverse effects on the mean displacement of fractionally charged antihydrogen. By choosing the sets “Right” and “Left”, and defining $\langle z\rangle_\Delta \equiv 0.5\,[\langle z\rangle_R - \langle z\rangle_L]$, one obtains a quantity that is nonzero, that can be calculated from the simulations, and that directly relates something measurable to a value of $Q$. Furthermore, this quantity, as mentioned above, is in principle immune to *constant* offsets in annihilation locations.

The simulated $\langle z\rangle_\Delta$ for several values of $Q$, without taking into account detector effects, is shown in Fig. 3.4. Each point in the plot is the average of approximately 450 000 simulated anti-atom annihilations which were selected from a larger list using the requirements that $0 \leq t_q \leq 30\,\mathrm{ms}$ and $|z| \leq 136\,\mathrm{mm}$; this selection is explained in detail in sec. 4.1. The extremely large number of annihilations used in each calculation assures that each point on the plot is a normally distributed random variable with standard deviation equivalent to the sample statistical error of the annihilation locations divided by the square root of the number of annihilations. This "standard error of the mean" is used to quantify the 1-$\sigma$ error of the simulations:

$$\mathrm{Err}_{R,L} \approx \frac{S}{\sqrt{N_{anh}}} \approx \frac{66\,\mathrm{mm}}{\sqrt{450\,000}} \approx 0.10\,\mathrm{mm} \tag{3.4}$$

where $S \approx 66\,\mathrm{mm}$ is the sample average of the simulated annihilation distributions, which does not change significantly for different values of $Q$ or choice of bias. Thus, $\mathrm{Err}_{R,L} = 0.1\,\mathrm{mm}$ is essentially equal for all points in the plot corresponding to a Bias-Right or Bias-Left result. Since $\langle z \rangle_\Delta$ is calculated from the individual averages of the two bias configurations (which are in principle independent variables), the error is the result of adding those errors in quadrature. As argued above, the error is the same for all values of $Q$.

$$\mathrm{Err}_{\langle z \rangle_\Delta} = 0.5\sqrt{\mathrm{Err}_R^2 + \mathrm{Err}_L^2} \approx 0.07\,\mathrm{mm} \tag{3.5}$$

Figure 3.4 shows that the variation of $\langle z \rangle_\Delta$ with $Q$ is very approximately linear, in agreement with the estimate from sec. 3.1. The calculation of the fit, which is pinned to the origin consistent with the physical expectation that $Q = 0$ should give equal results for Bias-Left and Bias-Right (and supported by the simulations to within statistical error) gives $Q = (-2.771 \pm 0.034)\,(10^{-9}\,\mathrm{mm}^{-1}) \times \langle z \rangle_\Delta$. This result provides a way to measure $Q \sim 10^{-8}$ when values of $\langle z \rangle_\Delta \sim 1\,\mathrm{mm}$ can be resolved.

A plot similar to this one, that includes detector effects and appropriately selected "cuts" on the data will be used for the estimation of the fractional charge $Q$ of antihydrogen in chapter 4.

## 3.5 Adding detector effects

The lists of annihilation times and axial locations $(t_q, z)$ obtained with the simulations described in sec. 3.3, and shown in sec. 3.4, correspond to the locations and timings of annihilations of antihydrogen atoms after the start of the magnetic trap shutdown. However, experimental data necessarily came from the silicon detector which, as described in sec. 2.3, introduced effects that need to be accounted for in order to correctly compare simulations to real data.

Detector effects are added to the simulations in the following way:

1. A random number from a $[0, 1]$ uniform distribution is generated for each pair $(t_q, z)$ and compared to the value at $z$ of the detector efficiency curve rescaled to have a

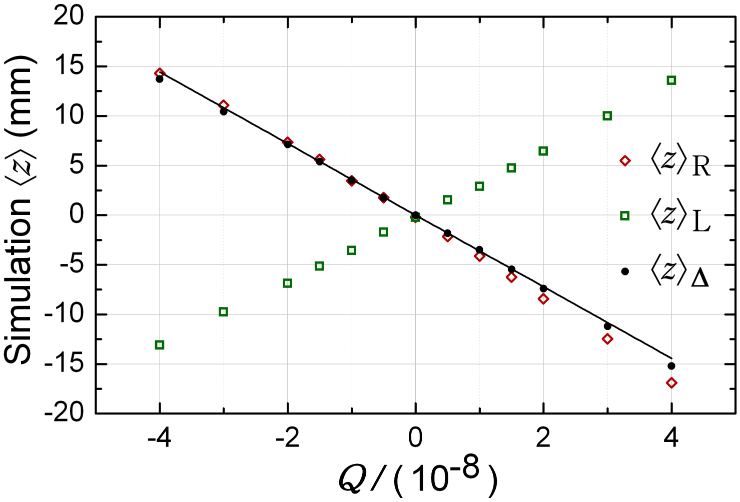

Figure 3.4: Average location of annihilations for different values of $Q$, without including detector effects. Red diamonds are Bias-Right simulations, green squares are Bias-Left, and black circles are $\langle z\rangle_\Delta = 0.5\,[\langle z\rangle_R - \langle z\rangle_L]$. The statistical error of $\pm 0.1\,\mathrm{mm}$ ($\pm 0.07\,\mathrm{mm}$ for $\langle z\rangle_\Delta$) of each point is too small to be shown with clarity. The black line is the least-squares linear fit of the $\langle z\rangle_\Delta$ points.

maximum value of 1 in Fig. 2.6. If the random number is larger than the efficiency at that point, the pair is discarded; otherwise it is kept.

2. For every pair that is kept, a random number $z_{smear}$ is generated using the smearing distribution of the detector in $z$ (Fig. 2.7), and added to $z$.

The list of accepted pairs $(t_q, z + z_{smear})$ would then include detector efficiency and smearing, and give a sample of the data that is expected to be seen experimentally under different hypotheses of values of fractional charge for antihydrogen.

In reality, however, this list would be one particular instance corresponding to a set of random numbers generated from one particular seed. In other words, slightly different sets of accepted pairs would be obtained if different seeds were used. In order to get rid of this effect, the mean annihilation locations (for each $Q$) that include detector effects are calculated as averages over many instances generated from different seeds. The spread associated to this procedure would then in principle need to be added to the final calculation of the error of each point, as it would bring an extra uncertainty to the simulation results. However, it was seen that by using $\sim 20$ instances the error would be negligible compared to the standard error of the means of the distributions. This is the reason why averages over 20 instances are used in all calculations performed on quantities affected by the detector.

# Chapter 4

# Measurement of the fractional charge of antihydrogen

The methods developed in ch. 3 provide an expected dependency of $\langle z\rangle_\Delta \equiv 0.5\,[\langle z\rangle_R - \langle z\rangle_L]$ on $Q$. By inverting the relation, those results can be used to calculate the fractional charge $Q$ from the knowledge of $\langle z\rangle_\Delta$, a quantity that can be determined experimentally.

In this chapter, the calculation of $Q$ from $\langle z\rangle_\Delta$ is performed using experimental data collected with the ALPHA1 apparatus during the 2010 and 2011 runs, and studies are presented of the possible sources of systematic errors that affect this result.

It is important to note that all the theoretical and statistical procedures were developed *before* analyzing the experimental data. Decisions on the validity of data that could be included in the analysis (the "cuts") were taken and fixed before proceeding to an actual calculation. This "blind analysis" [39] is a standard procedure done in order not to introduce biases towards preconceptions that may exist about the final results. In particular, this requires that data not be left aside without an unbiased justification.

The discussions of this chapter are the main subject of [40].

## 4.1 Experimental data

Experimental data for the fractional charge measurement was taken in the years 2010 and 2011, in experiments aimed at trapping [5, 6, 7] antihydrogen atoms and studying their interactions with microwaves [8].

As mentioned in detail in sec. 2.4, every experimental attempt, which could be repeated on average every 15 minutes, involved carefully combining plasmas of antiprotons and positrons to produce $\sim 1$ trapped antihydrogen atoms. The surviving anti-atoms would then undergo several electric field manipulations, after which they would be released from the magnetic trap and their annihilation by-products detected by the silicon detector system (sec. 2.3). The vertex reconstruction algorithms run on this recorded raw "hit" data, would then output a list of annihilation times (in 0.1 ms bins) and locations (with $z$ resolution shown in Fig. 2.7), that satisfied the criteria of an antihydrogen atom having annihilated on the trap walls. This data would of course be affected by the imperfect efficiency of the detector (Fig. 2.6).

The criteria used in the vertexing algorithms were set to reduce as much as possible the cosmic-ray background. Dedicated studies [22, 31] led to optimized "cuts" in the data that permitted a background rate of $47 \pm 2\,\mathrm{mHz}$ and an acceptance of $64.4 \pm 0.1\%$ of the true recorded annihilation events. One of the "cuts" chosen to reduce backgrounds was the selection of events occurring only in the time window $0 \leq t_q \leq 30\,\mathrm{ms}$, where $t_q$ is the time after the magnet shutdown trigger (sec. 3.4). This explains the selection performed on the simulated data shown in Figs. 3.2 and 3.4, and is the reason why only annihilation times in that window are considered in everything that follows in this chapter.

In order to only include "events" that are compatible with the fractional charge analysis, further cuts are needed on the list of reconstructed vertices.

First, only experimental runs where a QWP bias potential was applied are considered. Even though experiments without these biases have not been mentioned in detail, some 2010 runs were made without including them. They were a part of a campaign to rule out antiproton contamination in the experiments that led to the first demonstration of antihydrogen trapping [5]. Since the analysis developed in ch. 3 relies on the effects that the bias potentials would have on antihydrogen if it were electrically charged, runs with no bias cannot be straightforwardly included, and are therefore "cut out" from the list of events.

Antihydrogen atoms are born in excited, sometimes weakly bound, states [7]. As explained in sec. 2.2, the trapping force experienced by anti-atoms relies on the interaction of the magnetic field with their magnetic moment, which is modified from that described by eqn. (2.4) when the positron occupies a state with orbital angular momentum "$l$" different from 0. It is therefore important to make sure that antihydrogen has enough time to cascade down to the ground state, through radiative and collisional processes, for the dynamics to be correctly described by eqn. (3.3). Theoretical calculations using a very pessimistic decay path show that 99.5% of anti-atoms reach the ground state after 400 ms (sec. 2.4). Therefore, only events for which the hold time is greater than 0.4 s are included in the final list. Other plausible decay paths have decay times of as low as $\sim 25\,\mathrm{ms}$, showing that the selection could possibly be relaxed to increase the number of events compatible with the charge studies.

In total, there were $\sim 1300$ trapping attempts compatible with the selection criteria of bias field and hold times. Accumulating the detection time windows of 30 ms over all attempts and using the cosmic acceptance rate of 47 mHz, there is an expected contamination of $\approx 2$ cosmic rays in the list of events.

This estimate, however, is conservative as it does not take into account spatial cuts. Simulations show that antihydrogen annihilations can occur at axial locations as far as $z = \pm 200\,\mathrm{mm}$ or more. Nevertheless, as explained in sec. 2.1, there exists a change in radius of the Penning-Malmberg trap electrodes at the locations $z \approx \pm 138\,\mathrm{mm}$ that forces a concentration of annihilations at those locations, complicating the analysis. The choice is therefore made to *only* include data that fulfills $|z| \leq 136\,\mathrm{mm}$. It must be stressed that the simulations show that an overwhelming fraction of events are left untouched by this selection; less than 5% of the total simulated events are left out. This interval corresponds, also, to the region of the trap where the detector is the most efficient (see Fig. 2.6), and where the percentage of reconstructions that are far from their true position is smallest [32].

In addition to cosmic rays, there is special concern for antiproton contamination, since the detector is not able to distinguish between the annihilation of an antihydrogen atom and that of an antiproton (sec. 2.3). Thorough studies of the dynamics of antiprotons in the trap [32] showed that in the very unlikely event that antiprotons survived the clearing fields (sec. 2.4), they would be swept towards the ends of the trap by the bias field and annihilate preferentially around $z = \pm 130\,\mathrm{mm}$. In fact, the studies showed that 95% of deliberately trapped antiprotons annihilated within elliptical regions centered at $z = \pm 130\,\mathrm{mm}$, $t_q = 5\,\mathrm{ms}$, with semi-axes 20 mm, 4 ms. Thus, the decision is made to exclude events that fall in those *elliptical* regions in order to enhance rejection of unwanted antiprotons.

In discussions within the collaboration, concerns were raised for data taken in runs with microwaves. The first issue brought into consideration was the possibility that microwaves could force antihydrogen atoms to undergo a quantum transition into a de-trapping, "high field seeking" state (see sec. 2.2) during the trap shutdown. In that case, anti-atoms would be detected, but would not be correctly described by eqn. (3.3) and the simulations of ch. 3 would no longer be valid. However, all experimental sequences used for microwaves included a 1 s wait between turning off the microwave source and triggering the magnet shutdown. This is enough time for microwave power (at a frequency $\sim 29\,\mathrm{GHz}$) to dissipate in the cavity formed by the electrode stack (with quality factor unknown, but certainly no better than 10k) before the onset of the trap shutdown.

The second concern were possible forces experienced by anti-atoms in the microwave field. The electric field of the microwaves was estimated to have an amplitude of $\leq 150\,\mathrm{V/m}$ [7], significantly smaller than the DC values of the bias fields (Fig. 2.8). Since any effects brought about by the microwaves, that do not involve forcing quantum transitions, would enter as ponderomotive forces, which are second-order, averaging effects (and therefore much smaller than a DC effect), they have negligible consequences.

Also, there were possible perturbations to the anti-atom dynamics due to degraded vacuum conditions caused by the microwaves. It was observed experimentally that the pressure in the trap increased slightly when microwaves were on, an effect presumably linked to the raise in temperature of the electrodes and possible gas desorption from their surface. The small increase in gas density in the trap would increase the probability that an antihydrogen atom collide with a gas atom or molecule, perturbing its motion and altering the dynamics described by eqn. (3.3). However, calculations [41] using $> 9\,\mathrm{K}$ helium as the main species in the residual gas (see appendix A), showed that the rate of anti-atoms that remained trapped after colliding was $\leq 5\,\%$ the rate of being lost. This is due to the fact that anti-atoms that undergo a low-energy collision have a significant probability either of annihilating with the gas atom, or gaining enough energy from it to escape from the trap (whose depth is 0.54 K; see sec. 2.2). Thus, any antihydrogen surviving until the trap shutdown is very unlikely to have been affected by vacuum degradation, and there is no reason to leave aside events recorded in microwave runs.

This line of reasoning also applies for events recorded in very long hold time runs ($\sim 1000\,\mathrm{s}$

or more). Since a collision with a gas atom or molecule would force an anti-atom to be lost with very high probability, detection at the magnetic trap shutdown is indicative that the anti-atom did not undergo collisions that significantly affected its dynamics during the time it remained trapped. Therefore, "long hold time" events can be safely included.

Finally, it was observed that in some 2011 runs an intermittent failure of the detector occurred where data from two modules (modules 6 and 14) failed to be recorded properly. Studies showed that this was an unbiased problem, not related to any particular events but rather occurring in random runs, that could be recognized by observing the behavior of the modules in individual experiments. As the failure of two modules (in addition to module 10, which was always off as mentioned in sec. 2.3) would introduce changes in the experimental conditions, it was decided not to include events recorded in runs where there were indications that the problem existed.

In summary, the list of experimental data consists of candidate reconstructed vertices that meet the following requirements:

1. The run used Bias fields.
2. The anti-atom hold time was longer than 0.4 s.
3. The event occured at a time $t_q$ (after triggering the magnetic trap shutdown) such that $0 \leq t_q \leq 30\,\mathrm{ms}$.
4. The reconstructed vertex had axial location $z$ such that $-136\,\mathrm{mm} \leq z \leq 136\,\mathrm{mm}$.
5. The reconstructed vertex laid outside the elliptical regions centered at $z = \pm 130\,\mathrm{mm}$, $t_q = 5\,\mathrm{ms}$, with semi-axes 20 mm, 4 ms.
6. No signs of intermittent detector readout error was observed prior to the magnetic trap shutdown.

A total of 386 experimental events fulfill these criteria. They correspond to:

- Events recorded in Bias-Right runs: 241
  - Bias-Right events in 2010: 27
  - Bias-Right events in 2011: 214
- Events recorded in Bias-Left runs: 145. All of the Bias-Left runs were carried out in 2010.

In passing, it is worth mentioning that 112 (29%) of anti-atoms were held for times longer than 1 s. These correspond to 87 Bias-Right and 25 Bias-Left events.

Figure 4.1 shows the timings and axial locations of the experimental events in the final list. The calculation of the mean locations of annihilations for the Bias-Right and Bias-Left configurations yields $\langle z \rangle_R = 7.91 \pm 4.22\,\mathrm{mm}$ and $\langle z \rangle_L = -0.21 \pm 5.30\,\mathrm{mm}$, where the

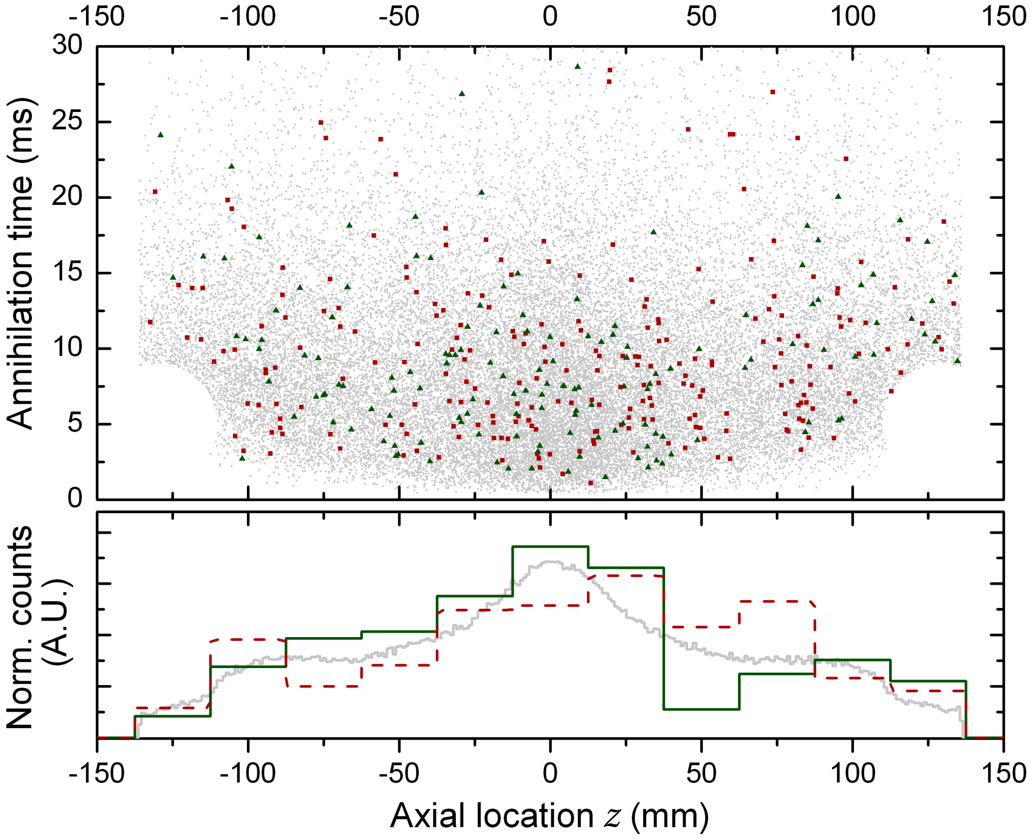

Figure 4.1: Top plot: Timings and axial locations of the experimental Bias-Left (green triangles) and Bias-Right (red squares) events in the final list considered for the measurement of the fractional charge of antihydrogen. The background gray dots are simulation results, including detector effects and cuts (notice the cut-out ellipses around $z = \pm 130\,\text{mm}$), for $Q = 0$. Bottom plot: Normalized histograms of experimental annihilation locations for Bias-Left (solid green line) and Bias-Right (dashed red), in arbitrary units. The gray curve is the histogram of simulated annihilations for $Q = 0$, rescaled for purposes of qualitative comparison. These plots were created only after consensus was reached within the collaboration to "unblind" the analysis.

error associated to each value is the standard error of the mean, equivalent to the standard deviation of the data divided by the square root of the number of events included in the calculation. Then $\langle z\rangle = 0.5\,[\langle z\rangle_R + \langle z\rangle_L] = 3.85 \pm 3.39\,\mathrm{mm}$, where the error is the result of propagating the errors of the means:

$$\sigma_{\langle z\rangle} = 0.5\,\sqrt{\sigma^2_{\langle z\rangle_R} + \sigma^2_{\langle z\rangle_L}} \approx 0.5\,\sqrt{\frac{S_R^2}{241} + \frac{S_L^2}{145}} \tag{4.1}$$

In this expression, $S_R = 65.5\,\mathrm{mm}$ and $S_L = 63.9\,\mathrm{mm}$ are the sample estimators of the true standard deviations of the distribution of annihilations under Bias-Right and Bias-Left conditions. In reality, since the variances as well as the means are estimated from the data, $\langle z\rangle$ is better described as being distributed T-student. However, the large number of degrees of freedom safely allows the approximation to a normal distribution with standard deviation $\sigma_{\langle z\rangle}$.

Also, $\langle z\rangle_\Delta = 0.5\,[\langle z\rangle_R - \langle z\rangle_L] = 4.06 \pm 3.39\,\mathrm{mm}$. Although 0 is not covered by the 1-$\sigma$ confidence region, it is indeed in the 90% confidence interval, which is calculated upon multiplication of the error bounds by a factor of 1.64. This result will be of great importance in sec. 4.2.

As seen throughout the discussion in this section, the list of annihilation events consists of data collected for purposes other than the specific one of measuring the fractional charge of antihydrogen. This makes the analysis sensitive to errors that could have been avoided from the beginning by a more careful choice of data collection procedures. For example, since the method requires $\langle z\rangle_\Delta$ to be calculated from experimental data, possible drifts in time that affected unevenly the Bias-Left and Bias-Right data sets might introduce an offset, a problem that could have been avoided by alternating different bias runs. In fact, as discussed above, the entire Bias-Left data set was collected in 2010, while most of the Bias-Right data was collected in 2011. A careful analysis is therefore needed to rule out any effects that may have caused drifts over time in the data described in this section. This is examined in sections 4.3 and 4.4.

## 4.2 Comparison with simulations

Applying detector effects (sec. 3.5) to the simulated data in sec. 3.4, and then applying the cuts from sec. 4.1, leads to the simulation results shown in Fig. 4.2. The extra cuts plus detector effects reduce the number of points that are used in the calculation of the simulated mean annihilation locations to $\approx 430\,000$, which is slightly lower than the number used in sec. 3.4. However, the application of the elliptical cuts reduces the sample standard deviation in a way that slightly outweighs the lower number of simulated events and makes the standard errors of the simulations approximately equal (actually slightly smaller) to the numbers mentioned in ch. 3.

A least squares linear fit of the simulated $\langle z\rangle_\Delta$ versus $Q$, constrained to pass through $\langle z\rangle_\Delta = 0$, $Q = 0$ consistent with the expectation that the bias electric fields have no effect

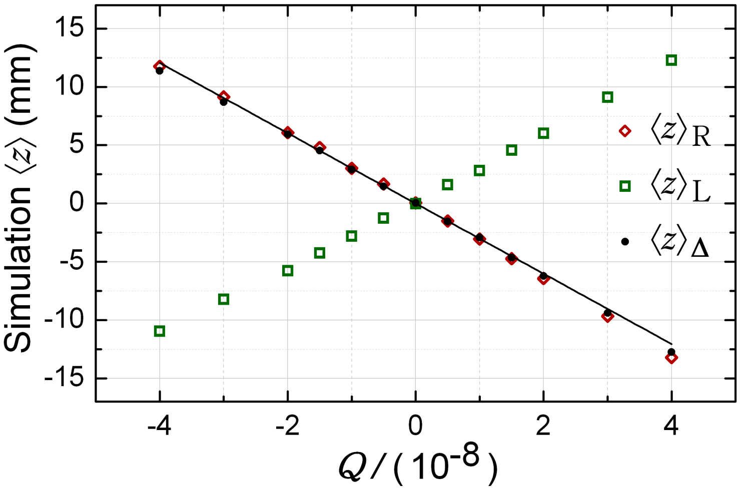

Figure 4.2: Average location of simulated annihilations for different values of $Q$, including detector effects and appropriate cuts. Red diamonds correspond to Bias-Right simulations, green squares to Bias-Left, and black circles to $\langle z \rangle_\Delta = 0.5\,[\langle z \rangle_R - \langle z \rangle_L]$. The statistical error of ±0.1 mm (±0.07 mm for $\langle z \rangle_\Delta$) of each point is too small to be shown with clarity. The black line is the least-squares linear fit of the $\langle z \rangle_\Delta$ points.

for $Q = 0$ (and supported by the simulations to within statistical error), gives a very good description of the data and leads to $Q = (-3.31 \pm 0.04)\,(10^{-9}\,\mathrm{mm}^{-1}) \times \langle z \rangle_\Delta$, where the error in the slope corresponds to one standard error of the fit.

Using this result, the experimentally calculated value of $\langle z \rangle_\Delta = 4.06 \pm 3.39\,\mathrm{mm}$ (sec. 4.1) yields $Q = (-1.34 \pm 1.12) \times 10^{-8}$. With 90% confidence bounds, $Q = (-1.34 \pm 1.84) \times 10^{-8}$

This number is consistent with $Q = 0$, in agreement with the expectations from sec. 1.1. The uncertainty comes from the precision with which $\langle z \rangle_\Delta$ is measured; it is due mainly to the reduced number of experimental data available, as discussed in sec. 4.1. Thus, in principle, this same method could be implemented in the new apparatus (ALPHA2) to yield tighter bounds on $Q$ by increasing the number of experimental data points.

It is interesting to note the implications of this result regarding the charge of the positron. Under the very likely assumption that the charge of antihydrogen is equivalent to the sum of the charges of its constituent particles, $Qe = q_{\bar{p}} + q_{e+}$, so

$$\left(\frac{q_{e+} - e}{e}\right) = Q - \left(\frac{q_{\bar{p}} + e}{e}\right) \tag{4.2}$$

Since the charge anomaly of the antiproton is known to be $|(|q_{\bar{p}}| - e)/e| \leq 7 \times 10^{-10}$ (a comparatively higher precision; see sec. 1.1), equation 4.2 allows to determine the charge anomaly of the positron as $(q_{e+} - e)/e \approx Q = (-1.3 \pm 1.8) \times 10^{-8}$ (90% confidence). This measurement agrees with previous numbers found in the literature (sec. 1.1) and constitutes a bound on the charge of the positron that is better than the previously recognized charge anomaly of $< 4 \times 10^{-8}$ [15]. No confidence level was given to the previous number, so a strict comparison with the new result is not straightforward; however, using the 90% uncertainty in the current measurement gives a factor of $\sim 2$ improvement in the precision of the experimentally measured positron charge.

Systematic effects, however, have not been taken into account yet. They need to be incorporated into the results in order to set the final bounds on the charge of antihydrogen. This is the subject of the next sections.

## 4.3 Calculation of systematic errors

Systematic effects can be classified into four groups, which are presented in order of descending importance:

A. Effects that cause the sensitivity $s \equiv dQ/d\langle z\rangle_\Delta$ to be different from that of the nominal simulation results discussed in sec. 4.2, and that are assumed to be *constant* in time. One example of this type of error is an inaccurate knowledge of the magnet currents.

   (Notice that $s$ has been defined as the *reciprocal* of the slope of the line in Fig. 4.2.)

B. Offsets in $\langle z\rangle_\Delta$ introduced by changes in time of experimental conditions. Generally speaking, these errors are due to offsets that affect differently the values of $\langle z\rangle_R$ and $\langle z\rangle_L$ and do not cancel when calculating $\langle z\rangle_\Delta$. A variation of the performance of the detector would be a typical example. Even though the changes may happen continuously, they are modeled using the extreme case of a discontinuous jump between 2010 and 2011; thus, the change only affects the Bias-Right data.

C. Changes in time of the sensitivity $s$. These effects are also assumed to change discontinuously between 2010 and 2011, and therefore, only affect the Bias-Right data. Consequently, their contribution is expected to be less than half the size of Type A errors, making this type of error negligible. These errors are not considered further.

D. Effects that cause an error in $\langle z\rangle$ but not in $\langle z\rangle_\Delta$. They are useful for evaluating the understanding of the experiment, but they do not not matter for the calculations of $Q$ and its experimental bounds.

Roughly speaking, these four categories account for changes in the slope and y-intercept of the line that relates $Q$ to $\langle z\rangle_\Delta$ (see Fig. 4.2). It is conceivable as well that some effects might cause changes to the shape of curve. However, linear models are adequate for all systematics considered; as will be seen in what follows, there are no effects that cause changes requiring the use of a model of higher order than linear.

The quantitative calculation of the errors starts by estimating differences with respect to the nominal results in sec. 4.2, either by using physical arguments or by running simulations with the proposed source. The numbers $\epsilon_z$, corresponding to absolute offsets in the average location of annihilations, and $\epsilon_s$, corresponding to relative changes in the sensitivity (i.e. $\epsilon_s \equiv (s/s_{\mathrm{Nom}}) - 1$), are thus obtained and used to proceed with the calculation of the different types of systematics and the final contribution to the error in $Q$; this is shown in table 4.1. The calculation takes into account the definitions of $\langle z\rangle$, $\langle z\rangle_\Delta$ and the proportion of experimental data taken in 2010 with respect to 2011 (see sec. 4.1).

| **Type** | $\delta\langle z\rangle_L$ | $\delta\langle z\rangle_R$ | $\delta\langle z\rangle_\Delta$ | $\delta s_L$ | $\delta s_R$ | $\delta Q$ |
|---|---|---|---|---|---|---|
| **A** | - | - | - | $s_{\mathrm{Nom}}\epsilon_s$ | $s_{\mathrm{Nom}}\epsilon_s$ | $s_{\mathrm{Nom}}\epsilon_s\langle z\rangle_\Delta$ |
| **B** | - | $\frac{N_{2011}}{N_R}\epsilon_z$ | $0.5\,\frac{N_{2011}}{N_R}\epsilon_z$ | - | - | $s_{\mathrm{Nom}}\,(0.5\,\frac{N_{2011}}{N_R}\epsilon_z)$ |
| **C** | - | - | - | - | $s_{\mathrm{Nom}}\frac{N_{2011}}{N_R}\epsilon_s$ | $0.5\,s_{\mathrm{Nom}}\frac{N_{2011}}{N_R}\epsilon_s\lvert\langle z\rangle_\Delta\rvert$ |
| **D** | $\epsilon_z$ | $\epsilon_z$ | 0 | - | - | 0 |

Table 4.1: Procedures for calculating the changes induced in $Q$ ("$\delta Q$") by the different types of systematic effects. Errors in $z$ ("$\epsilon_z$") and in the sensitivity $s$ ("$\epsilon_s$") produce changes in the average location of annihilations under Bias-Left ($\delta\langle z\rangle_L$) and Bias-Right ($\delta\langle z\rangle_R$) configurations, and changes in the sensitivity for Bias-Left ($\delta s_L$) and Bias-Right ($\delta s_R$). Temporal changes are assumed to occur discontinuously between 2010 and 2011 and only affect a fraction ($N_{2011}/N_R = 214/241 = 0.89$) of the Bias-Right data (see sec. 4.1).

The estimation of the errors $\epsilon_z$ and $\epsilon_s$ is done based on numbers that often have uncertainties. The simulation results, for example, have sampling errors associated to the finite (although large) number of antihydrogen trajectories simulated, as well as errors associated to the fit into a line. The propagation of the errors (using standard techniques, such as the "delta method") into the calculations in table 4.1 often lead to uncertainties larger than the value calculated. In those cases, the effect is labeled as "statistically insignificant", as it is not possible to know whether the systematic has a real effect in the experiment or not. These "insignificant" errors are conservatively taken into account by using the value of their uncertainty instead of the central number.

The list of all sources of systematic effects considered, as well as their contribution to the systematic uncertainty in $Q$, is shown in table 4.2. Detailed descriptions of the different sources of error are given in sec. 4.4. Here only numbers are presented in order to obtain a final result. The numbers $\delta Q$ in table 4.2 are calculated following the definitions in table 4.1. As mentioned before, uncertainties instead of central values are reported for results that are statistically insignificant (blue entries). Entries for which simulations showed a statistically significant value are shown in brown. The rest of the entries are calculated based on an independently measured parameter, which some times has an uncertainty compatible with zero, in which case the effect may not be real (black). In other cases (red entries), the parameter is incompatible with zero, giving a result that is very likely to have caused a change in the results.

By adding all the $\delta Q$ in quadrature, a final 1-$\sigma$ error of $\pm\,0.34\times10^{-8}$ is obtained. Going to 90% confidence (upon multiplication by 1.64) yields a total systematic error of $\pm\,0.56\times10^{-8}$.

| **Error source** | Type A $\epsilon_s$ ($10^{-9}\,\mathrm{mm}^{-1}$) | Type B $\delta\langle z\rangle_\Delta$ (mm) | Type D $\epsilon_z$ (mm) | Total $\delta Q$ ($10^{-8}$) |
|---|---|---|---|---|
| **Simulations** | | | | |
| 10 s hold time | - | - | ±0.04 | 0 |
| Code benchmarking | ±0.01 | ±0.09 | ±0.20 | ±0.03 |
| Degraded $\vec{E}$ field | ±0.01 | ±0.10 | ±0.24 | ±0.03 |
| Antihydrogen in $U_1$ state | ±0.01 | - | ±0.07 | ±0.01 |
| **Magnetic fields** | | | | |
| ±1% asymmetry in mirror currents | - | ±0.13 | ±0.29 | ±0.05 |
| ±1% common mode mirror error | ±0.01 | ±0.02 | ±0.03 | ±0.02 |
| 2 mrad background $\vec{B}$ tilt | ±0.01 | ±0.07 | ±0.15 | ±0.03 |
| ±1% error in octupole current | - | ±0.01 | ±0.03 | ±0.01 |
| External magnets | - | ±0.06 | ±0.11 | ±0.02 |
| **Initial conditions** | | | | |
| 3× radius, 2× length | ±0.01 | ±0.07 | ±0.15 | ±0.03 |
| Initial energy distribution | ±0.22 | ±0.04 | ±0.05 | ±0.31 |
| **Location errors** | | | | |
| Detector zero relative to trap zero | - | ±0.17 | ±0.2 | ±0.06 |
| Magnetic trap center relative to trap zero | - | - | ±0.5 | 0 |
| **Detector** | | | | |
| Detector efficiency | ±0.02 | ±0.03 | ±3.6 | ±0.04 |
| Detector drift | - | ±0.04 | ±0.09 | ±0.01 |
| **Other errors** | | | | |
| Cosmic-ray contamination | - | ±0.25 | - | ±0.08 |
| Antiproton contamination | - | ±0.13 | - | ±0.04 |

Table 4.2: Calculation of the contribution of the different sources of systematic errors to the total systematic uncertainty in the measurement of $Q$. See text for details.

This is small compared to the counting error of $\pm 1.84 \times 10^{-8}$ from sec. 4.2, corroborating the statement that the measurement of $Q$ is limited by the sample size.

Putting everything together, the fractional charge $Q$ of antihydrogen is measured to be $Q = (-1.34 \pm 1.84 \pm 0.56) \times 10^{-8}$ with 90% confidence. This result is consistent with $Q = 0$. The charge anomaly of the positron (see sec. 4.2) is then $(q_{e+} - e)/e = (-1.3 \pm 1.8 \pm 0.6) \times 10^{-8}$ with 90% confidence.

## 4.4 Detailed description of systematic effects

Calculations and numbers for the different systematic effects are presented in sec. 4.3. In this section, a more complete description of the different effects is given, following the order in which they are shown in table 4.2. There is also an additional discussion on the effects of placing "cuts" on the data; this does not add any contributions to the list of systematic errors, but it leads to an interesting study that is useful for understanding the predictions based on the simulations and some of their limitations.

In the discussions that follow, "insignificant" will refer to an effect whose value cannot be distinguished from the uncertainty of the estimation (see sec. 4.3). "Small" will refer to an effect that may be statistically significant, but whose contribution to the total systematic error is small.

### Simulation benchmarking

The nominal simulations of ch. 3 closely mimic the complete history of approximately 71% of anti-atoms in the final list considered for the charge measurement. The remaining 29% were held for longer times by introducing a wait between the end of the bias-field ramp and the magnet shutdown trigger (see sec. 2.4). Simulations of anti-atoms held for an additional 10 s showed no significant differences when compared to the nominal results.

Also, a comparison was performed with results obtained with a simplified version of the electric fields. In that case, the electrodes were assumed to have no change in radius, causing significant errors in the field at large values of $z$. Additionally, the effects of the electrode gaps were only approximated and not carefully implemented as in the case of the nominal model. Only small errors associated to these effects were seen.

Additionally, simulations were run for anti-atoms in the low-field seeking state $U_2$ in eqn. 2.3 without approximating the energy to that of the $U_1$ state. No significant differences were observed.

Although the code used for the simulations was similar to some previously benchmarked versions [32], it was anyway cross-checked against a different one using a 4th-order, adaptive step Runge-Kutta integrator. That code included a more accurate magnetic field model, and electric fields induced by changes in the magnetic field. An insignificant type A error, as well as small type B and D effects were observed.

Data used in the benchmarks in [32] provides good evidence that the simulations, coupled to the standard efficiency curve (Fig. 2.6), match the experimental results. However, it is interesting to explore the consequences of making predictions based on a model that yields results different from some assumed "actual" results. This is studied, in this case, by making "predictions" based on the nominal simulations (Fig. 4.2) and comparing them to data with a different spread (i.e. a different standard deviation). The procedure is the following: A sensitivity is obtained using the nominal simulations (plus detector effects) and used to calculate a "Predicted $Q$"; the results are then compared to "Actual $Q$" data calculated using altered versions of the annihilation distributions for each $Q$ and direction of bias field, such that they have a different width. The different distributions are generated from the original lists of points by applying the following transformation to the annihilation locations (this has to be done for each $Q$ and direction of bias field):

$$z_{new} = z_{old} + a \sin\left(\pi \frac{z_{old}}{136\,\mathrm{mm}}\right) \tag{4.3}$$

For small values of the parameter $a$, like the ones employed in what follows, this transform has the property that the $z$ do not flip sign, and that $z$ which fulfill $|z| \leq 136\,\mathrm{mm}$ remain in $|z| \leq 136\,\mathrm{mm}$. Fig. 4.3 shows the effect of choosing $a = -10\,\mathrm{mm}$ (blue histogram) and $a = 16\,\mathrm{mm}$ (red histogram), compared to the original simulations (green). The two modified distributions are very different from the experimental distributions obtained in [32], so they bracket plausible changes.

It is important to note that no elliptical cuts are considered for this analysis, since they have a sizable effect on the standard deviation that may mask some of the interesting changes.

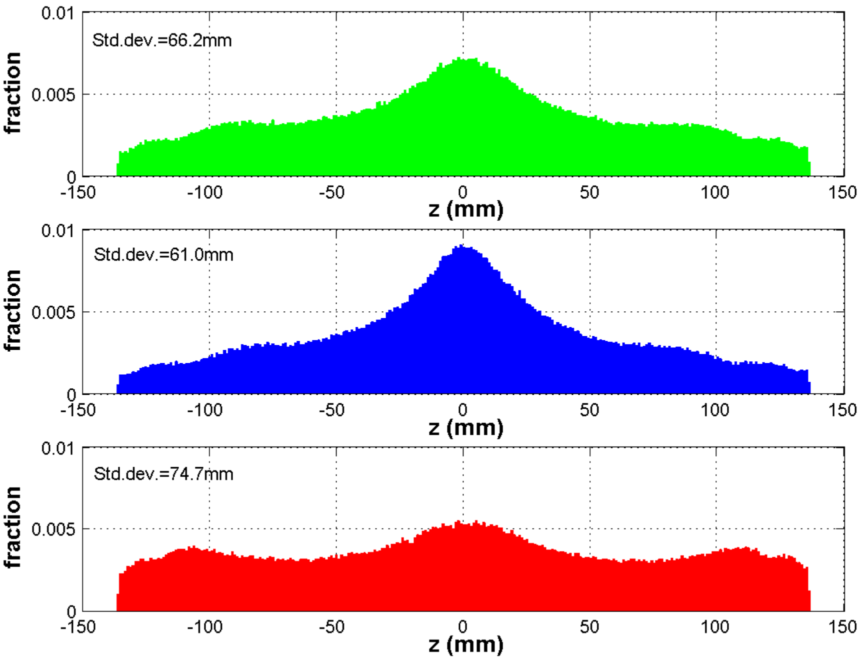

Figure 4.3: Normalized distributions of annihilation locations obtained from the original $Q = 0$ (top, green) by applying the transform $z_{new} = z_{old} + a \sin(\pi\, z_{old}/136\,\mathrm{mm})$. The reduced standard deviation in the middle plot (blue) is obtained by choosing $a = -10\,\mathrm{mm}$. The choice $a = 16\,\mathrm{mm}$ in the bottom plot (red) causes the noticeable increase in the spread. In all cases detector efficiency and smearing are included, as well as the cut $|z| \leq 136\,\mathrm{mm}$ (but *no* elliptical cuts).

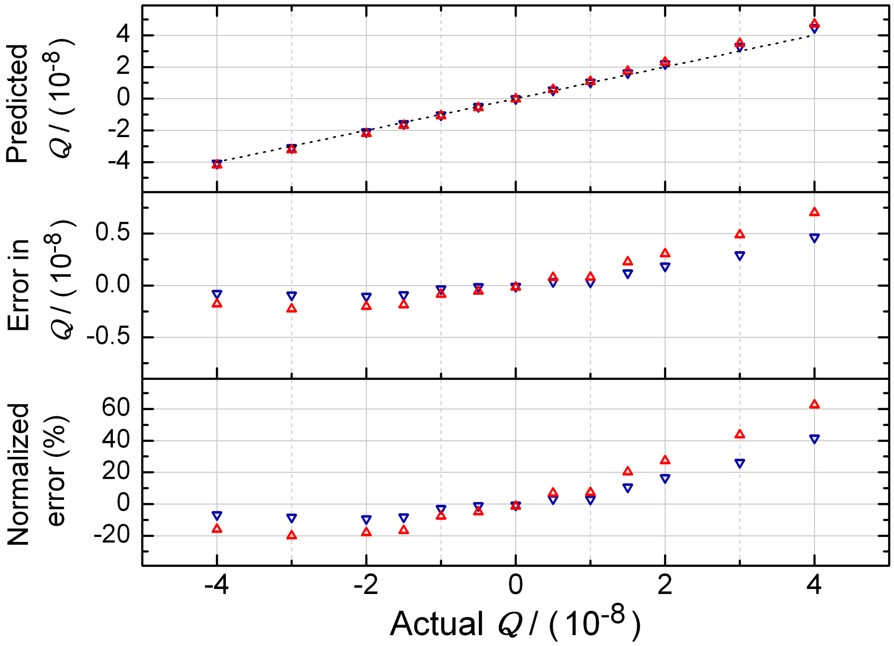

Figure 4.4: Predicted $Q$ versus Actual $Q$ when real anti-atom annihilations are assumed to have a distribution different from the one modeled by the simulations (top plot). The red triangles (pointing up) correspond to larger spread data as indicated in Fig. 4.3; blue triangles (pointing down) are obtained with distributions with smaller standard deviation. The dashed line is a slope one line (not a fit of the data) that would correspond to perfect agreement between predicted and actual points. Departures indicate errors, which are shown in the middle plot. The bottom plot shows the errors normalized to the measured statistical error in $Q$ (see text).

The top plot in Fig. 4.4 shows the Predicted $Q$ against Actual $Q$ obtained with the bracketing distributions. The fact that the points are very close to a straight line with slope one implies that Predicted $Q \approx$ Actual Q. The middle plot shows the error (Predicted $Q -$ Actual $Q$), and the bottom plot shows the error normalized by the statistical error of the measurement of $Q$. It is important to note that this analysis was initially performed *before* unblinding the experimental data; the error in $\langle z\rangle_\Delta$ was estimated to be in the order of 3.5 mm from the sample size and simulated standard deviation of $z$ for individual annihilation events (obtained with nominal simulations and detector effects). This gave a statistical error of $Q$ of $\approx \pm 1\times10^{-8}$, which is very close to the actual calculation in sec. 4.2, which gave a value of $\pm 1.12\times10^{-8}$. This last *measured* number, however, is the one used for the normalization in Fig. 4.4. That means that if the normalized error were one, the systematic error engendered by using the wrong annihilation distributions for the calculation of the fractional charge would be equal to the measured statistical error.

It is important to limit the range of the Actual $Q$; if the values were very large, the corresponding errors would also be large. From sec. 1.1, it is expected that $|Q| < 4 \times 10^{-8}$. Furthermore, sec. 4.2 showed that the measurement of $Q$ is consistent with 0 with a statistical uncertainty equivalent to the one mentioned in the last paragraph; thus, it makes sense to consider $Q$ in the range $\pm 1 \times 10^{-8}$, which leads to a normalized error in $Q$ in the range $[-2.9\%, 2.9\%]$ for the $a = -10\,\mathrm{mm}$ case, and in the range $[-7.7\%, 7.2\%]$ for $a = 16\,\mathrm{mm}$.

Thus, even if the antihydrogen simulations were off by amounts inconsistent with the experimental measurements, the errors in $Q$ would still be significantly smaller than the statistical error.

## Magnetic field errors

Errors in the currents through the mirror coils and octupole change the shape of the magnetic trap and are a source of systematics. Of special importance are mismatches in the strength of the mirror fields, which would cause the magnetic minimum to be displaced axially and introduce an offset in the location of the annihilations.

The magnitude of the errors is limited by the fact that the coils were driven by individual power supplies with accuracies of ±0.5%. Furthermore, continuous low precision measurements of the currents set a maximum variation of ±1.0% throughout the two years of the run [42]. Simulations using the maximum deviations allowed by the observations, both for differential and common mode variations of the mirror magnets, as well as for changes in the octupole, showed small type A, B and D errors.

Another source of error, which simulations showed to be insignificant, is the maximum tilt of 2 mrad (mechanically constrained) of the background 1 T field.

Finally, there are possible type B and D errors caused by external magnets. However, they are very small, as exemplified by the effect of a 1 m long, 1 T solenoid with a bore of diameter 40 cm, which was not there in 2010 but was then left in close proximity of the apparatus in 2011. At 2 m, such a magnet would create a shift $\epsilon_z < 0.1\,\mathrm{mm}$, a very small offset. Needless to say, nothing like that was placed close to the experiment.

## Initial conditions for the simulations

As mentioned in sec. 3.2, antihydrogen is modeled as being created in the space occupied by the positron plasma, approximately an ellipsoid of length 16 mm and radius 0.8 mm where particles are distributed uniformly. Simulations run using a larger initial volume (an ellipsoid with 3 times the radius and 2 times the length) showed insignificant type A, B and D differences.

The initial energy is modeled as being maxwellian at the temperature of the positrons, truncated by the depth of the trap. Previous studies gave strong evidence in favor of this choice (sec. 2.4). Also, as Fig. 4.5 shows, the experimental cumulative distribution function (CDF) of annihilations versus time (after the trap shutdown trigger) is very well modeled by simulations with $Q = 0$ and a maxwellian distribution. Nevertheless, two other choices

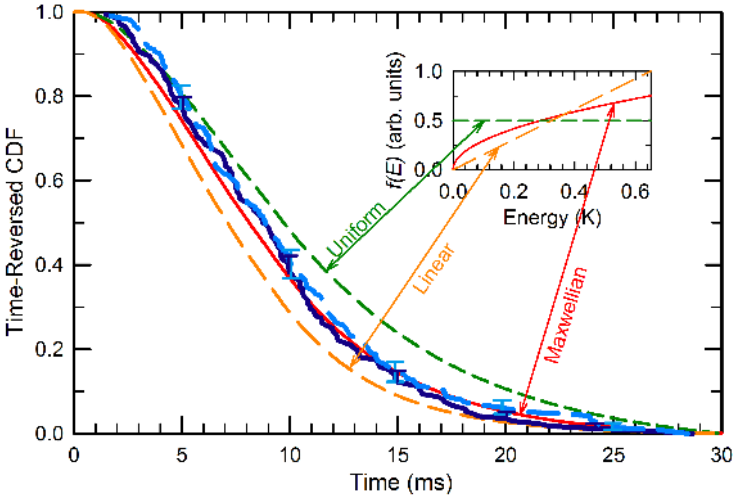

Figure 4.5: Time reversed cumulative distribution function (CDF) of annihilation times of simulated and measured antihydrogen. Results obtained for $Q = 0$ using a maxwellian distribution for the initial energies (solid red line) give a very good description of the experimental data from 2010 (solid dark blue) and 2011 (dashed light blue). Simulations using uniform (dashed green) and linear (orange) distributions are farther, but serve as bracketing cases for the studies of the effects of different initial conditions. The inset shows an illustration of the functional form of the distributions versus initial energy.

of initial energy distributions are also explored, which bracket the maxwellian case and the experimental data. The first one is a “uniform” distribution, which generates initial energies with uniform probabilities in the range $0 - 0.75\,\mathrm{K}$; this allows for more low-energy particles compared to the maxwellian case. The second is a “linear” distribution, where high-energy particles are more probable than in the nominal case.

Simulation results obtained with these different initial anti-atom energy distributions are shown in Fig. 4.6. It is clear from the plot that different distributions produce different simulated sensitivities, and a lack of a more precise knowledge of the real distribution causes an important error of type A. It can also produce a type B error if the initial energies are assumed to change from one year to the next. The data shown in Fig. 4.5 provides evidence against this, but it is an effect that cannot be completely ruled out.

## Location errors

In sec. 1.2, it was mentioned that the center of the mixing trap coincided with the center of the magnetic trap to within $0.5\,\mathrm{mm}$; the measurement, in fact, placed the center of the magnets at $z = -0.5 \pm 0.5\mathrm{mm}$. This result was based on observations of heating of an electron plasma using microwaves [17]. In that method [43], pulses of microwaves of different

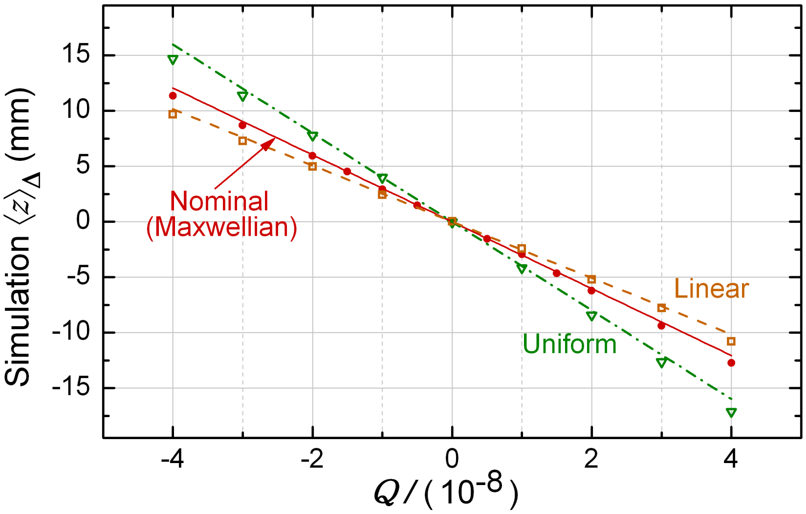

Figure 4.6: Simulated $\langle z \rangle_\Delta$ for different antihydrogen initial energy distributions and several values of $Q$. The same color codes of Fig. 4.5 are used: Orange squares were obtained with a "linear" distribution, blue triangles with a "uniform", and red circles using the "nominal" maxwellian. The lines are least-squares linear fits that show the variation of sensitivity caused by the change in initial energy distribution. These results include detector effects and appropriate cuts.

(known) frequencies are sent along the axis of the trap and made to interact with an electron plasma that has previously been loaded. By monitoring the temperature of the plasma, the cyclotron frequency of the electrons is found as the frequency of microwaves which produces maximum heating. Since the cyclotron frequency is directly related to the local magnetic field, maps of cyclotron frequencies obtained with electron plasmas prepared in different axial locations allow to determine the magnetic field minimum. That minimum is the axial center of the magnetic trap.

As the magnets were fixed on the assembly of the trap, this displacement $\epsilon_z$ is time invariant. It only causes a type D error.

The detector, on the other hand, had some freedom to move with respect to the mixing trap. The displacement, however, was constrained by measurements using annihilations of antiprotons on background gas during lifetime measurement runs (see sec. 2.3). The technique [22, ch.5] consisted on loading a small (compared to the resolution of the detector, Fig. 2.7) antiproton plasma in a known location of the mixing trap. Measurements of annihilations during the waiting would then indicate the location of the antiprotons in *detector coordinates*. By comparing the mean annihilation location to the known location of the antiprotons in the trap, a number could be obtained for the location of the detector with respect to the electrodes.

The original measurement, using a plasma centered at $z = 0$, placed the detector center at $z = 23.95 \pm 0.24\,\mathrm{mm}$. This number was used to transform the location of quantities in detector coordinates into trap coordinates (sec. 1.2), such as the experimental data and efficiency curves (Fig. 2.6), and is a source of a small type D error of $\pm 0.24\,\mathrm{mm}$. The way the electrode biases were set made the measurement insensitive to possible inaccuracies in the voltages applied.

Measurements in later years based on the same technique were used to identify possible displacements in time. In those cases, however, a different set of (smaller) electrode bias potentials was used that could introduce errors. By correcting for possible displacements of the antiproton plasma due to inaccuracies in the biases (estimated to be $\approx \pm 250\,\mathrm{mV}$ for the $\approx \pm 10\,\mathrm{V}$ biases used), a maximum $\epsilon_z$ of $\pm 0.34\,\mathrm{mm}$ was calculated, leading to a small type B error.

## Detector errors

The efficiency curve used to add detector effects to the simulations (sec. 2.3) was obtained with Monte Carlo simulations using GEANT3 [33]. As discussed earlier, the slight asymmetry in $z$ of the efficiency creates a slight bias towards the positron side (Fig. 2.6), causing a small type D error.

A type A error is associated to the uncertainty in the knowledge of the true efficiency curve. In order to quantify the effect, another plausible (early) curve (see Fig. 4.7) was considered and applied to the simulated data, in the same way described in sec. 3.5. A linear fit of the resulting $\langle z \rangle_\Delta$ versus $Q$ leads to a slightly different sensitivity, $s = (-3.40 \pm 0.03)\,(10^{-9}\,\mathrm{mm}^{-1})$, which gives a normalized variation $\epsilon_s = (3.40/3.31) - 1 \approx 0.02$. It is somewhat surprising that such a small effect would be produced by a seemingly big difference in efficiency curves; this is a fact that demonstrates the robustness of the method against constant offsets.

This error shows the effect that using a *different* efficiency curve would have on the calculation of $Q$. However, errors could also occur by incorrectly assuming that the efficiency curve has a certain functional form, while in reality it has a different one.

In order to analyze this, "predictions" are made using the nominal efficiency curve (Fig. 4.7) and the results are compared to data generated in an apparatus that is assumed to obey a different curve, following a procedure similar to the one described in the simulations benchmark. Specifically, a sensitivity is obtained using the nominal efficiency and used to calculate a "Predicted $Q$", and the results are compared to "Actual $Q$" data generated with the "early version" curve (see Fig. 4.7).

The top plot in Fig. 4.8 shows the Predicted $Q$ against Actual $Q$. The middle plot shows the error (Predicted $Q -$ Actual $Q$) and the bottom plot shows the error normalized by the statistical error of the measurement of $Q$. Considering $Q$ only in the range $\pm 1 \times 10^{-8}$, as done for the simulations benchmark, leads to a normalized error in $Q$ in the range $[-4.9\%, 5.5\%]$. A very similar calculation employed for the calculation of the systematic error in table 4.2 yields a normalized $Q$ error of $\pm 3.6\%$ (note that the numbers in the table are not normalized).

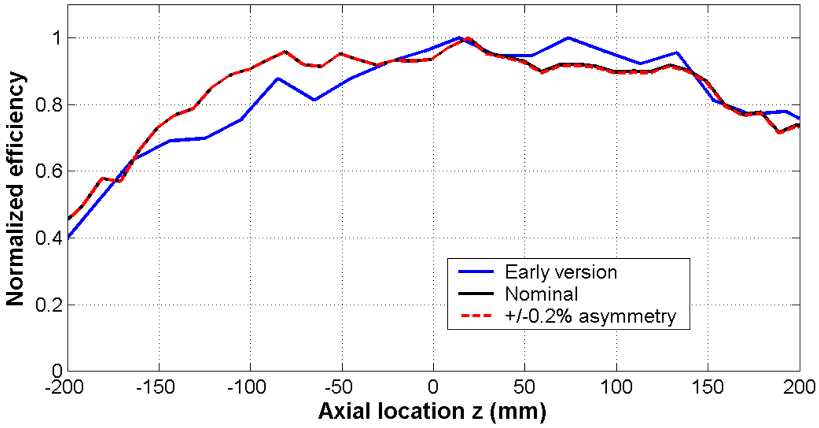

Figure 4.7: Normalized detector efficiency curves used in studies of detector-related systematic effects. All curves are linear interpolations of Monte Carlo simulated data. An early version (blue) was used as a plausible alternative to the nominal (black, the same as in Fig. 2.6) curve. The red-dashed curve results from adding a ±0.2% asymmetry to the nominal curve on each side of the detector (see text).

Even if the range were extended to $\pm 4 \times 10^{-8}$, the error would be less than 1/3 of the statistical error and less than the dominant systematic error in table 4.2.

A similar analysis can be applied to study the effect of a different $z$ resolution of the detector. In that case, the nominal simulations are used to calculate values of Predicted $Q$ and an altered smearing function is used to calculate values of Actual $Q$. Figure 4.9 shows the results for a smearing function with a width that is a factor of 4 larger (Fig. 2.7). Such an alteration has very significant effects on the distribution of the annihilations; however, the normalized error range in $Q$ is still small: $[-8.3\%, 8.2\%]$.

A different concern that deserved close attention were possible changes over time in the detector efficiency which could have introduced different biases in the calculations of $\langle z \rangle_R$ and $\langle z \rangle_L$, thus altering $\langle z \rangle_\Delta$. Dedicated studies, using cosmic ray particles, were performed and gave results consistent with no change in efficiency over time [44]. In order to reach that conclusion, the “occupancies” of each one of the 60 modules that make the detector were analyzed for several cosmic-analysis runs in 2010 and 2011 (the “occupancies” are the number of hits that form a particle track, normalized by the number of cosmic rays detected). The average occupancies for the modules on the AD side of the apparatus and those on the positron side were calculated for each one of the two years of interest, and then compared. Changes in the averages between 2010 and 2011 of $0.2 \pm 0.2\,\%$, on the AD side, and $-0.2 \pm 0.2\,\%$, on the positron side, were observed.

A time-drift systematic error of the detector system was calculated using the pessimistic assumption that the efficiency changed by the numbers mentioned above between the two years. An efficiency curve was created for the 2011 data by taking the “nominal” curve

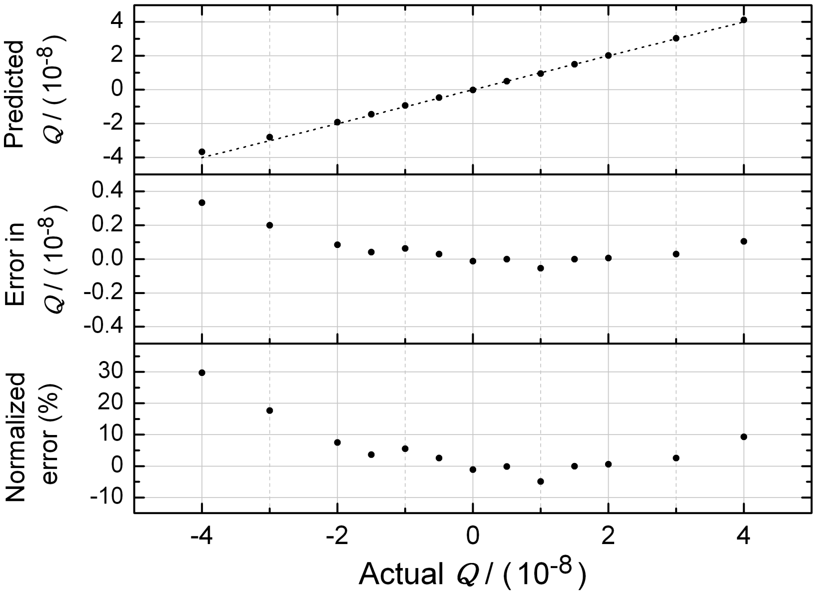

Figure 4.8: Predicted $Q$ versus Actual $Q$ when an efficiency curve different from the nominal is assumed to be the true one obeyed by the experiment (top plot). In this case, Actual Q data is generated using the "early version" curve in Fig. 4.7. The dashed line is a slope one line (not a fit of the data); departures from it induce the errors shown in the middle plot, which is calculated as Predicted $Q -$ Actual $Q$. The bottom plot shows the error normalized to the measured statistical error in $Q$.

(Fig. 4.7), uniformly increasing the efficiency by 0.2% in all $z$ on the AD side of the detector (note that this is not exactly the same as all $z < 0$ due to the offset between the trap and detector zeros), and then decreasing the efficiency by the same amount in all $z$ on the positron side. The calculation of $\langle z \rangle_\Delta$ for each $Q$ then proceeded using the nominal curve for 2010 and the modified one for 2011. A linear fit of the results shows a small error of type B.

## Antiproton and cosmic contamination

As mentioned in sec. 4.1, antiproton contamination is reduced by the use of elliptical cuts. 95% of any antiprotons surviving by the end of the experiments are expected to annihilate within the aforementioned elliptical regions, so the decision to remove data falling in those areas is well motivated. This comes at a cost, though, since the removal of legitimate events affects the sensitivity adversely. The simulations predict that, for the total of 386 in the final list of events, 7.7 antihydrogen atoms are expected to be cut out.

In fact, 9 experimental events fall in the elliptical regions. This is very close to the number of anti-atoms expected from the simulations, and provides evidence against any

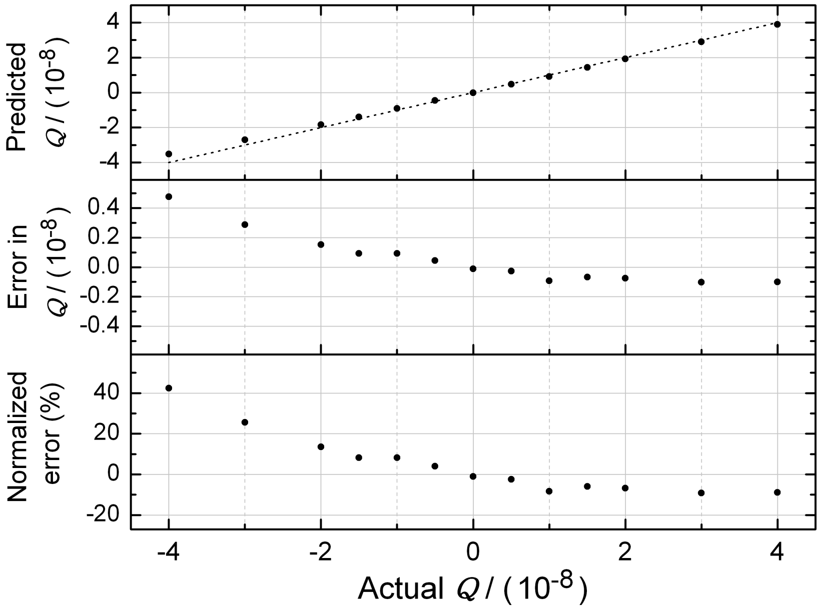

Figure 4.9: Predicted $Q$ versus Actual $Q$ when the detector is assumed to have a poorer resolution (4 times the width of Fig. 2.7) than the one used in the nominal results (top plot). Departures from the slope-one dashed line indicate errors, which are shown in detail in the middle plot (which is calculated as Predicted $Q -$ Actual $Q$). The bottom plot shows the error normalized to the measured statistical error in $Q$.

contamination of antiprotons. However, in the very pessimistic event that all 9 events are indeed antiprotons, 5% of that number ($9 \times 0.05 = 0.45$) should escape the elliptical cuts and produce an error. Simulations have shown [32] that the $z$-averaged location of antiprotons outside the excluded regions is approximately $z = \pm 110\,\text{mm}$. This result would alter the experimental average location of annihilations used in the charge measurement by approximately $0.45 \times 110\,\text{mm}/386 = 0.13\,\text{mm}$.

This is not strictly a type B error, since the antiproton count could have occurred at any time during the two years. Nevertheless, a pessimistic estimate of the effect can be made by assuming that it only affected the data in 2011, thus producing an offset in $\langle z \rangle_\Delta$ of approximately the same amount.

Cosmic rays passing through the apparatus are another source of error. In sec. 4.1 it was estimated that $< 2$ cosmics are expected to have been misclassified as annihilations. The cosmics are uniformly distributed in $z$, but as the detector did not have perfect efficiency (sec. 2.3), their detection followed approximately the distribution of the simulated efficiency curve. An estimate of the effect of the contamination can then be calculated by using the width of the efficiency curve to give a pessimistic location where cosmics were likely to be detected, and seeing the effect that this would have on the calculation of the average locations of anti-atom annihilations.

As with antiprotons, the error produced by the cosmics is not strictly of type B. However, it can be modeled as such by assuming the pessimistic scenario that cosmics only affected the 2011 data.

## Effects of cuts

Studying the effects of a "cut" is different than most of the studies of systematic effects because in this case something *known* is done to the data.

Cuts affect three parameters in the analysis:

- The observed $\langle z \rangle_\Delta$.
- The observed uncertainty of $\langle z \rangle_\Delta$, since cuts may affect the standard deviation of the observations.
- The sensitivity $s$.

Applying a cut has effects in all three parameters, so it is important to study all effects simultaneously in order to see what the effect of a cut is in the observed value of $Q$. Generally speaking, cuts decrease the value of $\langle z \rangle_\Delta$ for a given $Q$ and increase the sensitivity $s = dQ/d\langle z \rangle_\Delta$. Thus, $Q = s\,\langle z \rangle_\Delta$ remains constant, which leads to the observation that placing a cut has no effect on the *predictions* of the value of $Q$.

This is a straightforward conclusion that is easy to see by assuming that the relationship between $Q$ and $\langle z \rangle_\Delta$ is linear in the range of interest (i.e. $s$ is constant). However, the linearity is not a necessary requirement: A higher order function could be used to relate $Q$ and $\langle z \rangle_\Delta$. Nonetheless, for all combinations of cuts and reasonable $Q$, the relation is very nearly linear, as shown in Fig. 4.10; in that plot, results for the nominal simulations (nominal efficiency curve, $|z| \leq 136\,\mathrm{mm}$ and elliptical cuts), nominal with no elliptical cuts, and results assuming a perfect detector with no cuts, show that no significant deviation from linearity occurs for $|Q| \leq 4 \times 10^{-8}$.

As mentioned in sec. 4.2, each one of the individual points used for the fits to compute the sensitivities are the result of averaging around 400 000 points. Each one of those points is an unbiased estimator of the $\langle z \rangle_\Delta$ that would be obtained with experimental data for a particular value of $Q$. Fitting the points with a generic function thus leads to an unbiased estimator of $Q$ as a function of $\langle z \rangle_\Delta$, something that is particularly simple when the function used is linear, as it can be well approximated in this case.

Figure 4.10 illustrates the small change in sensitivity made by the elliptical cuts: $-3.31 \times 10^{-9}\,\mathrm{mm}^{-1}$ compared to $-2.85 \times 10^{-9}\,\mathrm{mm}^{-1}$. Even assuming a perfect detector with no cuts does not lead to big changes; in that case, the sensitivity is $-2.13 \times 10^{-9}\,\mathrm{mm}^{-1}$, only a factor of 1.34 lower.

The reason why the sensitivity does not change much can be explained by looking at Fig. 4.11. The top plot (green) shows the simulated distribution of antihydrogen annihilations

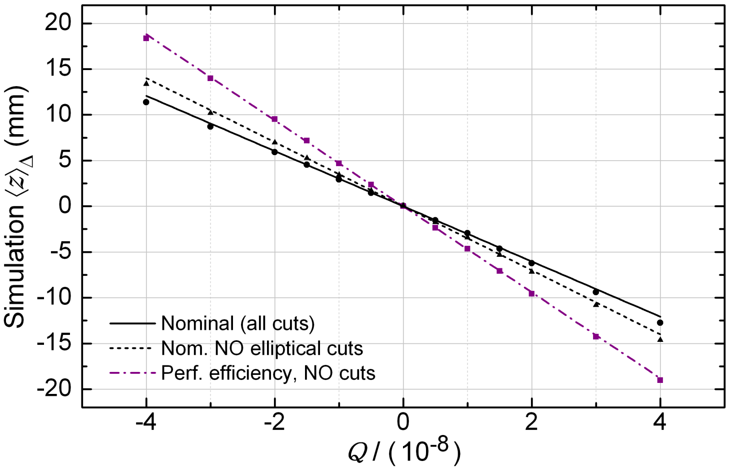

Figure 4.10: Simulated $\langle z\rangle_\Delta$ showing the effects of applying different cuts. The solid black line is the linear fit of the points (circles) obtained with the nominal detector effects and cuts (including elliptical cuts). The effect of not applying elliptical cuts can be seen in the dashed black line and triangles, where nominal simulations and detector effects have been used. The purple dash-dotted line and squares are results obtained assuming a perfect detector efficiency (i.e. an efficiency of value one independent of $z$) and without applying any cuts in $z$. In all cases, the linear fit gives a very good description of the simulated values of $\langle z\rangle_\Delta$.

for Q=0, no cuts and no detector effects. The dashed lines show the location of the $|z| > 136$ mm exclusion range if the appropriate cut were implemented. A careful count shows that 3.8% of the total of annihilations fall in that range, in good agreement with the experimental value of 4.7% (p= 0.34). Even if $Q \neq 0$, very few particles annihilate outside ±136 mm, as the middle plot shows (blue). The bottom plot (red) shows that the effect of a nonzero $Q$ is different from a simple shift of the $Q = 0$ distribution; if that were the case, the cuts at $|z| = \pm 136$ mm would certainly have larger effects.

Figure 4.11 also shows that the experiment itself effectively imposes a cut at $\approx \pm 136$ mm. The reason for this is that the maximum of the mirror fields is very close to those locations. The mirror fields add linearly to the background 1 T field, but the octupole adds in quadrature (sec. 2.2). Therefore, even though the decay rates of the mirrors and octupole are very similar (Fig. 2.5), the radial "potential wall" decays much faster at the time of the magnetic trap shutdown and most particles escape radially; only the aforementioned $\approx 4\%$ escape over the axial wall.

In summary, there are very good reasons for placing the cuts at ±136mm:

- Most annihilations occur inside $|z| \leq 136$ mm, so very few events are removed by placing the cuts.

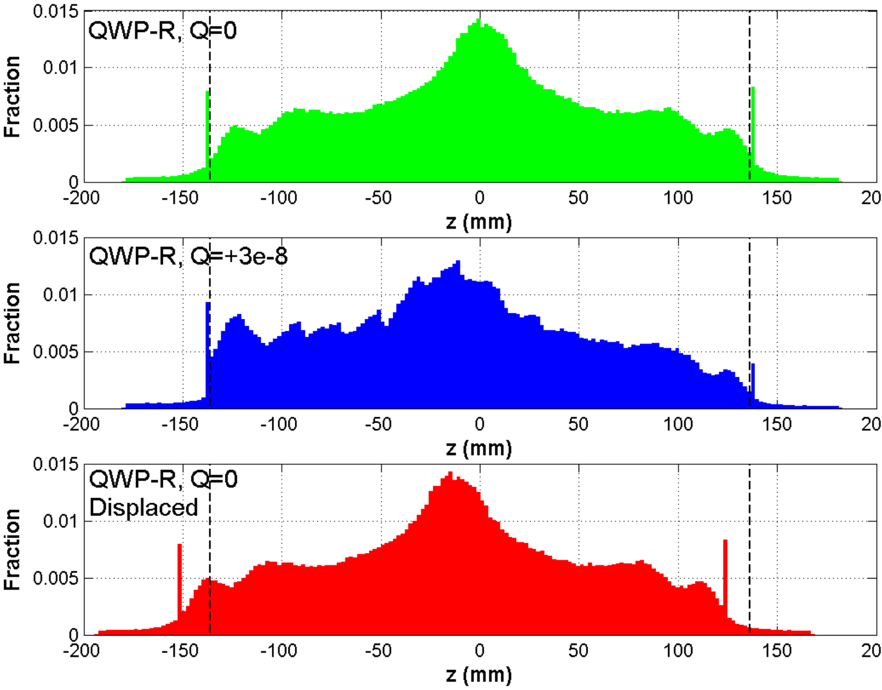

Figure 4.11: Comparison of different simulated annihilation distributions, with no detector effects and no cuts in $z$. The top (green) plot is the normalized histogram of simulated annihilation locations for $Q = 0$ under Bias-Right conditions. The middle plot corresponds to Bias-Right, $Q = 3 \times 10^{-8}$; notice the fact that most annihilations remain in the region bounded by the two vertical dotted lines (placed at $z = \pm 136\,\text{mm}$). This is in contrast to the $Q = 0$ distribution displaced to have the same mean as the $Q = 3 \times 10^{-8}$ (bottom red plot). The large number of counts near $z = \pm 136\,\text{mm}$ for the top and middle plots corresponds to annihilations at the radial step of the electrodes.

- As mentioned in sec. 4.1, the trap wall has a change in radius (a "step") just past ±136 mm. According to the simulations, about 25% of the anti-atoms that manage to escape through the ends annihilate on the step.

- By cutting out the larger $z$ data, big changes in the detector efficiency can be avoided (Fig. 2.6), as well as changes in the detector reconstruction resolution.

The antiproton-supressing elliptical cuts, as mentioned before, are more of a tradeoff. As can be seen in Fig. 4.12, the sensitivity decreases slightly when the cuts are removed while, in contrast, the uncertainty of $\langle z \rangle_\Delta$ increases. The net result is that the error in $Q$ increases by 12.5% with the cuts. Based on the discussion above, the predicted $Q$ is an unbiased estimator of the actual $Q$, so the errors of the assumed efficiency curve used in the plot are unimportant.

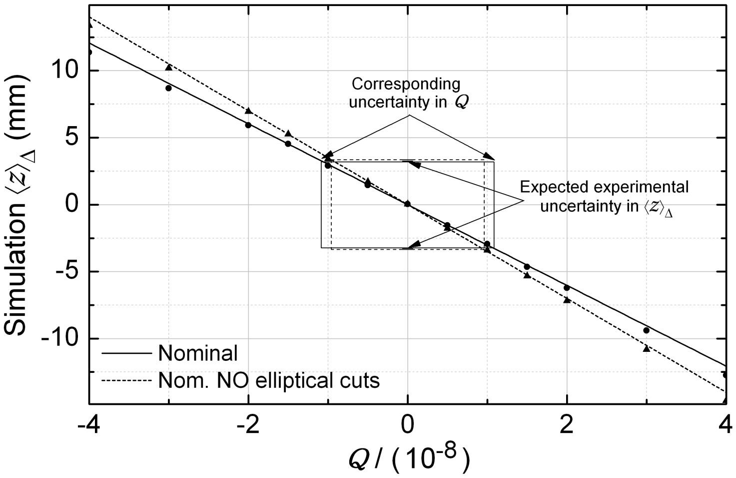

Figure 4.12: Sensitivity and calculated error in $Q$ for the nominal simulations (circles, solid line) compared to simulations with no elliptical cuts (triangles, dashed line). The addition of the cuts increases the sensitivity but decreases the estimated experimental uncertainty in $\langle z \rangle_\Delta$ (vertical width of the box). The net change in the uncertainty in $Q$ (horizontal width in the box) is a combination of both effects, and is therefore less pronounced than one might anticipate.

# Chapter 5

# Stochastic heating of antihydrogen

## 5.1 Introduction

The fractional charge bound found in sec. 4.2 is based mainly on the effects of static bias fields. However, as will be shown in this chapter, tighter bounds can be found by considering the particle dynamics as the electric fields in the trap are manipulated.

Antihydrogen trapping sequences included a series of "clearings" (see sec. 2.4), where the electric field underwent four cycles of oscillations between fields that resembled Bias-Right and Bias-Left; the first two cycles were done at lower voltages, approximately half of those used in the final clearing cycles. As the axial velocity of anti-atoms in the trap was expected to be $< (1/3)\,130\,\mathrm{m/s} = 43\,\mathrm{m/s}$ (see sec. 3.3), their orbits of $\sim 200\,\mathrm{mm}$ had oscillation times $> 4\,\mathrm{ms}$. Therefore, these eight oscillations, which were ramped in intervals of 2 ms, plus the final application of the bias field, which was ramped in 7.5 ms, were non-adiabatic, that is, the fields were applied on a time scale that was comparable to or short compared to the characteristic orbit oscillation times of the trapped anti-atoms.

After each change, the field was held constant for $\approx 10\,\mathrm{ms}$, a time comparable to, or longer than, the anti-atom orbit oscillation times. Thus, the kinetic energy of the center-of-mass of anti-atoms with a charge $Q$ changed by an amount $\Delta E_k \approx Qe\langle\Phi\rangle_\Delta$ as a consequence of each field change, where $\langle\Phi\rangle_\Delta$ is the characteristic electrical potential change experienced by the anti-atoms along their orbits. This energy change could be either positive or negative.

If the energy kicks were independent, this process would resemble a "random walk" in energy, which would lead to a form of forced "stochastic heating". The total energy gain would then scale approximately with the square root of the number of field changes $N$ (or "kicks"), so that $\Delta E_{net} \approx |Q|e\langle\Phi\rangle_\Delta\sqrt{N}$. Therefore, for a charged anti-atom in a trap with depth $U_T$, sufficiently large $N$ would force it to evaporate out of the trap. Likewise, for fixed $N$, a particle with fractional charge $Q$ would evaporate if

$$|Q| > \frac{U_T}{e\langle\Phi\rangle_\Delta}\sqrt{\frac{1}{N}} \tag{5.1}$$

In ALPHA1, $U_T = 0.54\,\mathrm{K}$ (see sec. 2.2). With an estimated $\langle\Phi\rangle_\Delta = 50\,\mathrm{eV}$ from Fig. 2.8, eqn. (5.1) predicts that anti-atoms with $|Q| > 3 \times 10^{-7}$ evaporate out of the trap. A more accurate result, without any estimated quantities, can be found by simulations. Figure 3.1 shows particles with $Q = 2\times 10^{-7}$ during the final stages of a trapping sequence. The heating effects of the field oscillations are clearly seen, and a careful count shows that 50% or more of the anti-atoms evaporate out of the trap before the magnet shutdown, in agreement with the estimation based on eqn. (5.1).

## 5.2 Method and model

The stochastic heating bound on $Q$ calculated in sec. 5.1 is roughly ten times less strict than the electrostatic deflection bound calculated in sec. 4.2. However, forced stochastic heating has several advantages which may lead to a much tighter bound. First, instead of looking for a small average deflection, which requires hundreds of anti-atoms to measure accurately, stochastic heating relies on the simpler observation that anti-atoms survive (sec. 5.4). Second, in experiments deliberately designed to employ stochastic heating, much larger fields can be applied than those used in experiments to date. For example, if the potential oscillated between the black trace in Fig. 5.1a and its inverse, the average change in the potential would be approximately $\langle\Phi\rangle_\Delta = 250\,\mathrm{V}$, as determined by simulations. Third, and most important, many more heating cycles ("kicks") can be employed by rapidly switching between a given potential configuration and its inverse.

Since, as mentioned before (sec. 3.1), the dynamics of antihydrogen atoms in the trap are very complex, numerical simulations are required to calculate the effects of stochastic heating. The basic equation of motion is again eqn. (3.3), and a code in C++ very similar to the one described in sec. 3.3 was implemented to perform the integration of anti-atom trajectories with a presumed fractional charge $Q$ from similar initial conditions [32, 36].

The manipulations in this case are somewhat simpler. The magnetic trap does not need to be turned off since there is no need to study the locations of annihilations during the trap shutdown. Therefore, the magnetic field $\vec{B}$ can be kept constant in time. Furthermore, the electric field only performs the transitions indicated in Fig. 5.1, and all electrodes can be taken to have "fast" responses (sec. 2.1), as they would conceivably be driven by a separate device that is not narrowly band limited like the ±75 V amplifiers. Thus, fewer potential interpolation coefficients are needed, and once loaded into memory, no transitions need to happen between different sets.

The only extra complexity comes from the generation of stochastic switching times, which are needed in the studies of later sections (see sec. 5.3). These are calculated at runtime using a uniform distribution with mean $\bar{t}$ and standard deviation $t_\sigma$, which are set as parameters during the initial configuration of the program. Every time a voltage flip happens, a new random time is calculated and set such that a new transition happens after the freshly-calculated amount of time.

The code implements the following algorithm:

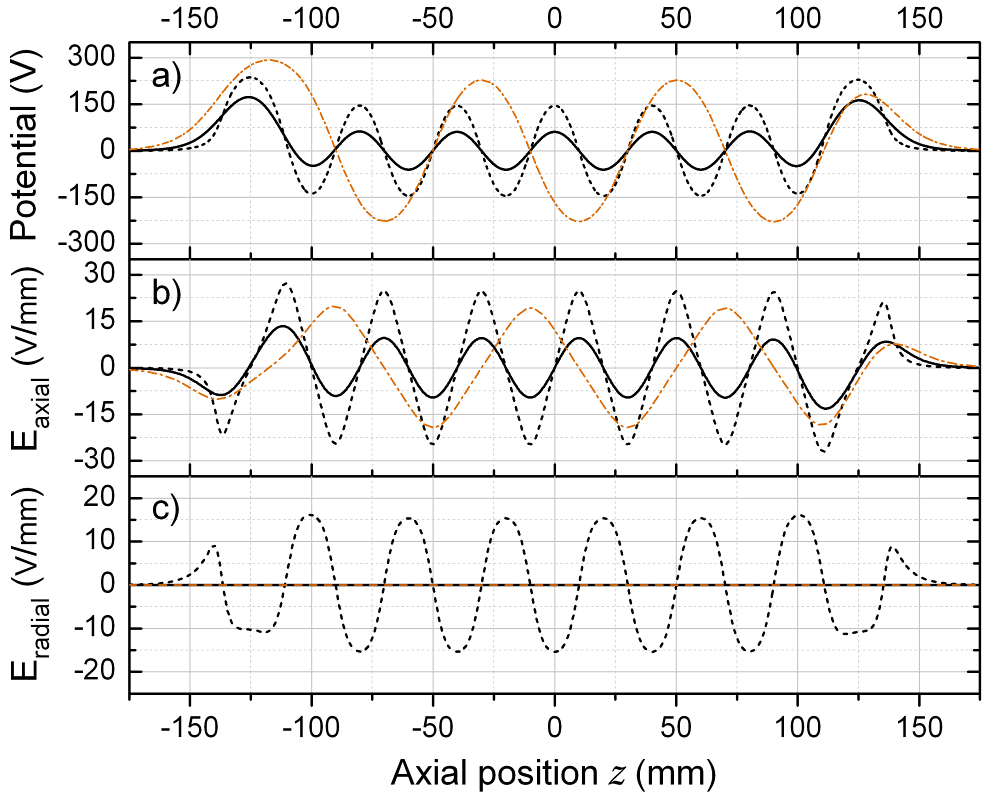

Figure 5.1: Values of the field on-axis (solid line) and at 60% the maximum trap radius (dashed line), for applied biases alternating between ±350 V on consecutive electrodes of the mixing region (350 V amplitude); all other electrodes are kept at 0 V. The orange dash-dotted line is the on-axis field when biases alternate in sets of two, i.e. the same bias is applied in two contiguous electrodes, then inverted for the following two, then flipped back for the next two, etcetera. a) Electrostatic potential. b) Axial component of the electric field. c) Radial component of the electric field. For stochastic heating, the voltages flip at random times between those shown and their inverse (see text). The amplitude of 350 V is a realistic value that can be achieved with circuits using current technologies of power electronics.

1. Configure constants and parameters. The fractional charge $Q$, the time step $t_{step}$, the total simulation time $T$, and the stochastic heating amplitude, mean switching time and standard deviation, for example, are set in this step.
2. Load the electrostatic potential interpolation coefficients from the corresponding file.
3. Generate random initial conditions of position and velocity for one anti-atom, using the distributions discussed in sec. 3.2. Choose the start time of the simulation to be $t = -1.0\,\mathrm{s}$, which gives a 1 s randomization time before the start of the potential manipulations. These manipulations begin at $t = 0$ with the first voltage flip.
4. Go forward one time step, using the symplectic integrator and the value of the current (at time $t$) electric field, calculated as described above.
5. Update the simulation time to $t = t + t_{step}$.
6. Check whether the anti-atom is still within the boundaries of the trap, or that the total simulation time $T$ has not been reached. If true, go back to step (4). If false, print the simulation time $t$, the $z$ of the particle, its initial and final energies, and continue.
7. Check how many anti-atoms have been simulated. If fewer than *numtraj*, go to step (3). Otherwise, print total execution time and finish.

In reality, the only information needed from each anti-atom is the escape time (if the anti-atom escapes at all), which is used to calculate the probability that an antihydrogen atom remain in the trap after being heated for some amount of time. The extra information printed in step (6) is used to gain insight into the features of the heating.

Initially, the same time step $t_{step}$ of $3.5\,\mu\mathrm{s}$ used for the simulations of sec. 3.3 was employed. However, as it was of interest to see the effects of very long heating times (of $\sim 1000\,\mathrm{s}$ or more), wider time steps were considered. It was seen that the choice $t_{step} = 35\,\mu\mathrm{s}$ gave results consistent with those of the shorter $t_{step}$, at 10 times the speed. For this reason, all stochastic heating simulations presented in what follows use $t_{step} = 35\,\mu\mathrm{s}$, unless stated otherwise.

Figure 5.2 shows typical simulation results, obtained in this case with $Q = 5 \times 10^{-10}$ and a heating signal with amplitude 350 V, mean switching time $\bar{t} = 0.3\,\mathrm{ms}$, standard deviation $t_\sigma = 60\,\mu\mathrm{s}$ and total heating time $T = 100\,\mathrm{s}$. The top plot shows the axial locations where anti-atoms escape. There is a clear tendency for particles to leave the trap around $z = \pm 130\,\mathrm{mm}$, which suggests that anti-atoms escape preferentially through the "holes" created by the octupole field at those locations in the magnetic trap [4] before they are able to reach the electrode step (change in electrode radius, see sec. 2.1). The middle plot shows the initial (blue) and final (red) energies of escaping particles, and the intuitive fact that particles with lower initial energies take longer to escape. Final energies are shown not to all agree exactly in value, but have a spread (see sec. 5.3).

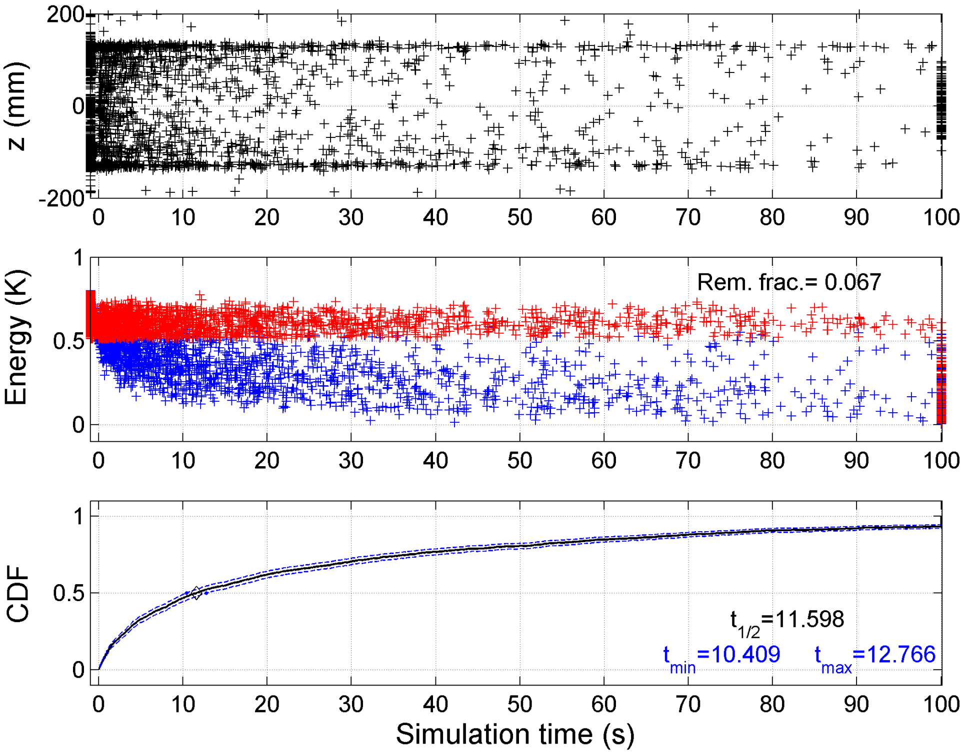

Figure 5.2: Stochastic heating simulation results for $Q = 5 \times 10^{-10}$, total heating time $T = 100\,\mathrm{s}$ and a heating signal with amplitude 350 V, mean switching time $\bar{t} = 0.3\,\mathrm{ms}$, standard deviation $t_\sigma = 60\,\mu\mathrm{s}$. The axial location $z$ of the annihilations (top plot) shows that anti-atoms tend to escape at $z \approx \pm 130\,\mathrm{mm}$; particles shown at $t = T$ correspond to anti-atoms that remain trapped after the end of heating. The middle plot shows the initial (blue) and final (red) energies, and the bottom plot shows the cumulative distribution function of the escaping particles (see text for details).

The bottom plot in Fig. 5.2 shows the empirical cumulative distribution function (CDF) of the escaping particles (black trace), which corresponds to the number of anti-atoms that escape in the interval $[0, t]$ divided by the total number of simulated anti-atoms that survive the randomization time. This curve is an estimator; the blue-dashed curves, calculated using Greenwood's formula [45, 46], establish the 95% confidence bounds for the true CDF. Using these results, the number '$t_{1/2}$', which will be widely used in sec. 5.3, is defined as the time by which exactly half of the particles escape (the median of $t$); it has bounds $t_{min}$ and $t_{max}$, calculated as the times where the confidence bound curves reach a value of 0.5. These numbers allow to estimate the error in $t_{1/2}$ as $t_{error} = \max[(t_{max} - t_{1/2}), (t_{1/2} - t_{min})]$; the interval $(t_{1/2} - t_{error}, t_{1/2} + t_{error})$ then contains the true median escape time with at least 95% confidence.

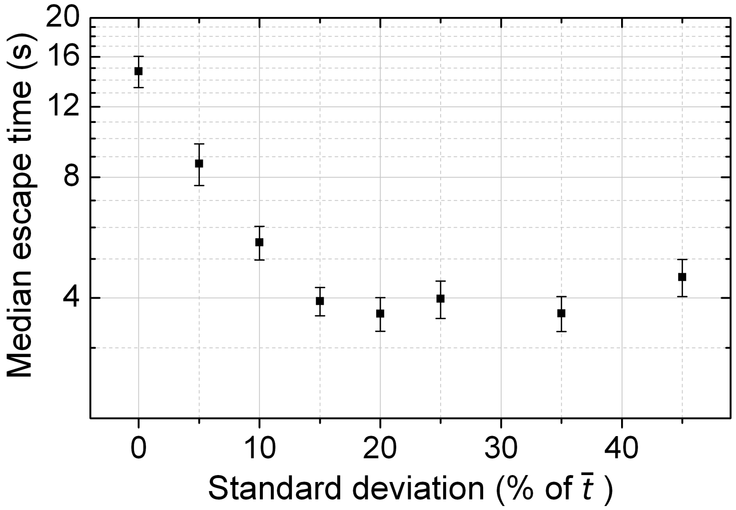

Figure 5.3: Median escape time for particles with $Q = 10^{-9}$ and heating of amplitude 350 V, mean switching time $\bar{t} = 0.3$ ms and varying standard deviation. The standard deviation is given as a percentage of $\bar{t}$, which means that the random number generator (uniform distribution) used a standard deviation with value equivalent to $\bar{t}$ times the number stated in the plot.

Finally, not all the particles escape by $t = T$. The remaining fraction, stated in the middle plot, is the ratio of anti-atoms that remain trapped after being subjected to heating, to the total number of simulations that survive past the initial randomization time. The fact that not all particles escape by time $T$ does not affect the calculation of $t_{1/2}$ (this is in general true, provided $T > t_{1/2}$), but does explain why in this example the CDF never reaches the value '1' before the end of the simulation.

## 5.3 Simulation results

The chaotic nature of antihydrogen orbits in the trap [32] largely provides the randomness needed for stochastic heating. However, extra randomization can be added by changing the time interval of the switching such that the electrostatic potential flips at random times with a fixed mean. A uniform distribution is used for the work presented here.

Figure 5.3 shows the effect of changing the standard deviation of the switching ($t_\sigma$) as a percentage of the mean switching time $\bar{t}$. The "median time of escape" $t_{1/2}$ (defined in sec. 5.2) of the particles is a measure of how effective the heating is; if $t_{1/2}$ is short, particles are heated faster to an energy high enough to escape from the trap. The plot shows that heating occurs even when the forcing signal is periodic and does not have a random component; that is the case $t_\sigma = 0$. However, heating is more efficient when some randomness is added, reaching an optimum at $t_\sigma = 0.2\,\bar{t}$ and leveling out for larger values of $t_\sigma$. This trend seems to degrade for $t_\sigma > 0.4\,\bar{t}$, at values where the random component starts to approach the size of $\bar{t}$. Together, these observations show that it is useful to incorporate some randomness in the heating signal, and that the choice $t_\sigma = 0.2\,\bar{t}$ is well suited for use in the simulations.

The mean switching time $\bar{t}$ is expected to have an optimal value. When switching is too fast, anti-atoms cannot propagate far enough to undergo an extra kick; when it is too slow, few heating cycles can be accomplished in a fixed amount of time. An estimate of this optimal switching time can be made by recalling that the axial speed of anti-atoms in the trap is $< 43\,\mathrm{m/s}$ (see sec. 5.1); then it takes $\sim 0.5\,\mathrm{ms}$ for an antihydrogen atom to move out from the area of influence of the "current" electrode (a distance of $\sim 2\,\mathrm{cm}$) and have a chance to receive a kick that does not undo the effect of the previous one. Therefore, switching times of $\sim 0.5\,\mathrm{ms}$ are expected to give the best results. Figure 5.4 shows the effect of changing the mean switching time $\bar{t}$ on heating when electrode biases of $\pm 350\,\mathrm{V}$ (black trace in Fig. 5.1a) are used, and $t_\sigma = 0.2\,\bar{t}$. The plot shows that the heating has the expected behavior with changes in $\bar{t}$, reaching an optimal value at $\bar{t} = 300\,\mu\mathrm{s}$, reasonably close to the estimate given above.

This behavior is also seen in the results obtained with simulations were biases do not alternate in contiguous electrodes, but in groups of two (orange trace in Fig. 5.1a). In that case, the optimal heating happens when $\bar{t} = 600\,\mu\mathrm{s}$, consistent with the observation that the anti-atoms must travel twice the distance to leave an area where the potential does not alternate, compared to the original case. It is interesting to note that the optimal median escape time is the same, to within statistical noise, as in the original case. This may be the result of higher electric fields compensating for the effect of fewer average "kicks".

The optimal mean switching time also changes with the trap depth and the temperature $\tau$ of the anti-atoms, as the blue triangles in Fig. 5.4 show. As lower temperatures imply lower initial velocities, it is not strange to see that slower switching times are more effective for heating the particles.

Having chosen optimal values for $\bar{t}$ and $t_\sigma$ ($300\,\mu\mathrm{s}$ and $60\,\mu\mathrm{s}$, respectiely), simulations were run for stochastic heating signals of amplitudes 350 V, 100 V and 35 V. The results are shown in Fig. 5.5. The most important observation is that fractional charge sensitivities as low as $\sim 5 \times 10^{-11}$, for heating times $\leq 1000\,\mathrm{s}$, can be achieved without modifications to the antihydrogen trapping parameters used in ALPHA1. This is a realistic time scale based on experimental measurements [7].

Linear fits of the simulated values of $t_{1/2}$ vs. $Q$ in the log-log plot (Fig. 5.5) show a simulated heating scaling that is very close in value to that expected from the simple model in eqn. 5.1, where $N \sim t_{1/2}/\bar{t}$. For that case, $\log(t_{1/2}/\bar{t})$ = -2 $\log(|Q|)$ + 2 $\log(U_T/e\langle\Phi\rangle_\Delta) \Rightarrow$ $\log(t_{1/2})$ = -2 $\log(|Q|)$ + 2 $\log(U_T\sqrt{\bar{t}}/e\langle\Phi\rangle_\Delta)$, so the expected slope of the lines in Fig. 5.5 is '-2'. Actually, the slopes in the simulations are $-1.81 \pm 0.018$, $-1.81 \pm 0.016$ and $-1.82 \pm 0.005$ for 350 V, 100 V and 35 V respectively (the error here stands for one standard fit error); a value which is slightly different but still close enough to support the idea that the underlying

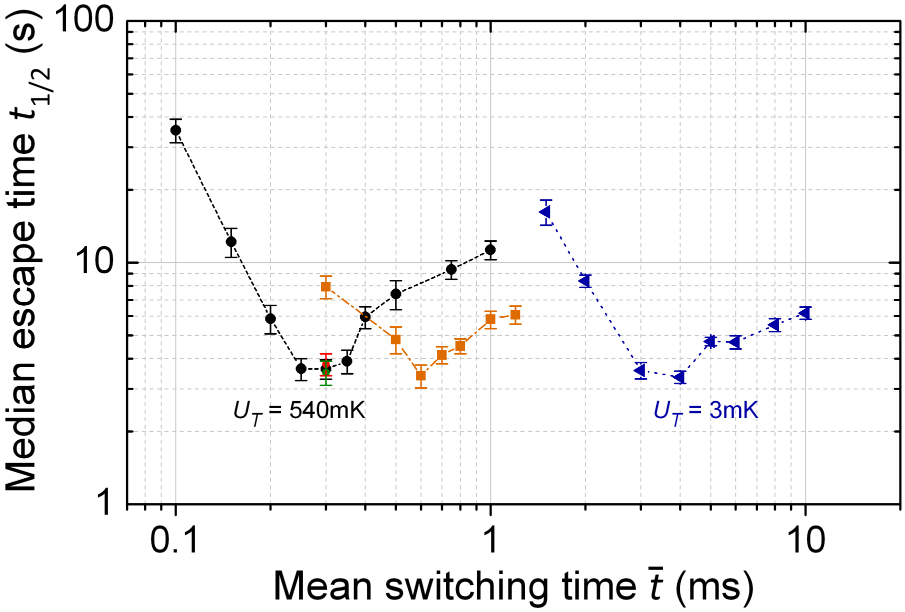

Figure 5.4: Median escape time for particles when heated with a stochastic drive of amplitude 350 V (using biases of ±350 V at the electrodes) and different mean switching times $\bar{t}$. The black circles correspond to $Q = 10^{-9}$ and the usual biasing setup, where the applied voltages alternate between contiguous electrodes. The orange squares differ in that biases alternate in groups of two, as explained in Fig. 5.1a. The blue triangles assume colder antihydrogen (2 mK), a shallower trap ($U_T = 3\,\text{mK}$), and $Q = 5 \times 10^{-11}$. In all cases, the standard deviation was chosen to be 20% of $\bar{t}$. The dashed lines are not interpolations and are there only to guide the eye. A time step $t_{step} = 3.5\,\mu\text{s}$ was used for most simulations; however, calculations with $t_{step} = 0.35\,\mu\text{s}$ (red) and $t_{step} = 35\,\mu\text{s}$ (green) corroborate that these results are valid for other values of $t_{step}$ as well.

mechanism is stochastic heating in energy space, as described in sec. 5.2.

This observation is supported by the separation between the lines of different heating amplitudes, which gives the scaling of heating with variations in $\langle\Phi\rangle_\Delta$. According to eqn. 5.1, by keeping all parameters the same except $\langle\Phi\rangle_\Delta$, the following approximate relation holds: $N_{100V}/N_{350V} = (\langle\Phi\rangle_\Delta^{350V}/\langle\Phi\rangle_\Delta^{100V})^2 \approx (350/100)^2 = 12.3$. Simulation data can be compared to this value by identifying $t_{1/2}^{100V}/t_{1/2}^{350V} \approx (N_{100V}\bar{t}_{100V})/(N_{350V}\bar{t}_{350V}) = N_{100V}/N_{350V}$, since $\bar{t}$ is the same in these simulations, and using the value of $t_{1/2}$ at a fixed $Q$, which is arbitrarily chosen here to be $Q = 10^{-9}$. Then $t_{1/2}^{100V}/t_{1/2}^{350V} = (35.3 \pm 4.6)/(3.51 \pm 0.40) = 10.06 \pm 1.71$, in relatively good agreement with the scaling expected theoretically. Similarly, $(t_{1/2}^{35V}/t_{1/2}^{100V}) = (240.8 \pm 29.5)/(35.3 \pm 4.6) = 6.82 \pm 1.23$ compared to the expected $(100/35)^2 = 8.16$. The calculation $(t_{1/2}^{35V}/t_{1/2}^{350V}) = (240.8 \pm 29.5)/(3.51 \pm 0.40) = 68.6 \pm 11.66$ is nevertheless farther

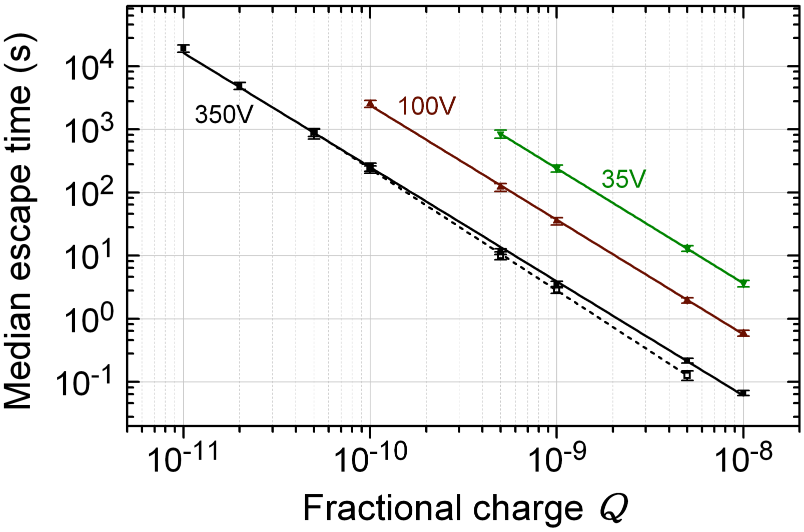

Figure 5.5: Median escape time $t_{1/2}$ versus fractional charge $Q$ for stochastic signals with $\bar{t} = 300\,\mu$s, $t_\sigma = 60\,\mu$s and amplitudes 350 V (black), 100 V (brown) and 35 V (green). Solid lines are least-squares linear fits of the data. The empty squares are data for 350 V calculated by setting a fixed magnetic trap depth, and the dashed line is their linear fit. In all cases, error bars show errors $t_{error}$ as calculated in sec. 5.2.

from the expected $(350/35)^2 = 100$, a fact that may show that assuming that $t_{1/2}^{V_1}/t_{1/2}^{V_2} \approx N_{V_1}/N_{V_2}$ and $(\langle\Phi\rangle_\Delta^{V_1}/\langle\Phi\rangle_\Delta^{V_2})^2 \approx (V_1/V_2)^2$ may be an oversimplification.

The dashed black line in Fig. 5.5 is a fit of the simulation results obtained for a heating signal with amplitude 350 V, $\bar{t} = 300\,\mu$s and $t_\sigma = 60\,\mu$s, identical to the one used in the calculation of the solid black line, but with the difference that here simulations were forced to stop immediately after particles passed the energy trap-depth limit of 0.54 K; of course, simulations also stopped when particles left the trapping region, as in the original case. The motivation for this test is the observation that for values of $Q$ which exhibit $t_{1/2} < 1000\,$s, particles are able to reach energies higher than the trap-depth before they escape, presumably due to the finite lifetime of quasi-bound orbits. This behavior can be interpreted as a change in the "effective" trap-depth $U_T$ that depends on $Q$, which leads to a modification of the scaling of $t_{1/2}$ vs. $Q$. By setting an artificial hard limit on the energies in the trap, this behavior can be suppressed, as the plot shows. The scaling of $\log(t_{1/2})$ vs. $\log(Q)$ is $-1.93 \pm 0.019$, closer to the value '-2' expected from eqn. 5.1.

Finally, the linear fits in Fig. 5.5 provide a way to estimate the value of $\langle\Phi\rangle_\Delta$. By using the y-intercept $y_{int}$, eqn. 5.1 suggests that $y_{int} = 2\,\log(U_T\sqrt{\bar{t}}/e\langle\Phi\rangle_\Delta)$, and therefore $\langle\Phi\rangle_\Delta = \sqrt{\bar{t}}\,(U_T/e)\,10^{-y_{int}/2}$. The fact that the parameter estimated from the fit appears in an exponent means that this result is not very precise; nevertheless, by using $U_T = 0.54\,\text{K} = 4.65 \times 10^{-5}\,\text{eV}$ and the value of $y_{int} = -16.9 \pm 0.18$ obtained from the simulations with a fixed trap depth and an excitation amplitude of 350 V, $\langle\Phi\rangle_\Delta^{350V} \approx 230 \pm 50\,\mathrm{V}$.

## 5.4 Experimental procedure

Section 5.3 showed that anti-atoms heated with a stochastic signal can be forced to escape from the magnetic trap. Since heating only occurs if antihydrogen is charged, the determination of survival of anti-atoms after being subject to stochastic heating gives a way to establish bounds on its neutrality.

Experimentally, antihydrogen would be trapped and heated for a fixed time $T$, after which the magnetic trap would be turned off and any surviving anti-atoms would be detected (see sec. 2.3); if $Q \neq 0$, survival rates would be different than the ones obtained without heating. Notice that there is no need to determine locations of annihilations precisely in this case.

Only few trials are needed in order to reach statistical significance. Figure 5.5 gives the simulated times for which half the particles with a given $Q$ escape. By fixing a total heating time $T = T_0$ (corresponding to some $Q_0$ on the plot) and repeating the experiment $M$ times, the number of surviving particles $K$ under the hypothesis that $Q = Q_0$ follows approximately a Poisson distribution with parameter $\lambda = 0.5\,M\,r_{rate}$, where $r_{rate}$ is the trapping rate without heating. Thus, the hypothesis (and in fact $Q \geq Q_0$, since the survival probability is lower for higher values of charge), can be rejected with confidence '$1 - \alpha$' if

$$\mathrm{Poisson}(K;\lambda) = \frac{\lambda^K e^{-\lambda}}{K!} < \alpha \tag{5.2}$$

If only very few trials are possible, simulations can be used to calculate survival probabilities lower than 0.5 to reach statistical significance at lower $M$ at the cost of more relaxed bounds on $Q$. Figure 5.6 shows results obtained with the same code as in sec. 5.3, but fixing in this case the heating time $T$ and using the empirical CDF (see Fig. 5.2) to determine the probability that an anti-atom with assumed fractional charge $Q$ would have escaped the trap in the interval $0 \leq t \leq T$. By selecting in the plot a particular $Q = Q_0$ for which the probability $p_0$ of escaping is significant, a smaller Poisson parameter $\lambda = (1 - p_0)\,M\,r_{rate}$ can be obtained that allows a hypothesis rejection with equal confidence and less number of trials $M$.

In order to confirm that the experiment is working properly and have a reliable value for $r_{rate}$, trials with no heating would have to alternate with stochastic heating ones. If an effect were observed, confirmation of the expected $\langle\Phi\rangle_\Delta$ and $\sqrt{N}$ scaling (eqn. 5.1) could be used for determining that the observation is truly due to stochastic heating.

It would also be important to establish that vacuum degradation is not responsible for destroying the anti-atoms. Such degradation could result from arcing between the electrodes, and could be eliminated as a source of concern by running the control case with the static potential of Fig. 5.1 applied. Since the probability of an arc increases monotonically with time, the system would surely arc with such a static potential if it arced with the oscillating potential used in stochastic heating. Also, the oscillating fields could cause $I^2R$ heating.

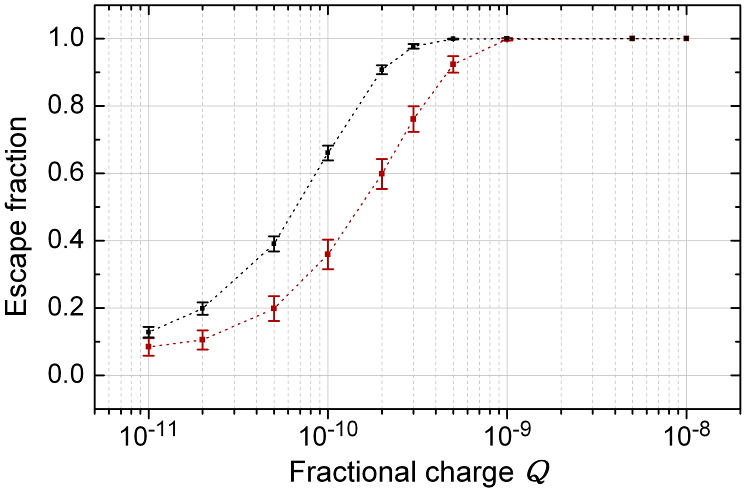

Figure 5.6: Escape fraction of anti-atoms with assumed fractional charge $Q$ for different values of total heating time $T$. The black points correspond to $T = 500\,\mathrm{s}$ and dark red corresponds to $T = 100\,\mathrm{s}$. The dashed lines are not interpolations and are there only to guide the eye. Biases of ±350 V were used in both cases. The error bars are determined from the CDF bounds in Fig. 5.2 and establish a 95% confidence interval for the true escape probability.

Such heating could be studied by applying a spatially uniform oscillating potential, which would have the same $I^2R$ heating effect as the regular oscillating potential, but would not induce stochastic heating.

## 5.5 Improving the method

With expected improvements to the vacuum, it is reasonable to assume that trapping times of 10000 s can be achieved. Then $N \approx 3 \times 10^7$ is in principle possible, and eqn. (5.1) suggests that $|Q|$ could be bound to $3 \times 10^{-11}$. The simulations (Fig. 5.5) show that this bound is actually lower, around $1.5 \times 10^{-11}$.

With laser cooled anti-atoms at 20 mK [47] the trapping potential could be reduced to perhaps $U_T = 30\,\mathrm{mK}$, while still retaining most of the anti-atoms, and the bound would become $3 \times 10^{-12}$ (Fig. 5.7). Adiabatic expansion cooling of the anti-atoms might reduce their temperature by a further factor of ten, yielding a bound of $7 \times 10^{-13}$. This bound approaches the limit where antihydrogen-polarization effects are expected to be non-negligible.

Atoms acquire a dipole moment $\vec{p} = \alpha\vec{E}$ in the presence of an electric field $\vec{E}$, where $\alpha$ is a constant (the *atomic polarizability*) [35, ch. 4]. These dipoles, in turn, experience a force due to the electric field equivalent to $\vec{F}_{pol} = (\vec{p} \cdot \nabla)\vec{E} = \alpha(\vec{E} \cdot \nabla)\vec{E} \approx (\alpha/2)\nabla(|\vec{E}|^2)$, where effects of induced electric fields from changing magnetic fields have been neglected as the

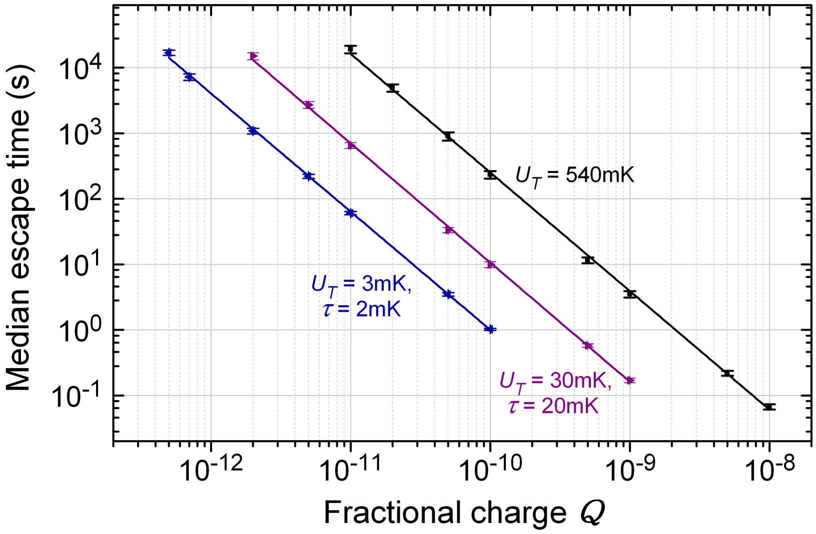

Figure 5.7: Median escape time versus fractional charge for cold antihydrogen distributions and a stochastic signal of amplitude ±350 V. Purple points are simulation results obtained with an initial energy distribution at a temperature $\tau = 20\,\text{mK}$, a trap depth $U_T = 30\,\text{mK}$ and $\bar{t} = 1.3\,\text{ms}$. Blue points were obtained using $\tau = 2\,\text{mK}$, $U_T = 3\,\text{mK}$ and $\bar{t} = 4\,\text{ms}$. The black points and line are the same as the 350 V data in Fig. 5.5, shown here for comparison.

trapping fields are constant. Compared to the usual electrostatic force for a particle with fractional charge $Q$, given by $\vec{F}_e = Qe\vec{E}$, polarization would be of comparable magnitude when $|\vec{F}_e|/|\vec{F}_{pol}| \sim 1$, that is, when the fractional charge has a value

$$|Q| < \frac{\alpha}{2e}\frac{|\vec{E}|}{L} \tag{5.3}$$

where $L$ is a typical length of variation of $|\vec{E}|$. For the setup used (see Fig. 5.1b), the largest on-axis $z$-component of the field is $\sim 10\,\text{V/mm}$, and $L \approx 1\,\text{cm}$. Assuming that the electric polarizability of antihydrogen is the same as that of hydrogen, $\alpha_{\bar{H}} \approx \alpha_H = 7.42 \times 10^{-41}\,\text{m}^2\text{F}$ [48], polarization would be important for $Q < 2 \times 10^{-16}$.

The radial and axial components of the electric field attain very large values close to the gaps between the electrodes. Depending on the biases used, the fields can be of the order of kV/mm or more, with sharp radial and axial increases as particles approach the gaps. Assuming then $|\vec{E}| \sim 1\,\text{kV/mm}$, equality of polarization and electric forces occurs when $Q \sim 2 \times 10^{-13}$. However, the volume close to the gaps is small compared to the overall volume of the trap, so the high values of the fields may have a small overall effect.

Simulation results for $Q = 0$ and different values of electric polarizability are plotted in Fig. 5.8. They show that, under the influence of a stochastic signal, polarization produces a heating that forces particles to escape from the confining well, in a way similar to the $Qe\vec{E}$

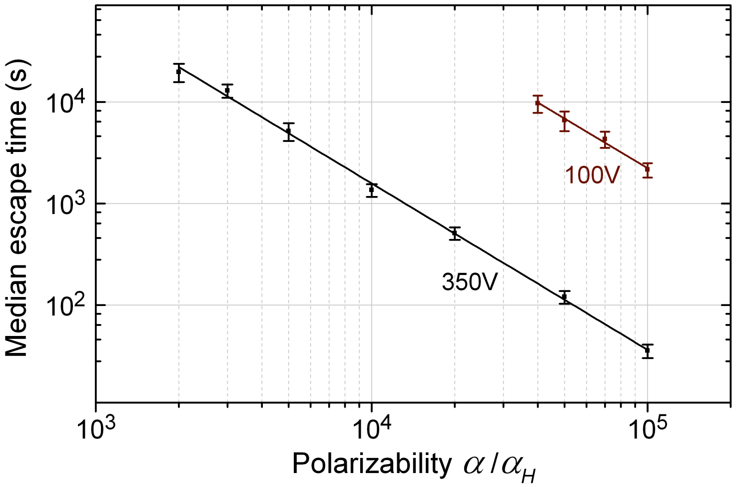

Figure 5.8: Median escape time $t_{1/2}$ of $Q = 0$ anti-atoms for different values of antihydrogen atomic polarizability $\alpha$ (assuming ground-state anti-atoms). Simulations used $U_T = 3\,\mathrm{mK}$, $\tau = 2\,\mathrm{mK}$, and a stochastic signal with $\bar{t} = 4\,\mathrm{ms}$ and amplitudes 350 V (black) and 100 V (brown). The atomic electric polarizability is given in units of $\alpha_H = 7.42 \times 10^{-41}\,\mathrm{m}^2\mathrm{F}$, the polarizability of atomic hydrogen.

force. Since in this case the force depends on $\nabla(|\vec{E}|^2)$, it is not expected that the heating proceeds in the same manner. In fact, a linear fit of the results obtained using a 350 V amplitude drive gives $\log(t_{1/2}) = (-1.639 \pm 0.032)\log(\alpha/\alpha_H) + (9.76 \pm 0.13)$; that scaling (-1.639) is different from the $\approx -1.81$ observed for stochastic heating. Also, the separation between the fits of the 350 V and 100 V data indicate a variation in heating versus electric field different than linear.

One first important observation from Fig. 5.8 is that in order for polarization of antihydrogen to have an effect comparable to that of stochastic heating in the range of trapping times of interest ($\leq 10000\,\mathrm{s}$), its electric polarizability would have to be a factor of $\sim 1000$ bigger than that of hydrogen. Using the scaling provided by the linear fit to extrapolate the simulation results and obtain a value of $t_{1/2}$ for $\alpha = \alpha_H$, it would take approximately $5.8\times10^9$ s to evaporate half of the particles out from the trap (a number too big to be of actual experimental relevance). In comparison, by extrapolating the fit for stochastic heating on the coldest antihydrogen in Fig. 5.7, where $\log(t_{1/2}) = (-1.804 \pm 0.014)\log(Q) - (18.04 \pm 0.15)$, polarization would have effects of comparable magnitude to a stochastically heated anti-atom with $Q = 3.9 \times 10^{-16}$. This prediction is in good agreement with eqn. 5.3, assuming values of on-axis electric field variations.

Second, polarizability contributes to *heating*. Simulations that include both effects, stochastic heating and polarization, run on a shallow trap of depth $U_T = 3\,\mathrm{mK}$, using particles with $Q = 7 \times 10^{-13}$, $\alpha = 3000\,\alpha_H$, at an initial temperature $\tau = 2\,\mathrm{mK}$, showed a median escape time $t_{1/2} = 2765.2 \pm 355.6\,\mathrm{s}$ (with 95% confidence), indicating an improved heating rate over the results obtained without including polarization (Fig. 5.7). Thus, simulations using stochastic heating alone (not including polarization) give conservative bounds that should be valid.

It is also conceivable that larger electrode biases can be used. The 350 V drive amplitude is a conservative limit set such that the internal electrical connections in ALPHA1 would not be stressed too close to their point of failure, but it can be raised if suitable connectors and electronics are used. Current technologies of power semiconductors (like VS Holding's 8821/2/3 single-pole double-throw solid state relay) can allow for drives that switch between ±500 V, provided the capacitance of the electrodes and their associated circuitry is sufficiently small that currents handled by the system are not too large, and provided that high voltage regulating capacitors can be found for the task at hand.

There are, however, theoretical considerations that limit the amplitude of the fields. Electrostatic potentials for stochastic heating may be high enough that static fields alone can force fractionally-charged particles to be expelled from the trap. The shape of the potentials prevents axial confinement from being lost; however, since the radial electric field never changes sign for a given $z$ (see Fig. 5.1c), confinement may be lost in the radial direction.

An estimate of this effect can be calculated in a way similar to that in sec. 3.1. From Fig. 5.1a (black trace), it can be seen that the on-axis potential corresponding to applied biases $\pm\Phi_{bias}$ is $\approx \pm(1/5)\,\Phi_{bias}$ or less for the central electrodes. Therefore, a particle with fractional charge $Q$ would gain enough energy from the electric field and escape when $(4/5)\,|Qe\Phi_{bias}| > U_T$, where $U_T$ is the magnetic trap depth (as defined before). In other words, by applying a static potential with the shape of Fig. 5.1 and amplitude $\Phi_{bias}$, particles with

$$|Q| > \frac{5}{4}\frac{U_T}{e\Phi_{bias}} \tag{5.4}$$

may be lost as a consequence of the static fields and not stochastic heating. Equation 5.4 therefore sets a limit of $Q$ above which the scaling in eqn. 5.1 is not expected to hold. This is roughly equivalent to what is expected from eqn. 5.1 when setting $N = 1$.

One final consideration are electromagnetic effects. The rapid transitions of the electrostatic potential produce magnetic fields that may interact with the magnetic moment of the anti-atom and alter its dynamics. An estimate of the fractional charge $Q$ for which these effects can no longer be neglected can be made by comparing $\vec{F_e} = Qe\vec{E}$ to the magnetic force $\vec{F_\mu} = \mu_B \nabla(|\vec{B}_{ind}|)$ (see eqn. 2.4). From the Maxwell-Ampere equation, $\nabla \times \vec{B}_{ind} = (1/c^2)\,(\partial\vec{E}/\partial t)$, it can be seen that $|\vec{B}_{ind}|/L \approx (1/c^2)\,(|\Delta\vec{E}|/\Delta t) \approx (2/c^2)\,(|\vec{E}|/\Delta t)$, where $L$ is some typical length over which $\vec{B}_{ind}$ varies, and $\Delta t$ is the time it takes to flip the voltages. Now, $|\vec{F_\mu}| \approx \mu_B(|\vec{B}_{ind}|/L) = \mu_B(2/c^2)\,(|\vec{E}|/\Delta t)$ and therefore, $|\vec{F_e}|/|\vec{F_\mu}| \sim 1$ implies

$$|Q| < \frac{2\mu_B}{c^2 e}\left(\frac{1}{\Delta t}\right) \tag{5.5}$$

Equation 5.5 shows that electromagnetic effects can be safely ignored for transition times $\Delta t \sim 0.1\,\mathrm{ms}$ typical of the electrode biasing plus filtering systems built for ALPHA1 (see sec. 2.1), but they may be of concern for other experiments.

# Conclusions

A method based on a retrospective analysis of data collected in the 2010 and 2011 ALPHA experimental runs, and on the study of the axial location of annihilations of trapped anti-atoms after being released from the confining trap, has been developed to measure the electrical charge of antihydrogen.

The technique makes use of the electric fields left on during the magnetic trap shutdown in most trapping experiments performed in ALPHA1. If antihydrogen were electrically charged, these "bias fields" would affect the trajectories of anti-atoms by pushing them towards the ends of the trap, thereby changing their average annihilation location. The two configurations of fields used, Bias-Left and Bias-Right, allowed then to define the experimentally-measureable parameter $\langle z\rangle_\Delta \equiv 0.5\,[\langle z\rangle_R - \langle z\rangle_L]$, where $\langle z\rangle_L$ ($\langle z\rangle_R$) is the average annihilation location obtained in Bias-Left (Bias-Right) runs, that would only be different from zero if the fractional charge of antihydrogen $Q$ were non-zero.

A computer model of the apparatus (ch. 3) was developed in order to calculate the effect of the electric fields on anti-atoms with a presumed $Q$, and used to predict corresponding values of $\langle z\rangle_\Delta$. By inverting the relation and using the $\langle z\rangle_\Delta$ calculated from experimental observations, a final value of fractional charge $Q$ of antihydrogen is obtained (ch. 4):

$$Q = (-1.34 \pm 1.84 \pm 0.56) \times 10^{-8} \qquad \text{(90\% confidence)}$$

where the errors come from the reduced number of experimental events ($\pm\,1.84 \times 10^{-8}$), and systematic effects ($\pm\,0.56 \times 10^{-8}$) which had to be carefully determined and quantified.

This value is compatible with $Q = 0$, and constitutes a factor of $\sim 10^{-6}$ improvement in accuracy over the only previous *direct* measurement of the charge of antihydrogen [14]. Since the charge of the antiproton is known to $|(|q_{\bar{p}}| - e)/e| \leq 7 \times 10^{-10}$ [10], this result can be used to infer a bound on the charge anomaly of the positron of $(q_{e^+} - e)/e = (-1.3 \pm 1.8 \pm 0.6) \times 10^{-8}$ (90% confidence) under the very likely assumption that the charge of antihydrogen is equivalent to the sum of the charges of the antiproton and the positron. This constitutes an improvement of a factor of $\sim 2$ in precision over the previously recognized experimental value of the charge of the positron [16].

Systematics are smaller than the counting error. Therefore, this measurement of $Q$ is dominated by the sample size and a similar procedure could conceivably be used to obtain tighter bounds, perhaps in the new ALPHA2 apparatus being commissioned at CERN's AD Hall.

A different approach, however, may lead to a much tighter bound. The studies in ch. 5 show that evaporation of anti-atoms from the magnetic trap using stochastic heating can lead to sensitivities of $Q \approx 5 \times 10^{-11}$ under ALPHA1 experimental conditions. Possible future improvements in ALPHA2, such as laser plus adiabatic cooling, and better vacuum in the trap, can further lower this value to $Q \approx 7 \times 10^{-13}$. This technique has the advantage that statistical significance can be reached in comparatively few runs without the need to precisely measure the location of anti-atom annihilations. It does, however, require the construction of separate hardware, which can anyway be built externally to the apparatus using currently available technologies of power electronics.

# Appendix A

# Residual gas analysis using an autoresonant drive

As mentioned in chapter 2, the capabilities of ALPHA1 went beyond those of a common particle trap. The very complete diagnostic systems and the many tools available for manipulating particles permitted interesting studies such as the one discussed in this appendix.

Here, the residual gas in the apparatus is analyzed using a technique based on autoresonant ion extraction from an electrostatic potential well. The discussion follows closely the results published in [49], and constitutes a good example of the interesting research done in ALPHA1 in parallel to the studies of antihydrogen.

The residual gas in charged particle traps has important effects on the confined species. It may affect plasma expansion rates [50], allow chemical reactions [51] and, in the case of antimatter plasmas, promote annihilation of the particles. In devices intended to trap antihydrogen [7], it may also determine the lifetime of the trapped anti-atoms. Indeed, for antimatter plasmas, knowledge of the residual gas composition, together with the measurement of the annihilation rate and with suitable cross-section calculations, can be used to determine the residual gas density [52].

For cryogenically cooled traps, composition measurements inside the trap itself are required. Determinations of the gas composition with conventional residual gas analyzers in room temperature regions of the apparatus are not useful because many species condense on the cryogenic trap surfaces, thereby changing the composition of the gas in the trap itself. For example, ALPHA1 operated at an internal system temperature of 9 K and thus the only gases in thermal equilibrium with the wall that were not expected to have largely condensed were helium, hydrogen and neon [53]. There was, however, the possibility of a "wind" of other species, such as $N_2$ and $O_2$, flowing from warmer areas of the apparatus, including some areas at room temperature that were not closed off from the trap interior.

Because of limited access, strong magnetic fields and cryogenic temperatures, it was not possible to implement conventional residual gas analysis (RGA) techniques in the ALPHA1 apparatus. Consequently, a technique was developed that relied on autoresonant ion extraction from an electrostatic potential well. This method was related to the one used in a commercial autoresonant mass spectrometer [54, 55] and could be implemented in ALPHA1 without modification to the trap geometry. It may also be applicable to ALPHA2 or other Penning trap devices where access is limited.

Autoresonance is a very general phenomenon occurring in many different dynamical systems [56, 18, 57] that allows a weakly damped, driven, nonlinear oscillator to phase lock to its drive. For example, consider an initially quiescent oscillator with a soft non-linearity (an oscillation frequency that decreases with amplitude). If the oscillator is subject to a swept-frequency drive that starts well above the oscillator's linear frequency and which sweeps downward through and below the linear frequency, then phase-locking will occur automatically, subject to some understood criteria. It has been shown that the drive amplitude must be proportional to the sweep rate raised to the 3/4 power for phase locking to occur [58, 56]. The oscillator amplitude will then adjust itself to match the drive frequency and, consequently, can be controlled (and made very large) simply by decreasing the drive frequency. This autoresonant process will work even with a very weak drive [58]. It will also occur when the oscillator is not initially quiescent, but then the phase locking condition is more complicated, and the oscillator can lock to subharmonics of the drive [59].

The residual gas composition was measured by ionizing the residual gas with hot positrons (see Fig. A.1), whereupon the positrons and ions were separated, with the latter placed in an anharmonic electrostatic potential well. Autoresonance was then used to selectively extract the ions from the well, where the drive frequency at which ions escaped depended on their mass-to-charge ratio. The escaping ions were collected with an MCP (Microchannel Plate) amplifier [26], and the amplified charge signal was compared to simulations of the process to determine the gas composition.

## A.1 Experimental setup

As mentioned above, the experiments did not require any modifications to the geometry of ALPHA1. The manipulations in this case only dealt with charged particles, so the full capabilities of the Penning-Malmberg trap in the apparatus were employed (sec. 2.1). The neutral trap (sec. 2.2) was de-energized at all times.

In a typical run, $\sim 10^7$ positrons were brought from the Surko-type positron accumulator [25] into the main trap [60] (Fig. A.2a) with an energy of $\sim 80\,\mathrm{eV}$, and trapped in an electrostatic potential well with a minimum near the center of the electrode stack. The confined positrons bounced in this initial electrostatic well with enough energy to ionize atoms or molecules of the residual gas through collisions [61, 62, 63]. Ions with low enough energy were trapped in the well along with the positrons. The positrons cooled through cyclotron radiation with a characteristic time of $4\,\mathrm{s}$ (at a magnetic field of $1\,T$), and sympathetically cooled the ions (Fig. A.2b) over a time interval of $\sim 80\,\mathrm{s}$, resulting in both ions and positrons accumulating around the potential well minimum. Positrons were then removed by applying a fast voltage pulse to one of the confining electrodes, thereby briefly opening the trap. The fast-moving positrons escaped, while the slow-moving ions did not (Fig. A.2c). The confin-

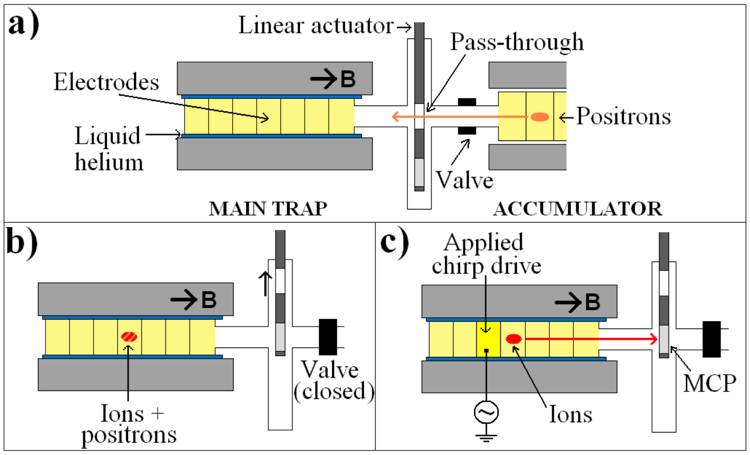

Figure A.1: Experimental setup for residual gas analysis experiments. The main ALPHA1 trap and positron accumulator were separated by a valve which was only opened for positron transfers. A linear actuator was also located between the traps to either allow positrons to pass through, or insert an MCP for charge detection (see also Fig. 2.2). (a) Configuration for positron transfers. (b) Configuration for charged particle manipulations. (c) Detection of autoresonantly extracted ions by charge amplification with the MCP.

ing well was then modified to a predefined anharmonic shape and, after a short wait, the remaining ions were subjected to a voltage chirp drive applied to a neighboring electrode (Figs. A.2e and A.2f).

When a suitably tailored chirp was used, the axial motion of some of the confined ions phase-locked to the drive. As the chirp swept down in frequency, the energy of these autoresonantly driven ions increased until they were able to escape the well. These ions then followed the magnetic field lines onto an MCP [26], where charge was amplified through electron cascading upon impact (Fig. A.1c). Electrons emitted from the back of the MCP were deposited on a charge collection plate and the resulting voltage signal was filtered, digitized and stored in a computer. Once the signal had been stored, additional digital filtering was performed for further noise reduction, and charge information was recovered from the voltage signal by digitally deconvolving the collection plate system response. Since the timing between the escaped ions and the drive chirps was recorded, the frequencies at which ions escaped could be plotted. Time of flight ($\sim 1\,\mu$s) effects were negligible, as they occurred at a time scale much shorter than the variations of charge at the collection plate ($\sim 1\,$ms) typical of the measurements.

Different ion species had different steady-state bounce frequencies in the anharmonic well determined by their mass-to-charge ratio. Autoresonance forced particles of each particular species to follow the energy versus frequency paths shown in Fig. A.3 and reach the top of the well (at 49.1 eV, measured with respect to the potential minimum at axial position 0;

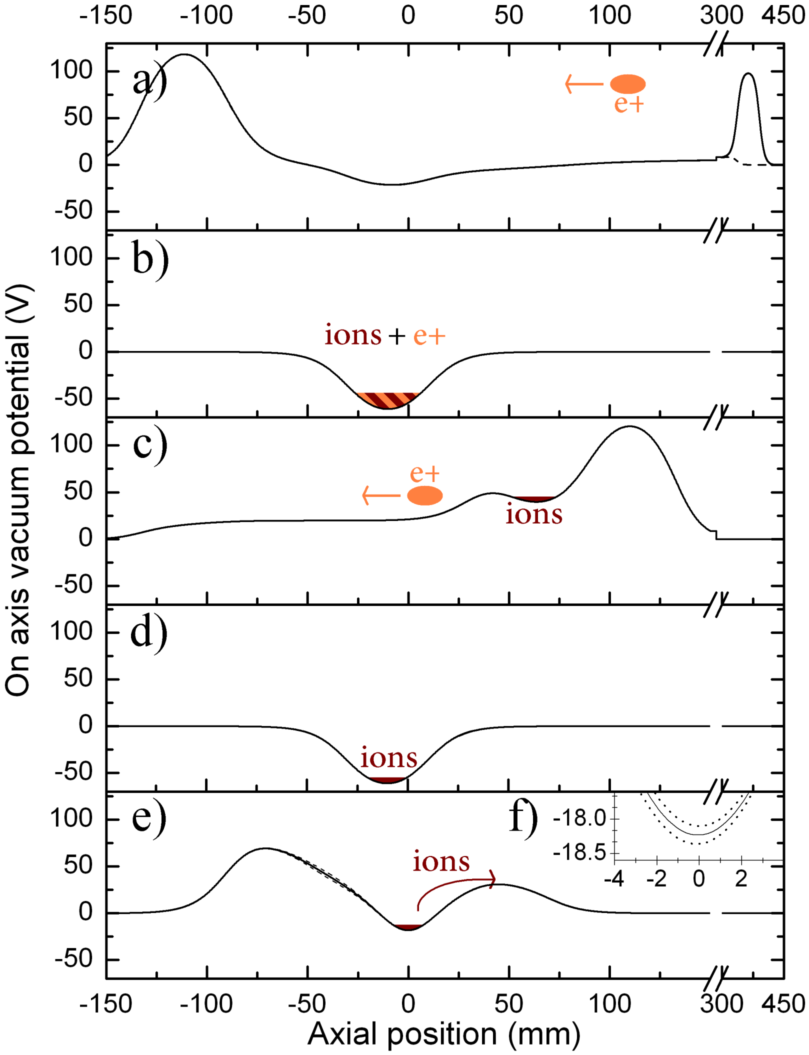

Figure A.2: Electrostatic potential manipulations during a typical residual gas analysis run. (a) Positrons were brought into the main trap from the right, at a time when there was no potential wall at the axial position ∼ 400 mm (dashed line). As soon as they entered, the potential wall was erected (solid line) and positrons were confined and forced to bounce inside the experiment. Ions were formed through collisions of the positrons with the residual gas. (b) Ions and positrons cooled down and accumulated at the bottom of the potential well, which was meanwhile modified to a more localized shape. (c) Positrons were then separated and discarded, and (d) ions were placed back in a deep well. (e) Finally, ions were placed at the bottom of an anharmonic well (solid line). A chirp was then applied that autoresonantly forced the ions to escape onto the MCP. The maximum electrostatic potential variations due to an applied 5 V chirp are shown as dashed lines. (f) Potential variations due to the chirp near the well minimum.

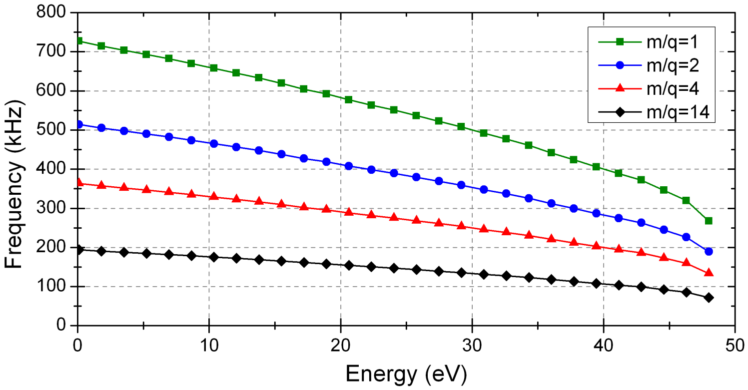

Figure A.3: Calculated bounce frequencies in the anharmonic potential well used for the experiments, of particles with mass-to-charge ratios 1 (green-squares), 2 (blue-circles), 4 (red-triangles) and 14 (black-diamonds), in units of proton mass/fundamental charge ($m_p/e$). Here, and in what follows, the energy is chosen to be zero at the potential well minimum.

see Fig. A.2e) at different drive frequencies. By analyzing the charge signal at the collection plate as a function of the drive frequency, it was possible to identify the different species in the well at the time of the chirp.

Separate images of ions arriving at the MCP taken with a CCD camera [26] indicated charges concentrated within $\sim 1\,\mathrm{cm}$ of the trap axis. Since ions were expected to follow the field lines closely when extracted, and the magnetic field was $\sim 40$ times stronger inside the trap than at the location of the MCP, it could be concluded that ions were located within $\sim 1\,\mathrm{mm}$ of the axis of the trap during the experiments.

## A.2 Simulations

The simulations used for the residual gas analysis were very different from the ones described in chapter 3. In this case, a particle stepper code was written using a C-based Runge-Kutta method with adaptive step size control [64] to simulate single-particle motion of ions in the electrostatic potential well. Only the effects of the electric field on the charged particles were included in the model; the magnetic field only manifested itself by keeping confinement in the radial direction. Furthermore, and consistent with the experimental observations, it was assumed that the ions remained close to the trap axis at all times. Thus, in the end, the model reduced to the one dimensional (1D) motion of a charged particle in the anharmonic well of Fig. A.2e, plus an applied voltage chirp.

Given a value of mass-to-charge ratio of an ion '$m/q$' (in units of $m_p/e$, where $m_p$ is the proton mass and $e$ is the fundamental charge) and specific initial conditions of energy and phase, the motion under the influence of the chirp was integrated. The escape time '$t$' was

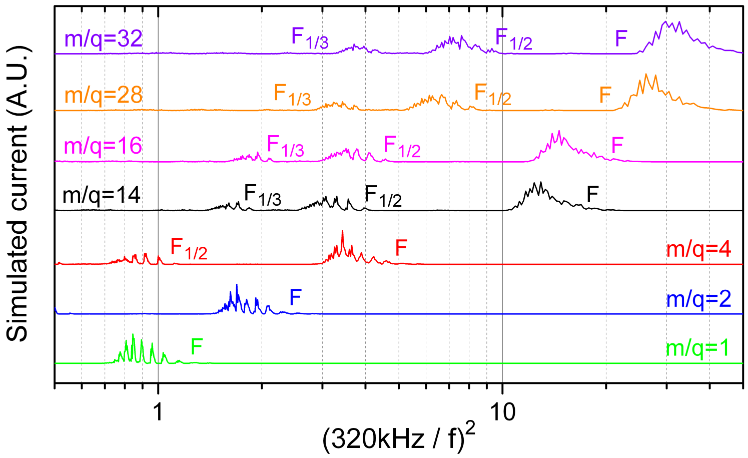

Figure A.4: Simulation histograms obtained for a 100 ms, 1 MHz − 10 kHz, 4 V linear chirp applied to particles with $m/q =$ 1, 2, 4, 14, 16, 28 and 32 and initial energies distributed uniformly in 0 − 49.1 eV. This energy range includes all possible initial energies and shows the full complexity of the particle dynamics in this nonlinear system. The peaks marked with an 'F' correspond to particles driven out by the fundamental of the chirp, while '$F_{1/2}$' and '$F_{1/3}$' mark the first and second subharmonics.

measured, that is, the time when the particle left the potential well (if it left at all) after the start of the chirp, and the procedure was repeated over a wide range of possible values of initial conditions. Using this simulated data, normalized histograms of number of escaping particles (with initial energy and phase in an experimentally expected range) versus escape time were created. Finally, the histograms were plotted against $(K/f)^2$, where $f$ was the frequency of the chirp at time '$t$' and $K$ was an appropriately chosen constant (Fig. A.4).

The choice $K = 320\,\mathrm{kHz}$ normalized the horizontal axis such that $H^+$ escaped at $(K/f)^2 = 1$. Since bounce frequencies scale like $f \sim \sqrt{q/m}$ (true even for anharmonic potentials), the $(K/f)^2$ mapping scales the escape locations of different species linearly with their mass-to-charge ratio. It also allows for plots with features that are independent of the length and functional form of the chirp, although only linear chirps were used for the discussion in this appendix.

The simulations showed that ions with enough initial energy could be prematurely carried out of the potential well by subharmonics of the chirp drive [59]. This effect was responsible for the appearance of additional peaks in the simulation histograms in locations of $(320\,\mathrm{kHz}/f)^2$ far in numerical value from $m/q$. Therefore, care had to be taken in the analysis to distinguish peaks due to fundamental frequencies of the sweeps from subharmonic-produced ones.

The simulations were restricted to plausible species, namely $H^+$ $(m/q = 1)$; $H_2^+$ and $He^{++}$ $(m/q = 2)$; $He^+$ $(m/q = 4)$; $N^+$ and $N_2^{++}$ $(m/q = 14)$; $O^+$ and $O_2^{++}$ $(m/q = 16)$; $N_2^+$

($m/q = 28$); and $O_2^+$ ($m/q = 32$). $N^+$ and $O^+$ were also analyzed due to the possibility of positron-induced dissociation of the $N_2$ and $O_2$ molecules in the range of energies considered [61, 62, 63].

Finally, it is important to say that attenuation of the chirp due to high pass filtering at the electrodes (used to shield the experiment from noise and decouple the chirp drive from the electrode bias voltages; see sec. 2.1) became important at around $(320\,\mathrm{kHz}/100\,\mathrm{kHz})^2 = 10.2$. Thus, it was expected that peaks at locations larger than 10.2 were increasingly difficult to observe in the experimental traces.

## A.3 Experiments

The first set of measurements involved changing the start frequency of the chirps while keeping the sweep rate fixed. As the calculated ion bounce frequencies for the anharmonic potential well show (Fig. A.3), light particles could not phase lock to chirps with low start frequencies, and consequently, the peak structure of the traces should vary for different choices of start frequencies. Ions could escape due to subharmonics of the chirp at frequencies that were integer multiples of the escape (maximum energy) frequencies shown in Fig. A.3. Thus, if for one particular species one chose a sufficiently low start frequency and swept downwards (as is always the case), the subharmonics of the chirp could not excite particles of that species.

Figure A.5 shows the experimental traces obtained for different choices of start frequencies and compares them to simulations made for ions with initial energies in the range $0-1.5\,\mathrm{eV}$, consistent with separate experimental measurements of the initial ion energies when the trap was at 9 K. The plots show that the simulations capture the main features of the dynamical system and are in good agreement with the experiments. They also allow an interpretation of the charge peaks. The group of peaks labeled "A" (in Fig. A.5), for example, is consistent with the presence of $He^+$. Although the simulations show that these peaks could also indicate the presence of $H^+$, the fact that there are at most very small peaks at $(320\,\mathrm{kHz}/f)^2 = 2$ suggests that there is no $H_2$ in the residual gas, and therefore, no normal source [65] of $H^+$. Group B is also consistent with $He^+$, although it may have traces of $N^+$, $N_2^{++}$, $O^+$ or $O_2^{++}$. The disappearance of peaks in Figs. A.5b and A.5c reinforces this conclusion and is consistent with what is expected from Fig. A.3. Group C is consistent with $N_2^+$ or $O_2^+$ at the first subharmonic. Group D is consistent with $N^+$, although (to a lesser extent) it is also compatible with $O^+$. This suggests that $N_2$ and possibly $O_2$ were present in the apparatus.

A further set of measurements involved changing the settings of nitrogen gas (which was used as a buffer gas to facilitate positron capture) pressures in the positron accumulator. When positrons were transferred into the main apparatus (Fig. A.1a), some $N_2$ would also necessarily enter. Consequently, higher $N_2$ pressures in the accumulator should lead to higher $N_2$ pressures in the mass spectrometer region.

Higher concentrations of $N_2$ could have an effect on the energy distribution of the ions (for example, if the fraction of ions compared to positrons is significant, sympathetic cooling

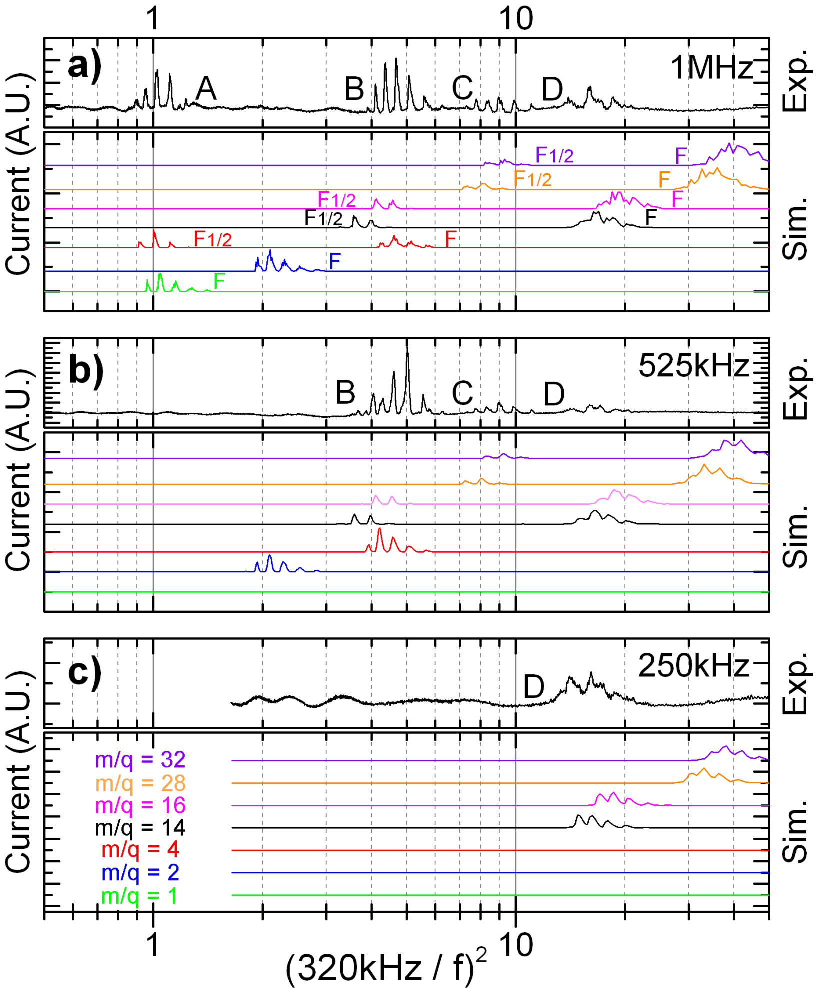

Figure A.5: Experimental traces and simulation results for autoresonant drives with different start frequencies. (a) Experimental trace obtained with a 5 V, 100 ms, 1 MHz − 10 kHz linear chirp (top), and simulation histograms made with a 4 V, but otherwise similar, chirp (bottom). The ∼ 20% difference in drive amplitudes gives a better fit of the data, and is consistent with the uncertainty in the knowledge of the coupling between the drive electronics and the electrode. Unlike Fig. A.4, this plot only includes initial energies in the 0 − 1.5 eV range. (b) Experimental data for a 50 ms, 525 kHz − 10 kHz linear chirp compared to the simulations. (c) Data and simulations for a linear 25 ms, 250 kHz − 10 kHz chirp. See text for explanation of labels A, B, C, D.

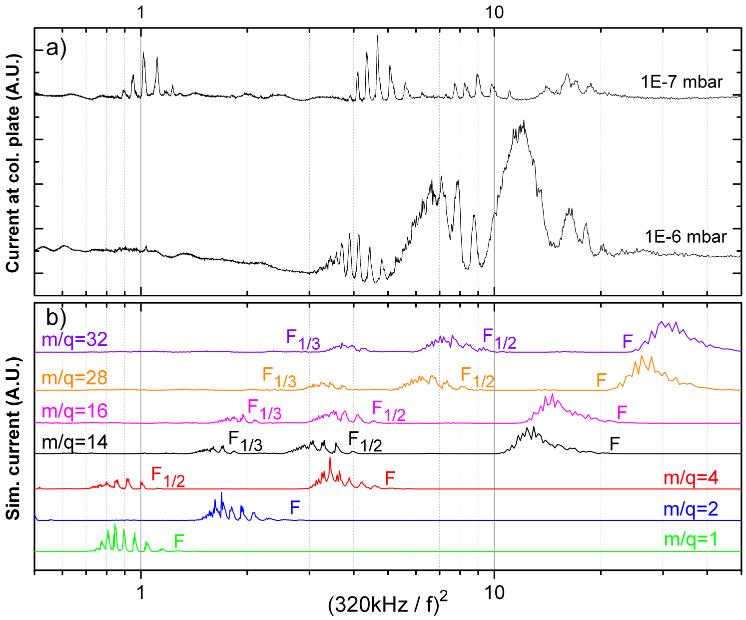

Figure A.6: (a) Experimental traces for different accumulator gas pressures when a 5 V linear, 1 MHz – 10 kHz, 100 ms chirp is used ($10^{-7}$ mbar is the default setting). (b) Simulations for ions with initial energies uniformly distributed between 0 and 49.1 eV, and a chirp amplitude of 4 V.

is no longer as effective), and this in turn could have an impact on the locations of the charge peaks. The simulations showed that, in general, higher ion energies translated into charges escaping slightly earlier in time (i.e. at slightly higher chirp frequencies), and consequently, peaks appearing at lower values of $(320\,\mathrm{kHz}/f)^2$.

Figure A.6a shows experimental data taken at different accumulator pressures. The most striking difference is the appearance of pronounced peaks at $(320\,\mathrm{kHz}/f)^2 = 7 \pm 1.0$ HWHM and $(320\,\mathrm{kHz}/f)^2 = 12 \pm 1.5$ HWHM. Fig. A.6b shows the simulation results for ions with initial energies uniformly distributed in the wider range 0 - 49.1 eV. The simulation traces for $N_2^+$ ($m/q = 28$) and $N^+$, $N_2^{++}$ ($m/q = 14$) provide a possible explanation for the appearance of the experimental charge peaks at $(320\,\mathrm{kHz}/f)^2 = 7, 12$, that is consistent with the expectation that nitrogen should be more clearly seen in the higher pressure trace. The fact that the simulated peaks at $(320\,\mathrm{kHz}/f)^2 = 28$ were not clearly seen experimentally does not contradict this observation because, as stated previously, the chirp was heavily attenuated by the electrode filters at those low frequencies.

Finally, measurements were performed during a cooldown of the apparatus. During this procedure, which lasted ∼ 5 hours, the temperature of the interior of the trap was brought down from ∼ 100 K to 9 K, as measured by the Lakeshore Cernox sensor closest to the trapping region (attached to an electrode located ∼ 30 cm from the center of the trap). The

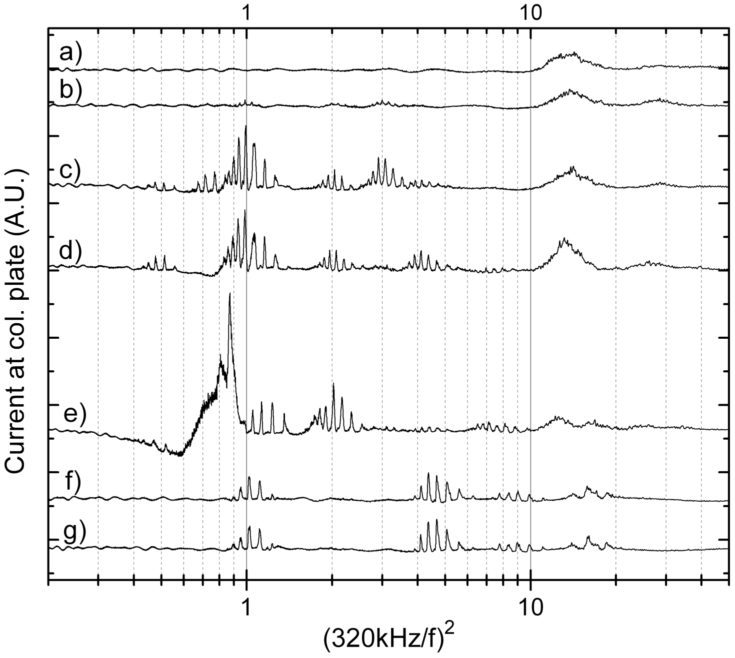

Figure A.7: Experimental traces obtained at different times during a cooldown of the apparatus. Data was taken sequentially from start to end in the order a) through g). A linear 5 V, 1 MHz − 10 kHz, 100 ms chirp was used for all measurements. See text for details of labeling.

change in temperature should produce changes in the residual gas pressure and composition due to cryo-pumping on the walls [53] that should lead to changes in the experimental traces. The changing pressure and density, and the consequent change in the collision frequencies of the particles, might also have an effect on ion formation, and ion-ion and ion-neutral reactions [66], which in turn would affect the detected species and the relative strength of their signals. Also, as discussed above, the changing conditions might affect the energy distribution of the ions, which further complicates the analysis and comparison with the simulations.

Figures A.7b,c,d,e are experimental traces obtained 48 min, 72 min, 102 min and 198 min after the start of cooldown that show the evolution of the vacuum in the trap. Based on the discussion above, the peaks at $(320\,\mathrm{kHz}/f)^2 = 1$ are consistent with $H^+$ and/or $He^+$ at the first subharmonic (notice the changing peak structure around $(320\,\mathrm{kHz}/f)^2 = 1$), and the groups at $(320\,\mathrm{kHz}/f)^2 = 4, 8, 12$ are consistent with $He^+$, $N_2^+$ and/or $O_2^+$, and $N^+$ and/or $O^+$ respectively. The simulations show that the peaks seen at $(320\,\mathrm{kHz}/f)^2 = 0.5, 2$ are consistent with $H_2^+$, while the peaks at $(320\,\mathrm{kHz}/f)^2 = 3$ may indicate the presence of $H_3^+$, which is allowed by the significant cross section of the reaction $H_2 + H_2^+ \rightarrow H_3^+ + H$ at low energies[66]. Figs. A.7 b,c,d also show a small peak close to $(320\,\mathrm{kHz}/f)^2 = 30$ that is consistent with $N_2^+$ and possibly $O_2^+$.

Figures A.7f and A.7g show the final (stable) mass spectra, corresponding to when the apparatus was cold at 9 K. The most striking feature is the disappearance of the signals at $(320\,\mathrm{kHz}/f)^2 = 0.5, 2$ and 3, which supports the conclusion that hydrogen was indeed present at early stages of cooldown but was effectively pumped out by the end of the procedure.

Lastly, Fig. A.7a shows data taken at the start of cooldown. In this case, the most visible peak is the one at $(320\,\mathrm{kHz}/f)^2 = 12$, which suggests the presence of $N^+$, $O^+$, $N_2^+$ and/or $O_2^+$. Although not fully characterized, this is consistent with the observations made with higher accumulator pressures discussed above. There is also a small signal around $(320\,\mathrm{kHz}/f)^2 = 30$ that was not visible in any of the previous experimental traces. It agrees with the simulations of $N_2^+$ and/or $O_2^+$, and suggests the presence of a large number of heavy gas molecules when the temperature of the apparatus was close to 100 K.

The residual gas was also ionized through collisions with electrons instead of positrons. It was observed experimentally that, under stable (cold) conditions, the number of ions so produced correlated well with antiproton lifetime measurements and provided a way to estimate the density of the residual gas in the apparatus [7]. Nevertheless, since electrons and ions have opposite charge, they tend to cool into separate potential wells, whereupon they lose contact and no further sympathetic cooling can occur. The very large energy spread of the ions made the experimental data difficult to analyze. Ionization with positrons avoided such problems.

## A.4 Conclusions of the studies

The simulations and experimental traces suggest that He, $N_2$ and possibly $O_2$ were present when the ALPHA1 trap was at 9 K. Helium is not a common contaminant, so its presence might be an indication of small leaks from the surrounding liquid helium reservoir. As neither gaseous nitrogen nor oxygen can exist in thermodynamic equilibrium in a closed chamber at that temperature, their presence suggests that they originated from other parts of the apparatus. Nitrogen accompanying the transfer of positrons from the positron accumulator is the likely source of nitrogen. Other data taken when the trap was cooling down from 100 K, showed the gradual disappearance of other species, notably hydrogen.

The analysis is complicated by subharmonic resonances and the lack of precise knowledge of the initial energy distribution of the ions in the anharmonic well when the apparatus was not in stable (cold) conditions. Precise measurements of these energies would allow for more complete simulations of the traces during cooldown and with higher positron accumulator pressures. This is something that should be considered in future implementations, possibly in ALPHA2.

# Bibliography

[1] M. Amoretti et al. (ATHENA Collaboration). “Production and detection of cold antihydrogen atoms”. In: *Nature* 419 (2002), p. 456.

[2] G. Gabrielse et al. “Background-free observation of cold antihydrogen and a field-ionization analysis of its states”. In: *Phys. Rev. Lett.* 89.213401 (2002).

[3] Y. Enomoto et al. “Synthesis of cold antihydrogen in a cusp trap”. In: *Phys. Rev. Lett.* 105.243401 (2010).

[4] G.B. Andresen et al. (ALPHA Collaboration). “The ALPHA antihydrogen trapping apparatus”. In: *Nucl. Instrum. Methods Phys. Res.* In review (2013).

[5] G.B. Andresen et al. (ALPHA Collaboration). “Trapped antihydrogen”. In: *Nature* 468 (2010), pp. 673–676.

[6] G.B. Andresen et al. (ALPHA Collaboration). “Search for trapped antihydrogen”. In: *Phys. Lett. B* 695 (2011), pp. 95–104.

[7] G.B. Andresen et al. (ALPHA Collaboration). “Confinement of antihydrogen for 1000 seconds”. In: *Nature Phys.* 7 (2011), pp. 558–564.

[8] C. Amole et al. (ALPHA Collaboration). “Resonant quantum transitions in trapped antihydrogen atoms”. In: *Nature* 483 (2012), pp. 439–443.

[9] C. Amole et al. (ALPHA Collaboration) and A.E. Charman. “Description and first application of a new technique to measure the gravitational mass of antihydrogen”. In: *Nature Comms.* 4.1785 (2013).

[10] M. Hori et al. “Two-photon laser spectroscopy of antiprotonic helium and the antiproton-to-electron mass ratio”. In: *Nature* 475 (2011), pp. 484–488.

[11] M. Charlton et al. “Antihydrogen for precision tests in physics”. In: *Cont. Phys.* 49 (2008), pp. 29–41.

[12] C.G. Parthey et al. “Improved measurement of the hydrogen 1S-2S transition frequency”. In: *Phys. Rev. Lett.* 107.203001 (2011).

[13] G. Bressi et al. “Testing the neutrality of matter by acoustic means in a spherical resonator”. In: *Phys. Rev. A* 83.052101 (2011).

[14] G. Baur et al. “Production of antihydrogen”. In: *Phys. Lett. B* 368 (1996), pp. 251–258.

[15] J. Beringer et al. (Particle Data Group). “Review of particle physics”. In: *Phys. Rev. D* 86.010001 (2012).

[16] R.J. Hughes and B.I. Deutch. “Electric charges of positrons and antiprotons”. In: *Phys. Rev. Lett.* 105 (1992), pp. 578–581.

[17] Tim Friesen. Personal communication. Feb. 12, 2013.

[18] G.B. Andresen et al. (ALPHA Collaboration). “Autoresonant excitation of antiproton plasmas”. In: *Phys. Rev. Lett.* 106.025002 (2011).

[19] G.B. Andresen et al. (ALPHA Collaboration). “Evaporative cooling of antiprotons to cryogenic temperatures”. In: *Phys. Rev. Lett.* 105.013003 (2010).

[20] G.B. Andresen et al. (ALPHA Collaboration). “Centrifugal separation and equilibration dynamics in an electron-antiproton plasma”. In: *Phys. Rev. Lett.* 106.145001 (2011).

[21] E. Butler. “Antihydrogen formation, dynamics and trapping”. PhD thesis. Swansea University, 2011.

[22] R.A. Hydomako. “Detection of trapped antihydrogen”. PhD thesis. University of Calgary, 2011.

[23] C.F. Driscoll and J.H.Malmberg. “Length-dependent containment of a pure electron-plasma column”. In: *Phys. Rev. Lett.* 50 (1983), pp. 167–170.

[24] S.F. Chapman. “The effect of multipole-enhanced diffusion on the joule heating of a cold non-neutral plasma”. PhD thesis. University of California, Berkeley, 2011.

[25] T.J. Murphy and C.M. Surko. “Positron trapping in an electrostatic well by inelastic collisions with nitrogen molecules”. In: *Phys. Rev. A* 46.5696 (1992).

[26] G.B. Andresen et al. (ALPHA Collaboration). “Antiproton, positron, and electron imaging with a microchannel plate/phosphor detector”. In: *Rev. Sci. Instrum.* 80.123701 (2008).

[27] C. Cohen-Tannoudji, B. Diu, and F. Laloe. *Quantum Mechanics, Vol. 2.* Paris, France: Hermann and John Wiley, 1977.

[28] L. Essen et al. “Frequency of the hydrogen maser”. In: *Nature* 229 (1971), pp. 110–111.

[29] J. DiSciacca et al. (ATRAP collaboration). “One-particle measurement of the antiproton magnetic moment”. In: *Phys. Rev. Lett.* 110.130801 (2013).

[30] W. Bertsche et al. “A magnetic trap for antihydrogen confinement”. In: *Nucl. Instrum. Methods Phys. Res. A* 566 (2006), pp. 746–756.

[31] G.B. Andresen et al. (ALPHA Collaboration). “Antihydrogen annihilation reconstruction with the ALPHA silicon detector”. In: *Nucl. Instrum. Methods Phys. Res. A* 684 (2012), pp. 73–81.

[32] C. Amole et al. (ALPHA Collaboration). “Discriminating between antihydrogen and mirror-trapped antiprotons in a minimum B-trap”. In: *New J. Phys.* 14.015010 (2012).

[33] Prof. Scott Menary and Andrea Capra. Personal communication. July 17, 2013.

[34] C. Amole et al. (ALPHA Collaboration) and L. Friedland. "Experimental and computational study of the injection of antiprotons into a positron plasma for antihydrogen production". In: *Phys. Plasmas* 20.043510 (2013).

[35] D.J. Griffiths. *Introduction to electrodynamics, 3rd ed.* Upper Saddle River, New Jersey: Prentice Hall, 1999.

[36] Prof. Francis Robicheaux. Personal communication. Sept. 27, 2012.

[37] Chukman So. Personal communication. June 13, 2013.

[38] U. Schwickerath and V. Lefebure. "Usage of LSF for batch farms at CERN". In: *J. Phys.: Conf. Ser.* 119.042025 (2008).

[39] J.R. Klein and A. Roodman. "Blind analysis in nuclear and particle physics". In: *Annu. Rev. Nucl. Part. Sci.* 55 (2005), pp. 141–163.

[40] C. Amole et al. (ALPHA Collaboration). *Experimental limit on the charge of antihydrogen.* In preparation. 2013.

[41] Prof. Svante Jonsell. Personal communication. July 8, 2013.

[42] Dr. Tim Tharp. Personal communication. July 30, 2013.

[43] C. Amole et al. (ALPHA Collaboration). "In situ electromagnetic field diagnostics with an electron plasma in a Penning-Malmberg trap". In: *New J. Phys.* In review (2013).

[44] Prof. Scott Menary, Prof. Art Olin, and Andrea Capra. *Silicon vertex detector stability 2010-2011.* ALPHA internal communication. Aug. 7, 2013.

[45] *Empirical cumulative distribution function in MATLAB.* 2013. URL: `http://www.mathworks.com/help/stats/ecdf.html`.

[46] J.F. Lawless. *Statistical Models and Methods for Lifetime Data, 2nd ed.* Hoboken, New Jersey: John Wiley and Sons Inc., 2003.

[47] P.H. Donnan, M.C. Fujiwara, and F. Robicheaux. "A proposal for laser cooling antihydrogen atoms". In: *J. Phys. B* 46.025302 (2013).

[48] W.M. Haynes ed. *CRC Handbook of Chemistry and Physics, 94th Edition (Internet Version 2014).* Boca Raton, Florida: CRC Press/Taylor and Francis.

[49] C. Amole et al. (ALPHA Collaboration). "Autoresonant-spectrometric determination of the residual gas composition in the ALPHA experiment apparatus". In: *Rev. Sci. Instrum.* 84.065110 (2013).

[50] J.S. de Grassie and J.H. Malmberg. "Waves and transport in the pure electron plasma". In: *Phys. Fluids* 23.63 (1980).

[51] F. Anderegg et al. "A new pure ion plasma device with laser induced fluorescence diagnostic". In: *Rev. Sci. Instrum.* 68.2367 (1997).

[52] G. Gabrielse et al. “Thousand-fold improvement in the measured antiproton mass”. In: *Phys. Rev. Lett.* 65 (1990), pp. 1317–1320.

[53] G. Lewin. *Fundamentals of vacuum science and technology.* McGraw-Hill, 1965, pp. 51–55.

[54] A.V. Ermakov and B.J. Hinch. “An electrostatic autoresonant ion trap mass spectrometer”. In: *Rev. Sci. Instrum.* 81.013107 (2010).

[55] G. Brucker and J. Rathbone. “Autoresonant trap mass spectrometry (ART-MS) for remote sensing applications”. In: *Int. Jour. Mass Spec.* 295 (2010), pp. 133–137.

[56] J. Fajans and L. Friedland. “Autoresonant (non stationary) excitation of a pendulum, Plutinos, plasmas and other nonlinear oscillators”. In: *Am. J. Phys.* 69.1096 (2001).

[57] K. W. Murch et al. “Quantum fluctuations in the chirped pendulum”. In: *Nature Physics* 7 (2011), pp. 105–108.

[58] J. Fajans, E. Gilson, and L. Friedland. “Autoresonant (nonstationary) excitation of the diocotron mode in non-neutral plasmas”. In: *Phys. Rev. Lett.* 82 (1999), pp. 4444 –4447.

[59] J. Fajans, E. Gilson, and L. Friedland. “Second harmonic autoresonant control of the l=1 diocotron mode in pure electon plasmas”. In: *Phys. Rev. E* 62.4131 (2000).

[60] L.V. Jørgensen et al. (ATHENA Collaboration). “New source of dense, cryogenic positron plasmas”. In: *Phys. Rev. Lett.* 95.025002 (2005).

[61] H. Knudsen et al. “Single ionization of $H_2$, He, Ne and Ar by positron impact”. In: *J. Phys. B: At. Mol. Opt. Phys.* 23.3955 (1990).

[62] H. Bluhme. “Ionisation by Positron Impact”. PhD thesis. University of Aarhus, Denmark, 2000.

[63] J.P. Marler and C.M. Surko. “Positron-impact ionization, positronium formation, and electronic excitation cross sections for diatomic molecules”. In: *Phys. Rev. A* 72.062713 (2005).

[64] W.H. Press et al. *Numerical Recipes in C, 2nd edition.* Cambridge: Cambridge University Press, 1992, pp. 710–722.

[65] U. Bischler and E. Bertel. “Simple source of atomic hydrogen for ultrahigh vacuum applications”. In: *J. Vac. Sci. Technol. A* 11.458 (1993).

[66] A.V. Phelps. “Cross sections and Swarm coefficients for $H^+$, $H_2^+$, $H_3^+$, H, $H_2$ and $H^-$ in $H_2$ for energies from 0.1 eV to 10 keV”. In: *J. Phys. Chem. Ref. Data* 19.653 (1990).